

TRANS NOW

TRANSPORTATION NORTHWEST

**Final Report
TNW2011-17**

Research Project Agreement No. 64-8532

SEISMIC BEHAVIOR AND DESIGN OF SEGMENTAL PRECAST POST-TENSIONED CONCRETE PIERS

Haitham Dawood
Research Assistant
Civil and Environmental Engineering
Washington State University

Mohamed ElGawady
Assistant Professor
Civil and Environmental Engineering
Washington State University

William Cofer
Professor
Civil and Environmental Engineering
Washington State University

A report prepared for

Transportation Northwest (TransNow)
University of Washington
112 More Hall, Box 352700
Seattle, Washington 98195-2700

and

Washington State Department of Transportation

June 2011

TECHNICAL REPORT STANDARD TITLE PAGE

1. REPORT NO. TNW2011-17	2. GOVERNMENT ACCESSION NO.	3. RECIPIENT'S CATALOG NO.	
4. TITLE AND SUBTITLE SEISMIC BEHAVIOR AND DESIGN OF SEGMENTAL PRECAST POST-TENSIONED CONCRETE PIERS		5. REPORT DATE 6/11	
		6. PERFORMING ORGANIZATION CODE 64-8532	
7. AUTHOR(S) Haitham Dawood, Mohamed ElGawady, William Cofer		8. PERFORMING ORGANIZATION REPORT NO. TNW2011-17	
9. PERFORMING ORGANIZATION NAME AND ADDRESS Transportation Northwest Regional Center X (TransNow) Box 352700, 112 More Hall University of Washington Seattle, WA 98195-2700		10. WORK UNIT NO.	
		11. CONTRACT OR GRANT NO. DTRT07-G-0010	
12. SPONSORING AGENCY NAME AND ADDRESS United States Department of Transportation Office of the Secretary of Transportation 1200 New Jersey Ave, SE Washington, D.C. 20590		13. TYPE OF REPORT AND PERIOD COVERED Final Technical Report	
		14. SPONSORING AGENCY CODE	
15. SUPPLEMENTARY NOTES			
<p>ABSTRACT</p> <p>Segmental precast column construction is an economic environmental friendly solution to accelerate bridge construction in the United States. Also, concrete-filled fiber reinforced polymer tubes (CFFT) represents a potential economic solution for durability issues in bridge industry. Combining the segmental precast and CFFT will result in rapid durable construction system. The proposed research will build on recent work by the PI where he experimentally investigated the seismic behavior of tens single-column and two-column bents constructed using precast post-tensioned CFFT. The columns were constructed by stacking precast CFFT segments one on top of the other and then post-tensioned using unbonded tendons. Two specimens had external energy dissipation devices and another two specimens had neoprene in the joints between the CFFT segments. The neoprene significantly reduced the seismic displacement demand. The columns re-centered upon the conclusion of the test resulting in minimal residual displacement which represents, in the case of a real strong earthquake, a huge advantage since the post-earthquake repair measures will be minimal. A 3-D finite element models were developed by the PI to predict the performance of the single-column under monotonic lateral loads. The main objective of this proposal is to improve and expand the capabilities of these finite element models to produce design recommendations. In particular, the models will be expanded to include dynamic loading, two-column bents, and the neoprene in the joints. Including dynamic loading in the model is essential to quantify the energy dissipation due to rocking of the columns segments. The output of this research will be recommendations on the optimum construction characteristics of the system including the segment height/column diameter ratio, neoprene thickness and hardness, external energy dissipater requirements, and post-tensioning force level. The proposed research will develop a durable environmental friendly rapid construction bridge system, which has low life-cycle costs, construction waste, noise, traffic disruption, and initial construction cost. In addition, the developed system will has high work zone safety, efficient use of construction material, a short construction time, and improved constructability. The proposed construction system will not have a leakage of wet concrete into waterways leading to pollution of water and harm migrating fish. Finally, when the proposed construction system fully developed and implemented in construction, it will reduce the expense of bridge replacement, repair, and continuous operation interruption after earthquakes.</p>			
17. KEY WORDS Key words: concrete, CFFT, seismic, smart infrastructure		18. DISTRIBUTION STATEMENT No restrictions.	
19. SECURITY CLASSIF. (of this report) None	20. SECURITY CLASSIF. (of this page) None	21. NO. OF PAGES 131	22. PRICE

DISCLAIMER

The contents of this report reflect the views of the authors, who are responsible for the facts and the accuracy of the information presented herein. This document is disseminated under the sponsorship of the Department of Transportation University Transportation Centers Program, in the interest of information exchange. The U.S. Government assumes no liability for the contents or use thereof.

SEISMIC BEHAVIOR AND DESIGN OF SEGMENTAL PRECAST POST-TENSIONED
CONCRETE PIERS

by

Haitham Dawood

Research Assistant, Civil and Environmental Engineering

Washington State University

Mohamed ElGawady

Assistant Professor, Civil and Environmental Engineering

Washington State University

And

William Cofer

Professor, Civil and Environmental Engineering

Washington State University

October 2010

TABLE OF CONTENTS

	Page
ACKNOWLEDGEMENTS.....	iii
ABSTRACT.....	iv
LIST OF TABLES.....	ix
LIST OF FIGURES.....	x
CHAPTER ONE.....	1
1. INTRODUCTION.....	1
1.1 Innovative Precast Post-tensioned Bridge Bents Developed at Washington State University.....	1
1.1.1 Structural Advantages.....	1
1.1.2 Construction advantages.....	3
1.1.3 Environmental Advantages.....	3
1.2 Research objectives.....	4
CHAPTER TWO.....	5
2. LITERATURE REVIEW.....	5
2.1 Seismic Behavior of Precast Post-tensioned Segmental Columns	5
2.1.1 Experimental Studies.....	7
2.1.1.1 Experimental Studies Done At WSU.....	7
2.1.2 Simple Models.....	9
2.1.3 Finite Element Models.....	10
2.1.4 Lumped-mass Models.....	11
2.1.5 Energy Dissipation Systems.....	12
2.2 Concrete Confinement	13
2.3 Conclusions.....	14
2.4 References.....	14
CHAPTER THREE.....	16
3. BEHAVIOR OF SEGMENTAL PRECAST POST-TENSIONED BRIDGE PIERS UNDER LATERAL LOADS: EXPERIMENTAL AND MODELING	16
3.3 Introduction.....	17
3.4 Finite Element Modeling of Self-Centering Piers.....	19
3.5 Experimental work.....	23
3.5.1 Test pier design details.....	23
3.5.2 Test setup, instrumentation, and loading protocol.....	26
3.5.3 Description of test results.....	27
3.6 Model Validation.....	30
3.7 Analyses results.....	32
3.8 Sensitivity Analyses.....	38
3.9 Findings and conclusions.....	42
3.11 References.....	43
CHAPTER FOUR.....	45
4. BEHAVIOR OF SEGMENTAL PRECAST POST-TENSIONED BRIDGE PIERS	45

UNDER LATERAL LOADS: PARAMETRIC STUDY	
4.2 Keywords.....	46
4.3 Introduction.....	46
4.4 Results and Discussions.....	49
4.4.1 Effects of initial post-tensioning level in the tendon	49
4.4.2 Effects of initial stresses on the concrete	53
4.4.3 Effects of pier aspect ratio	56
4.4.4 Effects of construction details	58
4.4.5 Effects of confinement thickness	61
4.4.6 Effects of adding internal energy dissipaters.....	62
4.5 Findings and Conclusions.....	64
4.7 References.....	66
CHAPTER FIVE.....	
5. FINITE ELEMENT MODEL CALIBRATION AGAINST SPPT SYSTEM DEVELOPED IN WASHINGTON STATE UNIVERSITY AND PARAMETRIC STUDY.....	
5.1 Introduction	
5.2 Piers Tested by Booker A. (2008)	
5.3 Bents Tested by Sha'lan (2009)	
5.4 Finite Element Model Implementation	
5.5 Results and Discussions	
5.5.1 Piers	
5.5.2 Bents	
5.6 Parametric Study	
5.6.1 Effects of applied post-tensioning force	
5.6.2 Load combination effects	
5.6.3 Effects of pier aspect ratio	
5.6.4 Pier size effects	
5.6.5 Diameter size effects	
5.6.6 Confinement effects	
5.7 Conclusions	
5.8 References	
CHAPTER SIX.....	68
6. PERFORMANCE-BASES SEISMIC DESIGN OF UNBONDED SEGMENTAL PRECAST POST-TENSIONED CONCRETE PIERS.....	68
6.2 Keywords.....	68
6.3 Segmental Precast Post-tensioned (SPPT) Piers.....	69
6.4 Summary of the Finite Element Model.....	69
6.5 Study Description.....	72
6.6 Performance levels.....	74
6.6.1 Performance objectives for the serviceability level.....	77
6.6.2 Performance objectives for the collapse-prevention level.....	78
6.7 Bilinear approximation.....	78
6.8 Residual Drift Angles.....	79
6.9 Equivalent viscous damping.....	80
6.10 Study Procedure.....	80
6.11 Collapse-prevention Limit State.....	81

6.11.1 Effective stiffness (K_{CP-e})	81
6.11.2 Yield load (F_{CP-y})	82
6.11.3 Yield displacement (Δ_{CP-y})	84
6.11.4 Performance displacement (Δ_{CP-p})	84
6.11.5 Performance load (F_{CP-p})	84
6.11.6 Error in predicting the lateral strength (collapse-prevention)	85
6.12 Serviceability Limit State.....	86
6.12.1 Effective stiffness (K_{Ser-e}).....	87
6.12.2 Yield load (F_{Ser-y}).....	87
6.12.3 Yield displacement (Δ_{Ser-y}).....	88
6.12.4 Performance displacement (Δ_{Ser-p}).....	88
6.12.5 Performance load (F_{Ser-p}).....	88
6.12.6 Error in predicting the lateral strength (serviceability).....	89
6.13 Increase of Post-tensioning with lateral drift angle.....	90
6.14 Design Procedure	96
6.15 Findings and Conclusions.....	101
6.17 References.....	103
APPENDIX.....	106
A. APPENDIX A (MATERIALS TESTING).....	107
A.1 Concrete.....	107
A.2 Post-tensioning bars.....	109
A.3 Glass Fiber Reinforced Polymer (GFRP).....	111
A.4 Fiber Sheets Used To Retrofit JH12 & JH22 (CHAPTER 3).....	116
A.5 References.....	116

LIST OF TABLES

	Page
Table 2.1: Examples of bridges constructed using segmental columns.....	5
Table 3.1: The matrix of the experimental work.....	24
Table 3.2: Summary of steel coupons tension tests.....	25
Table 3.3: Concrete compressive strength for test units (f_c' , MPa).....	25
Table 3.4: Properties of the FRP.....	30
Table 4.1: Different values assigned for each parameter in the parametric study.....	49
Table 5.1: Description of the columns used in the laboratory testing.....	
Table 5.2: Description of the bents used in the laboratory testing.....	
Table 6.1: Different studied parameters for the SPPT piers.....	73
Table 6.2: Material Properties of GFRP tubes.....	73
Table 6.3: Annual probability of exceedance of the design earthquake for each seismic performance level in California.....	75
Table A.1: Summary of compression test results.....	108
Table A.2: Summary of tension tests of GFRP specimens.....	112
Table A.3: Typical dry fiber properties used in chapter (3).....	116

LIST OF FIGURES

	Page
Figure 1.1: Schematic drawing of the PPT-CFFT System.....	3
Figure 2.1: Examples of segmental columns	6
Figure 2.2: Columns tested (From ElGawady et al. 2010).....	8
Figure 2.3: Tested frames (From ElGawady and Sha'lan 2010).....	9
Figure 2.4: Backbone curve of the test specimens, (From ElGawady et al. 2009).....	10
Figure 3.1: A typical mesh and applied loads and displacements for the SPPT pier.....	20
Figure 3.2: Test setup for specimens.....	26
Figure 3.3: Experimental hysteretic response plots	28
Figure 3.4: Experimental hysteretic response plots	28
Figure 3.5: Stress strain curves for unconfined and confined concrete.....	31
Figure 3.6: Specimen JH12 (a) during testing, and (b) FE model results.....	33
Figure 3.7: A schematic of a rocking pier indicating stresses and strains at different heights of the pier.....	33
Figure 3.8: Specimen JH11 at failure.....	35
Figure 3.9: Experimental versus predicted backbone curves for slender virgin piers.....	36
Figure 3.10: Experimental versus predicted backbone curves for squat virgin piers.....	37
Figure 3.11: Errors in predicting the strengths.....	37
Figure 3.12: Error in post tensioning stress versus drift angle.....	39
Figure 3.13: Different softening behavior of concrete.....	40
Figure 3.14: The effects of concrete material softening behavior on the response of piers.	41
Figure 3.15: Effects of coefficients of friction on the backbone curves of pier JH11.....	41
Figure 4.1: Detailed dimensions for piers.....	47
Figure 4.2: A typical mesh and applied loads and displacements for the SPPT pier.....	48
Figure 4.3: The effects of changing the initial post-tensioning stress in the tendons while keeping the same stress on concrete.....	50
Figure 4.4: Piers' drifts Vs. the stresses in the post-tensioning tendons normalized by its yield stress.....	51
Figure 4.5: The effects of changing the initial post-tensioning stress in the tendons for squat piers.....	51
Figure 4.6: Squat piers' drifts Vs. the stresses in the post-tensioning tendons normalized by its yield stress.....	52
Figure 4.7: The effects of increasing the axial stresses due to post-tensioning forces on concrete segments.....	54
Figure 4.8: The increase in the post-tensioning stresses vs. the standard piers lateral drifts.....	55
Figure 4.9: The effects of increasing the axial stresses on concrete segments for Pier B..	56
Figure 4.10: The increase in the post-tensioning stresses vs. piers type B lateral drifts.....	56

Figure 4.11:	Layout of the piers having different aspect ratios.....	57
Figure 4.12:	The effect of changing the piers' aspect ratio on the backbone curves.....	57
Figure 4.13:	The mechanism of deformation for slender and squat piers.....	58
Figure 4.14:	Configuration of each pier of CON series.....	59
Figure 4.15:	The effects of the different configurations on the backbone curves.....	60
Figure 4.16:	The effects on the backbone curves of the different confinement thicknesses	62
Figure 4.17:	The effects of the IED on the backbone curves.....	63
Figure 4.18:	High stress concentrations in the segments due to the insufficient development length of the IED bar.....	64
Figure 4.19:	The effects of different IED rebar diameters on normalized stresses on the rebar.....	64
Figure 5.1:	Schematic drawing showing the setup for the cyclic loading test for the piers	
Figure 5.2:	Schematic drawing for the two piers used for the calibration of the FE model	
Figure 5.3:	Schematic drawing showing the setup for the cyclic loading test for the bents	
Figure 5.4:	Schematic drawing for the tested frames.....	
Figure 5.5:	Stress strain curves for the concrete of segments.....	
Figure 5.6:	Stress strain curves for the concrete of the beam.....	
Figure 5.7:	Experimental versus predicted backbone curves for the singly segmented pier	
Figure 5.8:	Experimental versus predicted backbone curves for the multi segmented pier.	
Figure 5.9:	Experimental versus predicted backbone curves for the singly segmented bents.....	
Figure 5.10:	Experimental versus predicted backbone curves for the multi segmented bents.....	
Figure 5.11:	Effects of changing the applied post-tensioning forces on the backbone curves of piers having different aspect ratios.....	
Figure 5.12:	Effects of different combinations of axial stresses for piers with different aspect ratios.....	
Figure 5.13:	Effects of piers aspect ratios on the backbone curves.....	
Figure 5.14:	Backbone curves for two piers having different aspect ratios.....	
Figure 5.15:	Backbone curves for piers from the S series (dashed line) and L series (solid line) with different heights.....	
Figure 5.16:	An approximate mechanism for rocking of two piers having the same height but with different cross sectional diameter.....	
Figure 5.17:	Backbone curves for piers of the L series constructed using different FRP materials.....	
Figure 5.18:	Backbone curves for piers of the S series constructed using different FRP materials.....	
Figure 5.19:	The stress-strain relationships for piers from the S and L series confined using different FRP materials.....	
Figure 6.1:	Schematic drawing of the SPPT pier showing the used mesh in the FE model	70

	and the system's different components.....	
Figure 6.2:	Opening of the interface between the foundation and the pier during lateral loading.....	71
Figure 6.3:	Stress concentration at the pier's toe.....	72
Figure 6.4:	Stress strain obtained from Samaan et al. (1998) to model the GFRP confined concrete of the piers.....	74
Figure 6.5:	Backbone curve along with its bilineaized form.....	79
Figure 6.6:	The collapse-prevention yield load associated with each specific pier.....	83
Figure 6.7:	The collapse-prevention performance load associated with each specific pier	85
Figure 6.8:	The lateral drift angle vs. the error in predicting the pier's strength (collapse-prevention limit state).....	86
Figure 6.9:	The serviceability yield load associated with each specific pier.....	88
Figure 6.10:	The serviceability performance load associated with each specific pier.....	89
Figure 6.11:	The lateral drift angle vs. the error in predicting the pier's strength (serviceability limit state).....	90
Figure 6.12:	The relationship between the lateral drift angle (%) vs. the stress in the post-tensioning tendon's normalized by its initial stress for piers.....	92
Figure 6.13:	The relationship between the lateral drift angle (%) vs. the stress in the post-tensioning tendon's normalized by its initial stress for piers.....	93
Figure 6.14:	Error in predicting the change of post-tensioning stress with lateral drift angle.....	93
Figure 6.15:	Flow chart diagram of the proposed design procedure for SPPT piers.....	95
Figure 6.16:	A diagram showing how to obtain the periods of the pier from the uniform hazard displacement spectra of the Seattle, WA area.....	97
Figure 6.17:	A diagram showing how to obtain the periods of the pier from the uniform hazard displacement spectra of the Seattle, WA area.....	99
Figure A.1:	Test setup for computing concrete characteristic strength f'_c	107
Figure A.2:	Test setup for computing static modulus of elasticity of the concrete cylinders.....	108
Figure A.3:	Stress strain curves from the cylinders tests along with the equations of the trend lines.....	109
Figure A.4:	Copy of the report supplied by the DYWIYDAG company.....	111
Figure A.5:	Copy of the compression testing report of the FRP.....	115

CHAPTER ONE

INTRODUCTION

The use of precast segmental construction for concrete bridges in the United States has increased in recent years due to the demand for shortened construction periods, low environmental impacts and the desire for innovative designs that result in safe, economical and efficient structures. However, the behavior and performance of precast segmental bridges during earthquakes is of concern, and consequently their widespread use in moderate to high seismic regions such as the West Coast of the United States is limited.

1.1 Innovative Precast Post-tensioned Bridge Bents Developed at Washington State University

During the last few years, an innovative segmental precast post-tensioned bridge construction system was developed at Washington State University. The columns of the developed system consists of segmental concrete filled fiber reinforced polymer tubes (CFFT) and the precast segments are superimposed one on top of the other and then connected structurally with vertical post-tensioned tendons passing through ducts located in the precast segments. The tendons are anchored in the foundation of the column and in the bent cap at the column top (Figure 1.1). Constructing bridge columns in this manner offers several structural, construction and environmental advantages over conventional reinforced concrete (R.C.) designs.

1.1.1 Structural Advantages

A schematic of deformed shape of the CFFT segmental column under transverse loading is shown in Figure 1.1. The post-tensioning load keeps the whole system as one unit. Under lateral loads the stresses under the precast segments start to be a combination of the normal force induced by prestressing and moment induced by the lateral load. Once the stress reach a zero value at a point under a segment, any increase in the lateral load leads to an opening between that segment and the one beneath it. This opening continues to propagate with the load increase until it reached the prestressing bar at the C.G. of the cross section. This is when the post-tensioning steel bar is stretched and the stress in the tendons increase. The fact that the opening between the components propagates means that the stiffness of the system decreases and as a result the energy absorbed from the event decreases.

The tendon is unbonded over the height of the column so incremental stresses and strains are not concentrated at the crack, this is the reason why unbonded tendons are chosen for this system, and if the initial prestress level is well chosen, the prestressing steel will not yield. This is essential for this system for several reasons. First, the ability to transfer shear forces across the segments' interface joints by shear friction is dependent on the clamping force provided by the prestressing tendon. The column stiffness depends on the prestressing force and hence is not reduced drastically if the prestress is maintained. Finally, the restoring force (self-centering ability) is provided to the column if the prestress is maintained during and after the earthquake ensuring that the column returns to the undeformed position.

CFFT bents have an encouraging behavior under seismic loads, as the residual column drift will be negligible, and damage in the form of concrete spalling minimal and limited to the region near the compression toe of the column. Yielding of longitudinal bars, which is typical of R.C. columns, will not occur for the precast post-tensioned concrete filled fiber reinforced

polymer tubes (PPT-CFFT). Which means that a precast concrete segmental bridge column will remain functional immediately after a moderate to strong seismic event and will require minimal repair. Due to their exceptional seismic performance, this system would be particularly attractive in bridges considered as lifeline structures.

1.1.2 Construction Advantages

Construction schedules can be shortened significantly since bridge components can be rapidly produced at the precasting facility, where assembly lines and steam curing increase the efficiency of concrete construction. Additionally, the erection of a segmental bridge in the field can proceed rapidly, thus reducing the disruption to existing traffic infrastructure.

1.1.3 Environmental Advantages

This system reduces noise and leakage of wet concrete into waterways and fuel consumption due to congestion and rerouting of cars during construction. So it reduces sound, water and air pollution when compared to the conventional R.C. systems.

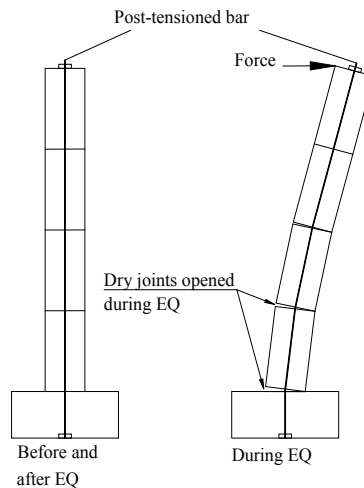


Figure 1.1 Schematic drawing of the PPT-CFFT System

1.2 Research Methodology

This study started with the development of a FE model capable of capturing the behavior of the SPPT pier system. The model was calibrated against three different experimental studies with two different configurations of the SPPT system. The model was then used to conduct a parametric study to have a better understanding of the effect of different parameters and configurations on the seismic behavior of the SPPT piers. The data collected from a large number of analyzed piers was then used to develop a design procedure for the system using empirical equations.

CHAPTER TWO

LITERATURE REVIEW

2.1 Seismic Behavior of Precast Post-tensioned Segmental Columns

Segmental precast post-tensioned (SPPT) systems in low to medium seismic zones have proven to be an economical and advantageous construction system. Table 2.1 and Figure 2.1 show examples of bridges constructed in this way. However, little is known about the seismic behavior of SPPT system. Recently, several research projects have investigated the seismic behavior of unbonded and bonded post-tensioned segmental columns.

Bridge	Location	Description
Louetta Road Overpass	Houston, Texas	precast post-tensioned piers
Sunshine Skyway Bridge	Florida	precast PT hollow elliptical column segments
U.S. 183 Elevated	Austin, TX	Hollow Precast Piers
Varina-Enon Bridge	Virginia	Precast concrete elements for the piers
South Rangitikei Rail Bridge	New Zealand	Rocking bridge pier
Lions Gate Bridge (north approach)	Vancouver	Rocking bridge pier



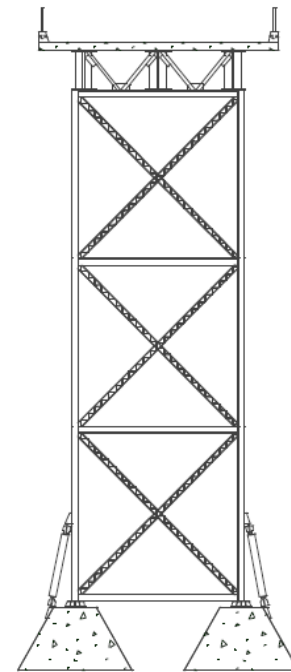
(a)



(b)



(c)



(d)

Figure 2.1 Examples of segmental columns
(a) Louetta Road Overpass,
(b) U.S. 183 Elevated columns during construction,
(c) South Rangitikei Rail Bridge, and
(d) Schematic diagram of the controlled rocking pier used in lions gate bridge

2.1.1 Experimental Studies

Hewes and Priestley (2002) conducted cyclic loading on four, 40% scaled, unbonded segmental post-tensioned columns with different aspect ratios. Each column was tested twice under low and high initial prestressing. Two different thicknesses of steel confinement were used for the lower segments only, while the upper segments were reinforced concrete.

Chang et al. (2002) conducted a study on four large-scale hollow precast unbonded post-tensioned reinforced concrete segmented columns. Each specimen consisted of nine or ten 1m tall, precast column segments.

Chou and Chen (2006) tested two one-sixth scale (16.67%) precast unbonded post-tensioned concrete filled steel tubes, segmental columns through cyclic loading tests.

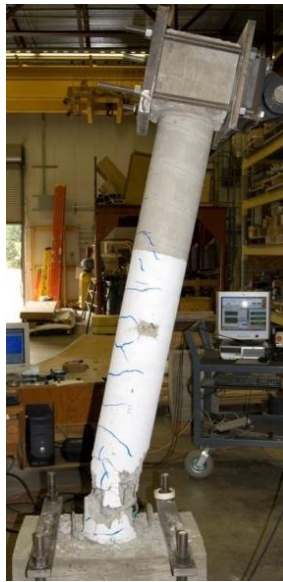
Marriott et al. (2009) tested three, one-third scale (33%) columns. Two were segmental columns while the third was monolithic reinforced concrete (RC).

The previously mentioned efforts highlighted the ability of the system to undergo large lateral displacements with no sudden strength reduction (failure). The reported residual displacements were much lower compared to the monolithic RC system. The low hysteretic energy dissipation capacity, due to the minimal concrete damage, was of concern.

2.1.1.1 Experimental Studies Done At WSU

ElGawady et al. (2009) and ElGawady and Sha'lan (2010) studied the performance of precast post-tensioned segmented columns and frames under cyclic loads. The test matrices of the two studies consisted of four precast post-tensioned concrete fiber tubes (PPT-CFFT), columns, and frames along with two cast-in-place RC specimens (Fig 2.2 and 2.3) as control

specimens. The segments consisted of plain concrete cylinders confined by glass fiber reinforced polymer (GFRP) tubes. For each study, one single segment specimen was tested and three multi-segmented specimens (consisted of 4 segments for the columns study and 3 segments for the frames study stacked over each other). Steel angles were used as external fuses for one multi-segmented specimen in each study. Also, rubber pads were used as base isolators for a column and a frame.



RC column

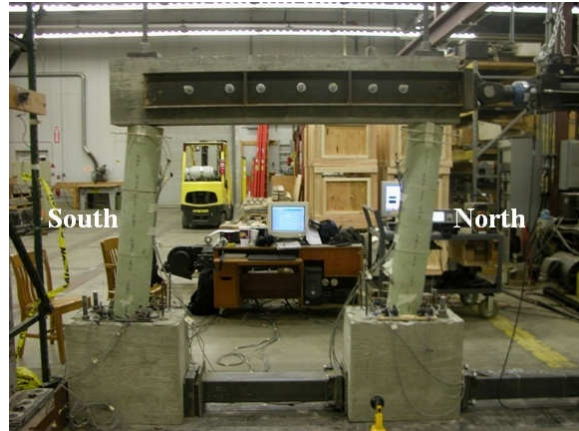


Multi-segmented

Figure 2.2 Columns tested (From ElGawady et al. 2010)



RC



Multi-segmented

Figure 2.3 Tested frames (From ElGawady and Sha'lan 2010)

2.1.2 Simple Models

A simplified analytical three-stage model was developed by Hewes and Priestley (2002); their results showed that the model was able to predict the backbone curves of the tested columns quite well.

Ou et al. (2007) used the experimental data obtained by Chang et al. (2002) to develop a simplified analytical model for static pushover analysis as well, but also taking into consideration the presence of longitudinal mild steel reinforcement across the column segment joints.

ElGawady et al. (2009) and ElGawady and Sha'lan (2010) attempted to verify the simplified analytical model originally developed by Hewes and Priestley (2002) against their test results. The model overestimated the yield point of the system (Fig. 2.4). To capture the experimental backbone curve, the plastic hinge length definition was changed according to Hines et al. (2001). This proved that the model isn't yet accurate enough to capture the behavior of different systems.

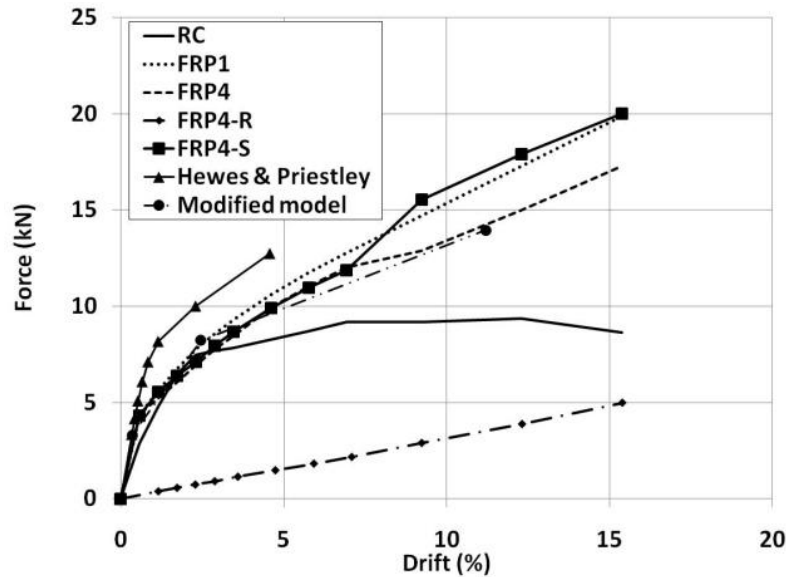


Figure 2.4: Backbone curve of the test specimens, (From ElGawady et al. 2009)

2.1.3 Finite Element Models

A wide range of numerical modeling techniques were used to model the response of segmental columns including 2-dimensional (2D-FEM), 3-dimensional, finite element (3D-FEM), and macro-models (multi-spring models). No 3D-FEM has been developed to model fiber and steel confined segments.

Kwan and Billington (2003 a,b) developed a 2D finite element model to simulate the behavior of partially post-tensioned reinforced concrete bridge piers. They developed models for single column piers as well as two-column bents and studied the behavior under monotonic, cyclic, and seismic loads. The material models were verified in the study. However, the overall response of the system wasn't calibrated.

Ou et al. (2007) also developed a 3D finite element model using the test results of Chang et al. (2002). A cyclic loading pattern was applied to the model to validate the simplified analytical model.

The 2D-FEM and 3D-FEM, at present, are only capable of capturing the general behavior of the segmental columns. Each of the FE models was calibrated against one set of data. Hence, the literature didn't include a standard approach to develop a FE model capable of capturing the behavior of different systems layouts, particularly fiber and steel confined. This is the preliminary target of this study.

Marriott et al. (2009) developed and tested the efficiency of two macro-models (multi-spring model). ElGawady et al. (2010) developed a pushover analysis of a segmental frame system using SAP2000. To be able to correctly implement this type of approach, a good physical understanding of the system and its behavior is required in order to implement the correct assumptions and parameters to the model and to be confident in the output.

2.1.4 Lumped-mass Models

In this approach, the columns are assumed to be a single degree of freedom system (SDOF) with a lumped mass at the top. The hysteretic diagrams developed by experimental tests and/or FE models are then modified to an idealized flag-shape hysteretic for the SDOF.

Ou et al. (2007) used the 3D FE analyses and the cyclic test data from Chang et. al (2002) to develop a flag-shaped (FS) model. By assuming that the columns are a lumped-mass SDOF, the response-history of the columns under 25 near-fault ground motions was easily computed in order to study the behavior of the system under seismic loading.

Chou and Hsu (2008) developed a FS and a stiffness-degrading flag-shaped (SDFS) models according to the hysteretic curves obtained from the cyclic loading of precast post-tensioned segmented columns. Both the FS and SDFS models considered hysteretic energy dissipation. However, only SDFS took the stiffness degradation into consideration. The discrepancy between the results of both assumptions showed the importance of considering stiffness degradation in predicting the dynamic response of the system.

The importance of this approach is that it makes possible a simplified dynamic analysis of the system under seismic excitations. The importance of this method is that it allows the development of the seismic analysis in a fast and economic way if compared with the FE analysis.

2.1.5 Energy Dissipation Systems

To overcome the drawback of low hysteretic energy dissipation capacity, additional energy dissipaters were used to increase the hysteretic damping of the system. In most cases hysteretic damping comes from the yielding of the steel element. Energy dissipaters can be divided into two main categories, namely, internal and external (fuses) energy dissipation systems.

Chang et al. (2002) and Ou et al. (2007) used mild steel bars between column segments as internal energy dissipaters. The bars proved their efficiency by significantly increasing the hysteretic energy dissipation. The major problem with this type of dissipater is that, after yielding, the bars are permanently deformed and the whole system suffers from residual displacement after loading.

External energy dissipaters (fuses) have been used by Chou and Chen (2006), Marriott et al. (2009), ElGawady et al. (2009) and ElGawady and Sha'lan (2010).

Chou and Chen (2006) provided one of their columns with a dog bone shaped external energy dissipater. They reported that it increased the equivalent viscous damping of the system from 6.5% to 9%.

Marriott et al. (2009) used two different layouts of external energy dissipater systems for segmental columns. They used mild steel bars encased in steel confining tubes and injected with epoxy to have a fuse-like behavior and to be able to dissipate energy while subjected to tension and compression stresses.

ElGawady et al. (2009) and ElGawady and Sha'lan (2010) used external steel angles and rubber pads respectively as external energy dissipaters and isolation dissipation devices. The idea of the steel angles is the same as with other metal dissipaters: energy is dissipated by the yielding of the steel. On the other hand, rubber dissipates energy in another way, as the soft rubber changed the energy dissipation function from a discrete function occurred at every impact between the rocking segments to a continuous function ElGawady et al. (2005 and 2006).

Both internal and external energy dissipaters increased the dissipation of hysteretic energy. The fuses had the advantage of being easily changed and, hence, not increasing the residual drift of the system. Use of the rubber isolation pads significantly decreased the initial stiffness.

2.2 Concrete Confinement

Mander et al. (1988) developed a theoretical model to predict the stress-strain of concrete confined using steel stirrups and/or jackets.

In recent years, external confinement of concrete using FRP composites has emerged as a popular method of both column retrofit and new construction, particularly for circular columns. Various models for predicting stress-strain behavior have been developed (e.g., Samaan et al. (1998), Fam and Rizkalla (2001), Becque et al. (2003), Lam and Teng (2002 & 2003), Jiang and Teng (2007) and Teng et al. (2009)).

Confinement increases element ductility and the ultimate strength of the elements. If used in a tubular shape, confinement can be a permanent formwork which can save the time and money spent preparing temporary formworks.

2.3 Conclusions

- Experimental studies show that the permanent deformation of SPPT is minimal compared to that of RC columns.
- Experimental studies show the limited ability of the system to dissipate input seismic energy so additional energy dissipaters were used.
- Energy dissipaters are important for the SPPT system. External fuses don't increase the residual drift, but internal fuses do.
- The simple analytical models can't yet be generalized and need more efforts to be more accurate.
- 2D and 3D FE modeling is essential in understanding the behavior of the system under different loading patterns. A combination of FE modeling and FS/SDFS models can be an extremely powerful tool to compute the dynamic response of the system without running expensive experimental testing. However, first, we must develop a systematic way of preparing a FE model for the system.

2.4 References

- Booker, A. J. (2008). “Performance of continuous and segmented post-tensioned concrete filled fiber tubes.” M.Sc. thesis, Washington State Univ., WA, USA
- Chang, K. C., Loh, C. H., Chiu, H. S., Hwang, J. S., Cheng, C. B., and Wang, J. C. (2002). “Seismic behavior of precast segmental bridge columns and design methodology for applications in Taiwan”, Taiwan Area National Expressway Engineering Bureau, Taipei, Taiwan in Chinese.
- Chou, C.-C., and Chen, Y.-C., (2006). “Cyclic tests of post-tensioned precast CFT segmental bridge columns with unbonded strands” J. Earthquake Engng. Struct. Dyn., 35, 159-175.
- Chou, C.-C., and Hsu, C.-P.,(2008).”Hysteretic model development and seismic response of unbonded post-tensioned precast CFT segmental bridge columns.” J. Earthquake Engng. Struct. Dyn., 37, 919-934.
- ElGawady, M., Booker, A.J., and Dawood, H., (2009). “Seismic behavior of post-tensioned concrete filled fiber tubes. ” J. Composites for Construction, ASCE, (in press)
- ElGawady, M., and Sha’lan, A., (2010- In review). “Seismic behavior of self-centering bridge bents”, ASCE, Journal of Bridge Engineering.
- Hewes, J. T., and Priestley N. (2002). “Seismic design and performance of precast concrete segmental bridge columns.” Report No. SSRP-2001/25, Univ. of California at San Diego.
- Kwan,W.-P., and Billington, S. L. (2003). “Unbonded posttensioned concrete bridge piers. I: Monotonic and cyclic analyses.” J. Bridge Eng., 8(2), 92–101.
- Kwan,W.-P., and Billington, S. L. (2003). “Unbonded posttensioned concrete bridge piers. II: Seismic analyses.” J. Bridge Eng., 8(2), 102–111.
- Marriott., D., Pampanin, S., and Palermo, A., (2009). “Quasi-static and pseudo-dynamic testing of unbonded post-tensioned rocking bridge piers with external replaceable dissipaters” J. Earthquake Engng. Struct. Dyn., 38, 331-345.
- Ou, Y.-C., Chiewanichakorn, M., Aref, A. J., and Lee, G. C. (2007). “Seismic performance of segmental precast unbonded posttensioned concrete bridge columns.” J. Str. Eng., 133(11), 1636-1647.
- Sha’lan, A. (2009). “Performance of re-centering moment resisting frames composed of continuous and segmented precast post-tensioned concrete columns confined by FRP tubes” M.Sc. thesis, Washington State Univ., WA, USA

CHAPTER 3

BEHAVIOR OF SEGMENTAL PRECAST POST-TENSIONED BRIDGE PIERS UNDER LATERAL LOADS: EXPERIMENTAL AND MODELING

3.3 Introduction

Correctly designed and detailed reinforced concrete structures, under the prevailing capacity design concepts, are anticipated to exhibit inelastic response leading to structural damage and permanent residual drift angles at the conclusion of severe ground motion excitations. This leads to long-term closure of highways while expensive retrofits, or even complete replacements, are carried out. Following the Kobe earthquake (Japan 1995), over 100 reinforced concrete bridge columns were demolished due to a residual drift angles in excess of 1.5% (Lee and Billington 2010).

Recent research on the seismic behavior of segmental precast post-tensioned (SPPT) bridge piers has shown that they display less residual displacement and damage when compared to conventional reinforced concrete (RC) bridge piers (e.g., Hewes 2002, Ou et al. 2007, Marriott et al. 2009, ElGawady et al. 2010 and ElGawady and Sha'lan 2010). The potential benefits of using precast post-tensioned structural elements in high seismic zones were highlighted in the U.S. PRESSS research program where a self-centering system was implemented with precast elements demonstrated superior seismic performance (Priestley et al. 1999).

A segmental precast pier consists of precast segments stacked one on top of each other. The segments are connected by unbonded post-tensioning tendons passing through a duct cast in the segments during fabrication. The pier's segments will rock back and forth during ground

motion excitation and re-center upon the shaking termination as a result of the restoring force provided by the post-tensioning.

The effect of pier aspect ratio, applied initial post-tensioning force, applied external axial load, and solid or hollow core cross sections as well as confinement of the segments using steel stirrups, steel tubes, and/or fiber reinforced polymer tubes on the seismic performance of SPPT piers has been investigated (e.g. Chang et al. 2002, Hewes 2002 and Ou et al. 2007, Marriott et al. 2009, ElGawady et al. 2010(a), ElGawady et al. 2010(b), and ElGawady and Sha'lan 2010). These studies showed that SPPT piers were capable of withstanding large nonlinear displacements without experiencing significant or sudden loss of strength. The nonlinear behavior resulted not only from material nonlinearity, like in a conventional RC system, but also from geometric nonlinearity resulted from opening of the interface joints between segments as well as between the bottommost segment and the foundation. The significant contribution of the geometric nonlinearity to the nonlinear behavior of the SPPT piers resulted in smaller damage and residual displacement compared to their counterparts RC piers at a given lateral drift angle.

Currently, SPPT pier construction is an economic option to accelerate bridge construction in regions of low seismicity in the USA. Examples of bridges constructed with segmental columns include the Louetta Road Overpass (SH-249, Texas), Linn Cove Viaduct (Grandfather Mountain, North Carolina), Sunshine Skyway Bridge (I-275, Florida), Varina-Enon Bridge (I-295, Virginia), John T. Collinson Rail Bridge (Pensacola, Florida), Seven Mile Bridge (Tallahassee, Florida), and the Chesapeake and Delaware Canal Bridge (St. Georges, Delaware). However, the applications of this construction system in moderate to high seismic regions in the USA are limited due to concerns about its seismic response and low energy dissipation capabilities.

In an effort to increase the energy dissipation capacity of SPPT piers, researchers have investigated the influence of internal bonded mild steel bars at the interfaces between the segments as well as between the bottommost segment and foundation (Chang et al. 2002). However, the yielding of the mild steel bars increased residual displacements and damage compared to piers without mild steel. External energy dissipaters “fuses” have also been investigated as a means of enhancing energy dissipation (Chou and Chen 2006, Marriott et al. 2009, Rouse 2009, ElGawady et al. 2010(a), ElGawady et al. 2010(b), and ElGawady and Sha’lan 2010). These external simple yield-dissipaters significantly increased the energy dissipation with minor effects on the residual displacement of the system.

This paper presents a detailed three-dimensional (3D) finite element (FE) model developed using ABAQUS/Standard version 6.8-2 to capture the backbone curves of SPPT piers. The paper starts with a detailed description of the FE model including the element types used, material constitutive models, loading patterns, boundary conditions, and contact interaction properties. Then, a discussion of an experimental study conducted on eight large-scale SPPT piers subjected to static-cyclic loading is presented. The developed model was validated against the results of this experimental research. Finally, sensitivity analyses were carried out.

3.4 Finite Element Modeling of Self-Centering Piers

ABAQUS/Standard version 6.8-2, a general-purpose finite element code, was selected as a basic platform for this study. For the simulation of the SPPT pier system a built-in first-order full integration 8-node linear brick element (C3D8) was used to represent the concrete and the confining material in the model (Fig. 3.1). A 2-node linear beam element in space (B31) was used to simulate the post-tensioning tendon. The mesh size was selected based on a sensitivity

analysis such that the analyses converge to the same output while maintaining a reasonable computation effort.

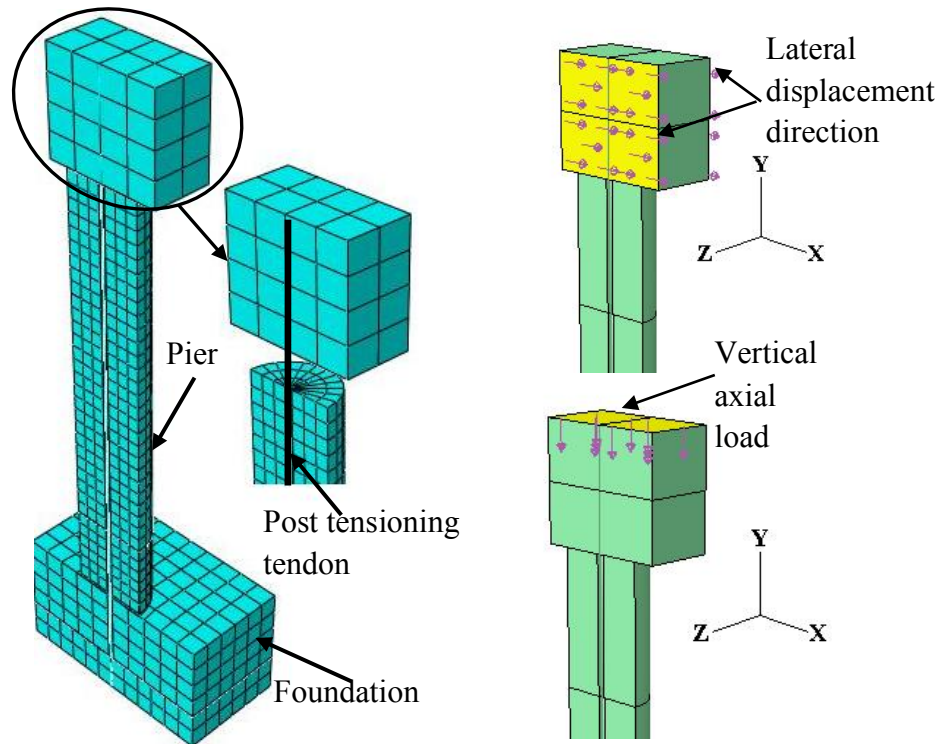


Figure 3.1: A typical mesh and applied loads and displacements for the SPPT pier.

Concrete damaged plasticity and concrete smeared cracking are the two models available in ABAQUS/Standard 6.8-2 to model concrete material behavior. The concrete damaged plasticity model (Lubliner et al. 1989 and Lee and Fenves 1998) assumes that the main two concrete failure mechanisms are the tensile cracking and compression crushing of the concrete material. Crack propagation is modeled by using continuum damage mechanics, i.e., stiffness degradation. The damaged plasticity model was selected to be used in this study since it has higher potential for convergence compared to concrete smeared cracking. Moreover, the concrete damaged plasticity model is designed for applications in which the material is subjected to

monotonic, cyclic, and/or dynamic loading, which gives the model the potential to be applied under different loading types.

To fully define the concrete material it is required to define material density, young's modulus, Poisson's ratio and the concrete damaged plasticity model parameters. The definition of the concrete damaged plasticity model requires the definition of the plasticity parameters, as well as, compressive and tensile behavior. The five plasticity parameters are: the dilation angle in degrees, the flow potential eccentricity, the ratio of initial equibiaxial compressive yield stress to initial uniaxial compressive yield stress, the ratio of the second stress invariant on the tensile meridian to that on the compressive meridian, and the viscosity parameter that defines viscoplastic regularization. The aforementioned parameters were set to 1°, 0.1, 1.16, 0.66, and 0.0, respectively. The values of the last four parameters were recommended by the ABAQUS documentation for defining concrete material (ABAQUS version 6.8 documentation- SIMULIA 2008). The dilation angle was chosen to be unity to give stability to the material model while minimizing the confinement effect of the material as the confinement effects were taken independently into consideration while getting the stress strain curves of the confined concrete. For a given concrete characteristic compressive stress at 28 days (f'_c) and confinement characteristics (thickness, material's type, and properties) the concrete stress strain curve in compression can be developed using a suitable confined concrete model. (e.g., Mander et al. 1988, Samaan et al. 1998, Fam and Rizkalla 2001, Beque et al. 2003, and Teng et al. 2009).

The concrete young's modulus can be either measured according to ASTM (C469) or calculated using Eq. 3.1 (ACI318-2008).

$$E_c = 4733 \sqrt{f'_c} \text{ MPa} [57,000 \sqrt{f'_c} \text{ psi}] \quad (\text{Eq. 3.1})$$

The concrete behavior in tension was modeled using a linear elastic approach until cracking is initiated at f'_t where f'_t is defined using Eq. 3.2 (ACI318-2008), followed by a horizontal plateau. This horizontal plateau was used to improve the numerical stability and convergence of the model (Wight 2006).

$$f'_t = 0.62276 \sqrt{f'_c} \text{ Mpa} \quad [7.5 \sqrt{f'_c} \text{ psi}] \quad (\text{Eq. 3.2})$$

The concrete compressive and tensile behaviors were inputted to the program using a tabulated form of yield stress versus inelastic strain and yield stress versus cracking strain respectively (ABAQUS version 6.8 documentation- SIMULIA 2008).

The constitutive model used to simulate the steel tendons and steel jackets was the classical metal plasticity model. An idealized elasto-plastic stress strain curve for each material was developed and used as the input for the ABAQUS model. The input for the classic metal plasticity model includes density, young's modulus, Poisson's ratio and the yield stress versus plastic strain submitted in a tabular form.

The three translational (U_x , U_y , U_z) degrees of freedom (DOF) were constrained for all the nodes at the bottom surface of the foundation (Fig. 3.1). Since the column is symmetric with respect to an XY plane, a symmetry (ZSYMM) boundary condition was used along the plane of symmetry to reduce the analyses time.

The post-tensioning tendons in the model are embedded at the top into a loading stub representing the bridge superstructure and at the bottom into the foundation (Fig. 3.1). The normal contact behavior between the concrete surfaces and between the confining steel tube and the concrete segments was modeled using the default constraint enforcement method with a hard contact pressure-over closure having finite sliding with node to surface as the discretization

method. The penalty method was chosen to formulate the tangential contact behavior between different surfaces of the model.

Three loading steps were used for the analysis of the models. During the first step, a post-tensioning force was applied using a stress-type initial condition to the tendons. During the second step, the gravity load was applied as a traction force applied to the top surface of the model in the negative y-direction (Fig. 3.1). The third loading step consisted of a monotonic push in the x-direction simulated by a linearly increasing lateral displacement until the failure of the model occurs and the analysis was not able to proceed any further.

3.5 Experimental work

3.5.1 Test pier design details

Four large-scale precast concrete segmented piers (Table 3.1) were constructed and tested at the Powell Structural Research Laboratories on the University of California at San Diego (UCSD) to investigate their strength – deformation characteristics and failure modes under simulated lateral seismic loading (Hewes 2002). The following primary features were investigated in the experimental program: (1) Pier aspect ratio, (2) Lateral confinement level at the maximum moment location, (3) Initial tendon stress, and (4) Damage reparability. The piers were circular in cross-section with diameter of 610 mm [24 in], and the main longitudinal reinforcement in each pier consisted of a single unbonded concentric tendon comprised of 27 – 12.7 mm [0.5 in] diameter ASTM A779 Grade 270 (1860 MPa [270 ksi]) low-relaxation steel prestressing strands with a total cross-sectional area of 2665 mm² [4.13 in²]. Two test piers had an aspect ratio (AR) of 6, and the other two piers had AR = 3, where aspect ratio is defined as the height between point of lateral loading and pier base divided by pier diameter.

Table 3.1: The matrix of the experimental work

Pier	Pier aspect ratio	No. of segments	Steel jacket thickness	Initial tendon's stress / ultimate tendon's tensile stress	Measured post-tensioning stress MPa [psi]
JH11 [*]	6	4	6.0 mm [0.24 in]	40%	1021 [148,090]
JH12 ^{**}				60%	1215 [176,238]
JH21 [*]	6	4	2.8 mm [0.11 in]	40%	801 [116,200]
JH22 ^{**}				60%	946 [137,210]
JH31 [*]	3	2	2.8 mm [0.11 in]	40%	773 [112,114]
JH32 ^{**}				60%	1020 [147,939]
JH41 [*]	3	2	6.0 mm [0.24 in]	40%	779 [112,984]
JH42 ^{**}				60%	1002 [145,328]

^{*} Virgin specimens

^{**} Retested specimens after retrofitting

The bottommost segment of each pier utilized an ASTM A569, A36 steel jacket to provide the relatively high level of lateral confinement which is required due to the high compression strains associated with a pier rocking about its base. For each aspect ratio, one pier used a jacket with a transverse volumetric reinforcing ratio of $\rho_v = 1.9\%$ and the other with $\rho_v = 3.9\%$. The steel jacket terminated approximately 25 mm [1.0 in] above the bottom of the segment to prevent the jacket from bearing on the footing during testing. The height of the steel jackets in all piers was selected such that spalling of cover concrete in the non-jacketed segments above it would be avoided. The jacketed segments did not contain any longitudinal reinforcement other than the prestressing tendon. Table 3.2 gives the jacket tensile properties and Table 3.3 gives the concrete compressive strength measured for each pier at the 28th day and the day of testing.

Table 3.2: Summary of steel coupons tension tests

Columns	Description	Size	Yield Strength (MPa)	Ultimate Strength (MPa)
JH1 and JH2	Thin coupons	2.9 mm thick	283 ± 7	390 ± 7
	Thick coupons	6.2 mm thick	303 ± 3	464 ± 3
JH3 and JH4	Thin coupons	2.8 mm thick	290	364
	Thick coupons	6.0 mm thick	317	463

Table 3.3 Concrete compressive strength for test units (fc', MPa)

Pier	28-Day	Day of Test 1	Day of Test 2
JH1	44.0 ± 0.3	48.7 ± 0.6	57.0 ± 1
JH2		50.8 ± 1.1	55.5 ± 1
JH3	48.5 ± 1.1	57.3 ± 1.6	57.1 ± 0.8
JH4		58.1 ± 1.1	57.8 ± 1.7
Footing	49.5 ± 1	61.4 ± 1	--

All other pier segments above the base segment used traditional transverse spiral rebar for lateral confinement. The transverse spiral was Grade 60 #3 bar spaced at 75 mm [3.0 in] and 150 mm [5.9 in] for piers with AR = 6 and AR = 3, respectively. The upper non-jacketed segments also contained eight Grade 60 #4 longitudinal bars spaced evenly around the perimeter of the section with a cover of 25.4 mm [1.0 in]. Test piers JH1 and JH2 had a total of four precast columns segments while JH3 and JH4 had two precast segments each. The unbonded tendon length was $L_t = 4953$ mm [195 in] for JH1 and JH2, while that for JH3 and JH4 was $L_t = 3137$ mm [123.5].

In order to investigate the influence of initial tendon stress level on pier behavior, and to evaluate how well a pier could be repaired after a seismic event, each pier was tested twice. The first test on each pier was conducted at a given initial tendon stress, and then each pier was

inspected, repaired, and post-tensioned to a higher initial tendon stress level for the second test. Table 3.1 provides a summary of test pier data including initial tendon stress level.

3.5.2 Test setup, instrumentation, and loading protocol

A schematic representation of the test setup is shown in Fig. 3.2. Pier footings were connected to the laboratory strong floor by six high strength post-tensioning bars, and a cyclic lateral point load was applied at the pier top by a servo-controlled hydraulic actuator reacting off the laboratory strong wall. Horizontal load levels in the actuator were monitored using a load cell, and the horizontal displacement at the actuator level was measured using a displacement transducer and reference column. A constant axial compressive force of 890 kN [200 kips] was applied to the piers to simulate gravity service loads.

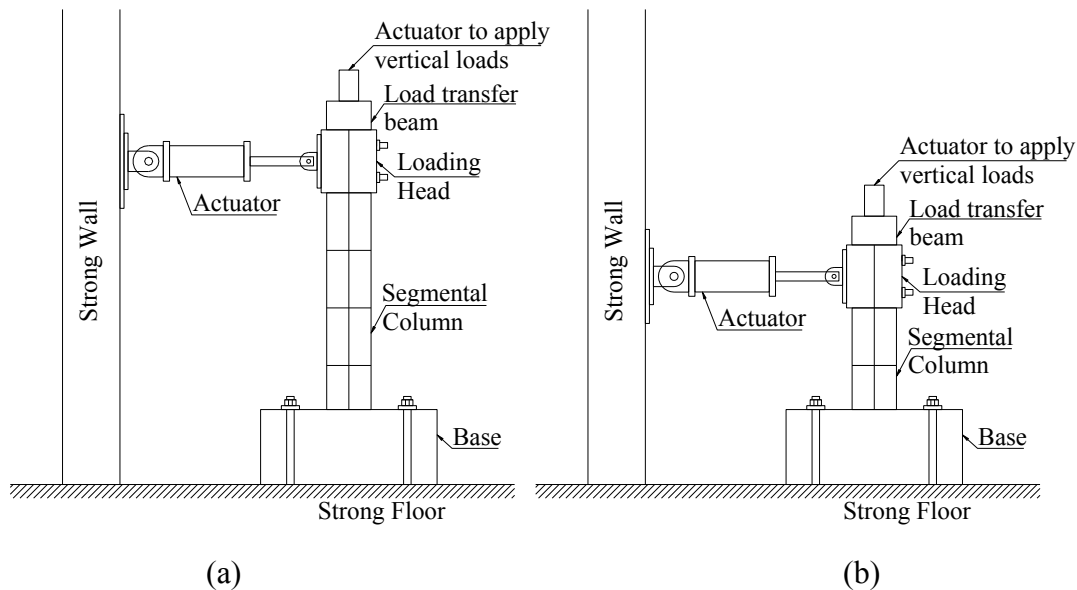


Figure 3.2: Test setup for specimens
 (a) Specimens (JH11/JH12/JH21/JH22), and (b) Specimens (JH31/JH32/JH41/JH42).

The first few cycles of each test were conducted in the elastic range under force control, with one cycle each performed at one-half, one, and one and a half times the theoretical force to cause decompression of the extreme tension fiber at the pier base. Subsequent cycles during the

test were conducted in displacement control, with three full displacement reversals conducted at increasing amplitudes. Since each column was to be tested twice, it was desired to limit the damage in the first test of each column to an amount that could be repaired relatively easily. Thus the maximum drift imposed during the first test of each specimen was dictated by the observed damage at a particular drift.

3.5.3 Description of test results

All test piers exhibited ductile flexural response up to the maximum imposed drift of each test, as is visible in the hysteretic force – displacement response plots shown in Figs. 3.3 and 3.4. A prominent feature of piers with unbonded tendons is the reentering tendency, which also implies less hysteretic energy dissipation compared to a traditional reinforced concrete column. Initial concrete crushing was observed at the region in the bottommost segment between the bottom of the steel jacket and top of footing at a drift angle of 1.2% for all piers during their first test. However, the extent of spalling was minor and the damage to this region was very limited during the first tests. After drift angle levels of about 0.5%, pier top displacement was observed to be primarily due to rotation of the pier about the compression toe. This was evidenced by a large flexural crack opening of the interface joint between the pier and its foundation with no significant flexural crack openings above the footing level.

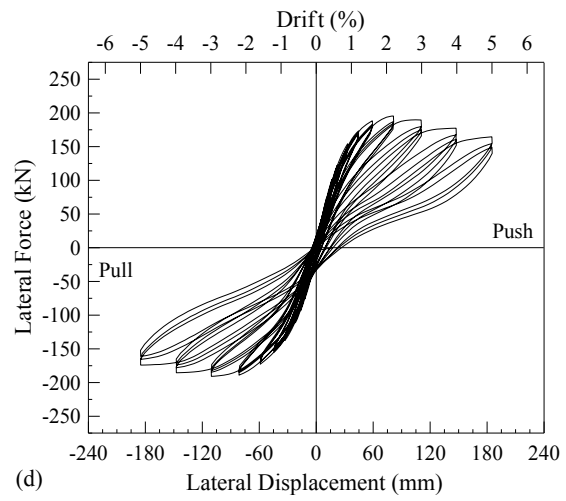
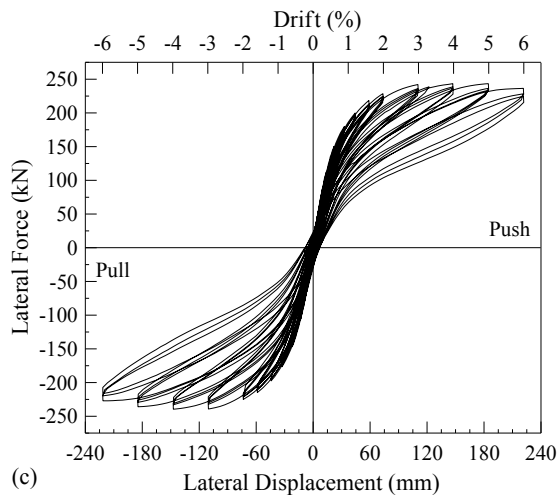
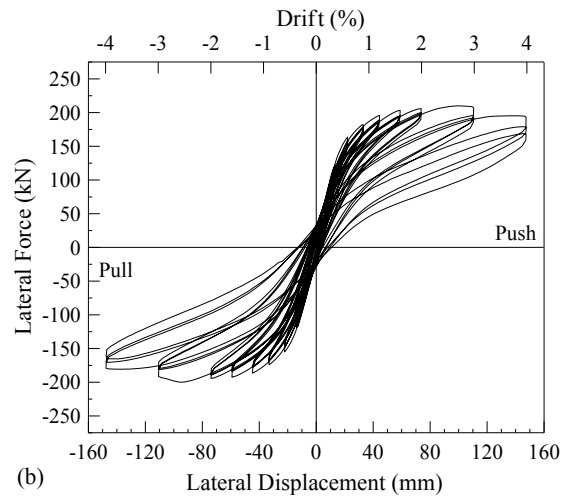
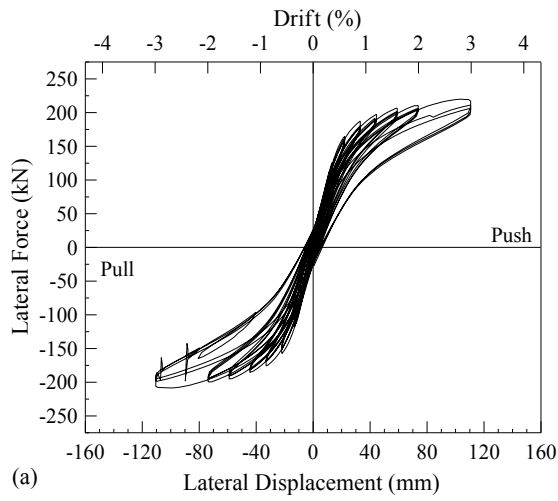
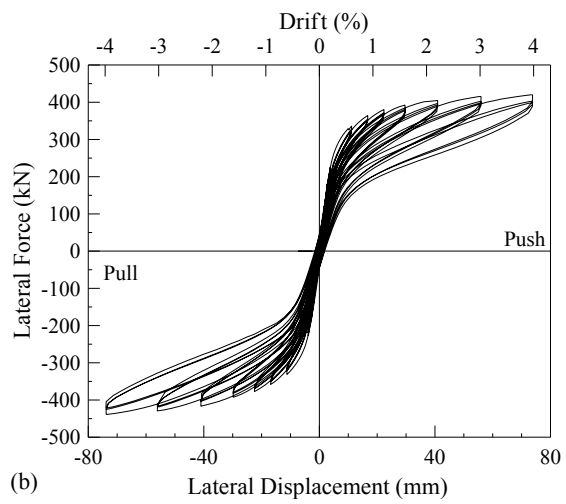
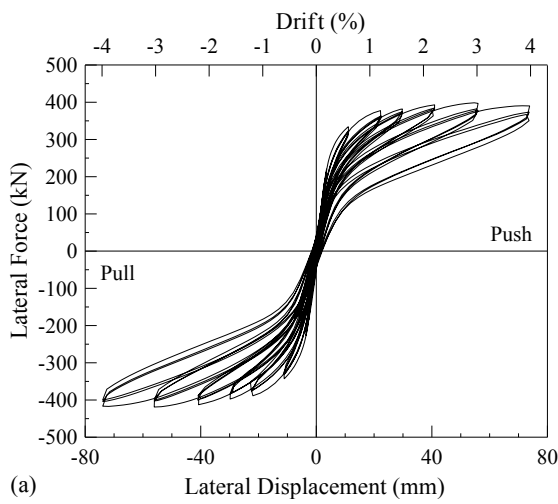


Figure 3.3: Experimental hysteretic response plots: (a) JH11; (b) JH21; (c) JH12; and (d) JH22



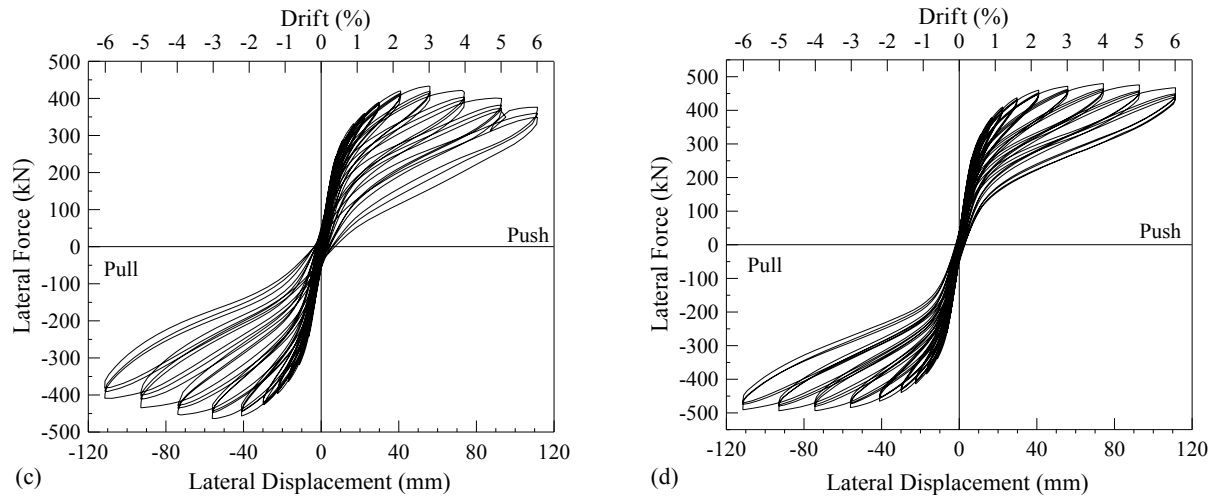


Figure 3.4: Experimental hysteretic response plots: (a) JH31; (b) JH41; (c) JH32; and (d) JH42

During the first tests on piers JH1 and JH2 ($AR = 6$), crushing of cover concrete in the segment directly above the jacketed segment was observed at lateral drift angles of 3.0%, and 4.0%, respectively. The first tests for these piers were stopped at these drift levels. Piers with $AR = 3$ were taken to a maximum lateral drift angle of 4.0% during the first tests. No spalling of cover concrete above the jacketed segment was observed for piers JH3 and JH4. Visible damage to JH3 and JH4 at the end of the first tests consisted of only minor crushing of concrete at the gap between steel jacket and top of footing. For all piers, a residual gap opening on each side of the section at the column base (i.e. the compression toe region) existed at the end of testing as a result of very high compression strains and concrete crushing. Residual pier drift angles at the end of testing were on the order of 0.1% for piers JH1, JH3, and JH4, while that for JH2 was 0.30%.

The damaged regions at the pier base and above the jacket (piers JH1 and JH2) were repaired after the first test. Loose concrete was removed, and the regions were scrubbed with a wire brush, rinsed with water to remove any remaining concrete particles, and then allowed to dry. The spalled cover concrete above the steel jacket was reinstated by patching the area with a

non-sag polymer-modified, Portland cement mortar. The residual crack at the base of each pier was grouted using a high-modulus, low-viscosity, high-strength epoxy resin adhesive. After the spalled regions in piers JH1 and JH2 were repaired, the lower half of the second segment was wrapped with five layers of fiberglass in an effort to prevent spalling of cover concrete during the second test. Five layers of the Tyfo® Fibrwrap® SEH-51 fiber reinforced polymer (FRP) (Table 3.4) were applied. Each continuous band was installed with a 152 mm [6.0 in] minimum overlap back onto itself.

Table 3.4: Properties of the FRP

Tensile strength	3.24 GPa [470,000 psi]
Tensile modulus	72.4 GPa [10.5×10^6 psi]
Ultimate elongation	4.5%
Density	2.55 g/cm ³ [0.092 lb/in ³]
Thickness	0.36 mm [0.014 in]

The initial stiffness of the piers during their second test was much less than that predicted for an undamaged pier, indicating that the repair measures did not fully restore the piers to an undamaged state (see Figs. 3.3 and 3.4). However, the piers in general exhibited satisfactory lateral strength –deformation behavior. Piers JH1, JH3 and JH4 achieved a maximum drift angle of 6% while testing of JH2 was terminated at 5% drift angle. The 6% maximum imposed drift during testing corresponded to the maximum displacement limit of the test setup. Comparing the second test hysteretic responses (Figs. 3.3 and 3.4 (c) and (d)), it is seen that piers with the higher jacket confinement level (JH1 and JH4) experienced less damage at their bases, achieved higher lateral strengths, and showed less stiffness and strength degradation at high drifts. Pier JH1 (AR=6) experienced a 6% decrease in lateral strength going from 5% drift to the maximum imposed drift, while JH4 (AR=3) did not show any reduction in strength up to the maximum

imposed drift angle level. Specimen JH2 experienced a 20% decrease in strength at maximum drift angle while JH3 suffered a 13% drop in lateral capacity at 6% drift angle. Residual drift angles for JH1, JH3, and JH4 at the end of the second testing were about 0.2%, while that for JH2 was 0.7%. No spalling of cover concrete above the steel jackets was observed during the second tests on the piers.

3.6 Model Validation

The sizes of the elements chosen for the concrete segments, concrete base, and upper loading stub were 94, 127, and 130 mm [3.7, 5 and 9 inches], respectively. The slender pier's model includes 1720 continuum elements, 174 beam elements and a total of 3086 nodes, while the squat piers' model includes 1072 continuum elements, 102 beam elements and a total of 1974 nodes.

The passive confining stresses imposed by the steel stirrups, steel tube, and the FRP sheets on the concrete core during loading alter its stress strain behavior by increasing both its peak strength and ductility. Through this study, Mander et al.'s (1988) and Samaan et al.'s (1998) models were used for developing the stress-strain behavior of concrete confined using steel and FRP wrapping, respectively.

The concrete compressive strengths in Table 3.3 were implemented in the model. Concrete was defined using a density of 2214 kg/m^3 [138 lb/ft^3] and a Poisson's ratio of 0.2. The stress strain curves in compression of the segments confined by thick steel tube, thin steel tube, steel stirrups and FRP is shown in Fig. 3.5. For more details about developing these curves and the ABAQUS input vectors refer to (Dawood 2010).

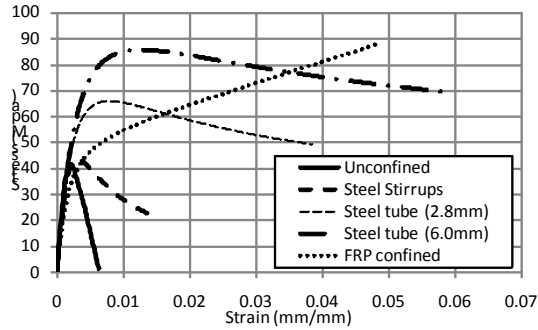


Figure 3.5: Stress strain curves for unconfined and confined concrete.

The steel tubes used to confine the lowermost segments in the specimens were defined using density of 7840 kg/m³ [0.28 lb/in³], Poisson’s ratio of 0.3, modulus of elasticity of 200,000 MPa [29000000 psi], while yield stress and ultimate stress were as shown in Table 3.2. The tendon material was modeled using a density of 7840 kg/m³ [0.28 lb/in³], Poisson’s ratio of 0.3, modulus of elasticity of 196,500 MPa [28,500 ksi], yield stress of 1690 MPa [245,000 psi] and ultimate stress of 1,730 MPa [270,000 psi]. The characteristics used for the FRP used for the retrofitted piers JH12 and JH22 are listed in Table 3.4.

Coefficient of frictions of 0, 0.5, and 0.5 were selected between the post-tensioning bar and the duct, steel tubes and segments’ surfaces, and two concrete surfaces respectively. An external axial vertical stress of 3.07 MPa [445 psi], corresponding to approximately 7.4% of f'_c , was applied to the top surface of the piers at the loading stub to represent the service load acting on the bridge’s superstructure.

3.7 Analyses results

The FE models were able to capture the behavior of the eight specimens described previously (Fig. 3.6). While applying the lateral load, the lateral displacement of the pier increased approximately linearly while all the interface joints between the different segments remained intact. This linear behavior continued until the normal stress under the heel of the pier

reached zero (neutral axis at the edge of the cross section). Beyond that, the first opening at the interface joint between the foundation and the bottommost segment was observed and softening in the stiffness was observed as well. While increasing the lateral load, the neutral axis continued to move through the pier's cross section towards its geometric centroid, and the opening of the interface joint between the bottommost segment and the foundation increased. Fig. 3.6(b) shows the discontinuity of the normal strains at the interface joints, which was, expected once the interface joints opened. Once the neutral axis reached the geometric centroid of the pier's cross section, more softening in the stiffness of the system occurred rapidly while the post-tensioning stresses increased rapidly. The same interface joint opening mechanism occurred at the second interface joint between the first and the second segments. However, the neutral axis didn't reach the geometric centroid of the pier at this interface joint. Fig. 3.7 shows the different bending stresses and openings at the different interface joints. This behavior is similar to what was observed during the experimental tests.

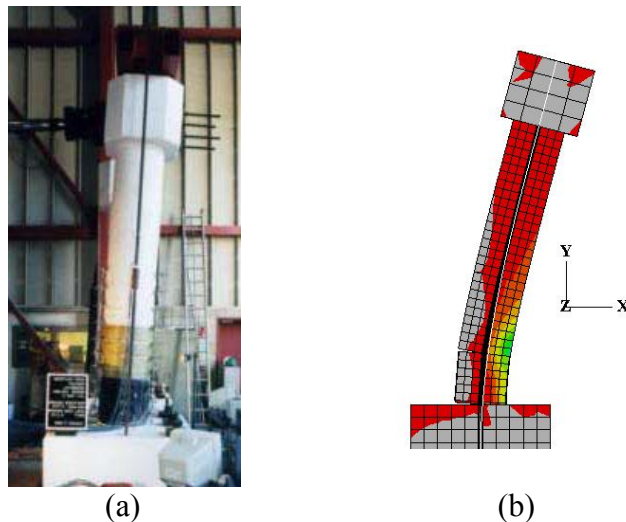


Figure 3.6: Specimen JH12 (a) during testing, and (b) FE model results.

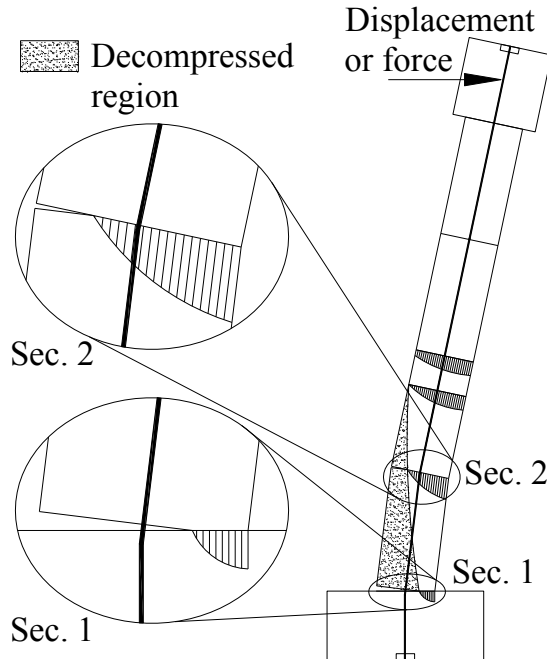
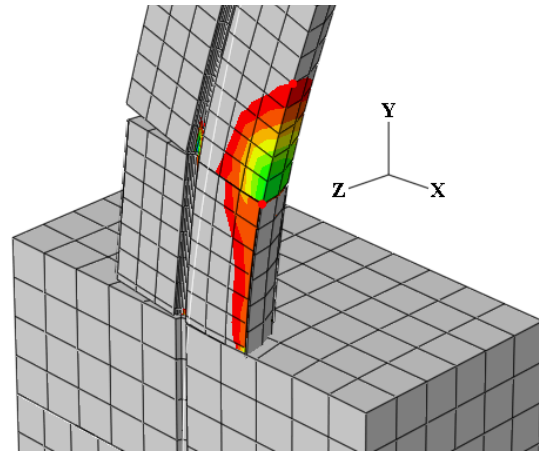


Figure 3.7: A schematic of a rocking pier indicating stresses and strains at different heights of the pier

The FE model was also capable of capturing the damage pattern of the system. For example, the experimental work showed spalling of the concrete cover of specimen JH11 along a height of approximately 406 mm [16 in] at a drift angle of 3%. During the FE analysis of JH11, stresses concentrations occurred at the bottom of the second segment, as well as at the top and bottom of the bottommost segment. At a lateral drift of 3%, since the bottommost segment was confined using the steel jacket; the segment was able to reach high strains without any potential concrete crushing. However, the second segment was a conventional RC segment and the strains in the concrete cover exceeded a potential spalling strain of 0.003 mm/mm along a height of approximately 533 mm [21 in] (Fig. 3.8(b)). Finally, it is worth noting that during the experimental work and at lateral drift of 3%, significant concrete crushing was reported. The analysis showed that the strength degradation of the pier started at a lateral drift of 2.5%.



(a)



(b)

Figure 3.8: Specimen JH11 at failure (a) experimental, and (b) analytical.

Figs. 3.9 and 3.10 show the predicted lateral forces versus drift angles and the experimental backbone curves of the slender and squat piers presented in the experimental section, respectively. As shown in the figures, the model was able to capture the general nonlinear behavior of all specimens. The model was able to capture the initial tangent stiffness of all piers. However, the stiffness degradation rate was under estimated for specimens JH12, JH22, JH32 and JH42. The aforementioned specimens were retest of specimens JH11, JH21, JH31 and JH41 after retrofitting and applying a higher post-tensioning stress. This shows that the behavior of the retrofitted piers was affected after the first testing due to micro cracks in the concrete and the retrofitting was not able to fully recover the concrete stiffness. The effect of these micro

cracks wasn't taken into consideration in the FE model. Pier JH11, unlike other piers, was tested up to a drift angle of only 3%, and consequently the extent of micro cracking in this specimen was not as significant. Hence, out of all the retrofitted specimens, the predicted stiffness degradation for the retrofitted column JH12 was much closer to the experimental study.

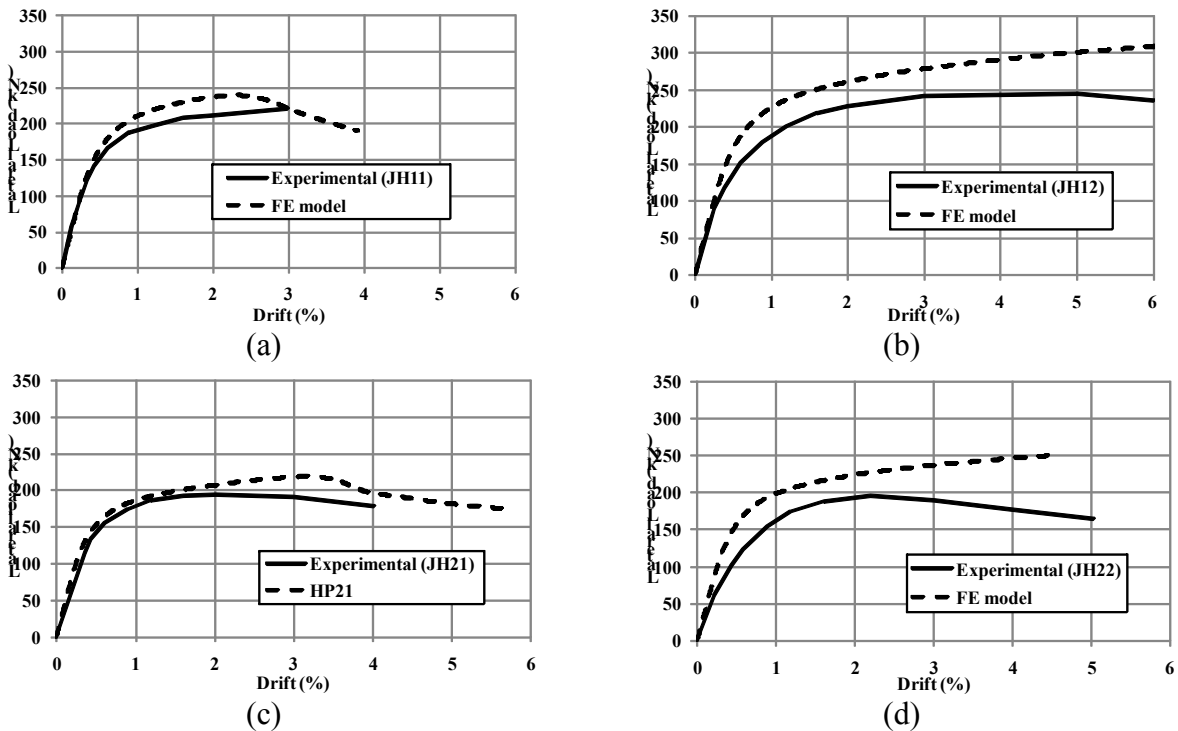


Figure 3.9: Experimental versus predicted backbone curves for slender virgin piers (left) and retested piers (right) (a) JH11, (b) JH12, (c) JH21, and (d) JH22.

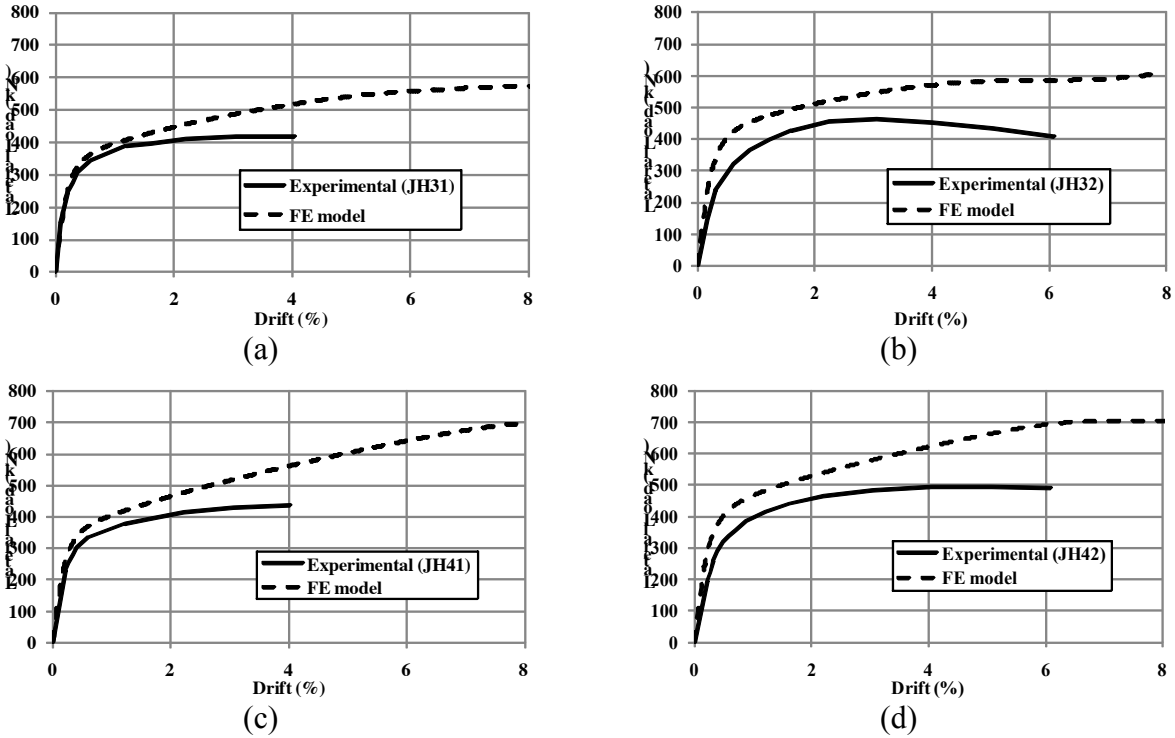


Figure 3.10: Experimental versus predicted backbone curves for squat virgin piers (left) and retested piers (right) (a) JH31, (b) JH32, (c) JH41, and (d) JH42.

Fig. 3.11 shows the error in predicting the lateral force for a given drift angle for each test specimen. The error is defined as follows:

Error in the lateral force (%) =

$$\frac{\text{Numerically determined lateral force} - \text{Experimentally measured lateral force}}{\text{Experimentally measured lateral force}} \% \quad (\text{Eq. 3.3})$$

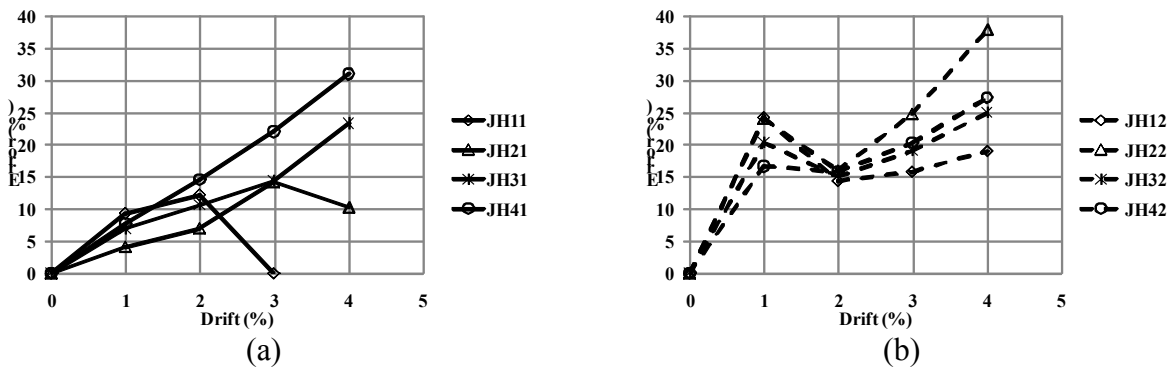


Figure 3.11: Errors in predicting the strengths of (a) virgin piers, and (b) retested piers

As the figure shows, the percentage of error increased with increasing the applied lateral drift angle. For slender specimens that were tested as virgin specimens (JH11 and JH21), the percentage of maximum error was approximately 14%. The error in predicting the strength of piers JH11 and JH21 started to decrease at drifts corresponding to the spalling of the upper segment's cover and it reached approximately 5% at the end of the tests. After retrofitting piers JH11 and JH21 and retesting as piers JH12 and JH22, the maximum percentage of error increased approximately to 17% and 37% for JH12 and JH22, respectively. As mentioned earlier, retrofitting was not able to fully recover the pier's mechanical properties as there were micro cracks that affected the performance of the columns, such micro cracks were not taken into consideration in the FE model. For virgin squat specimens i.e. piers JH31 and JH41, the percentage of error increased approximately linear with the applied lateral drift angle. At a drift angle of 4% the percentage of error reached 23% and 31% for JH31 and JH41, respectively. For specimens JH32 and JH42, the percentage of error for both was approximately 25% at a drift angle of 4%.

One important parameter for the performance of the SPPT piers is the level of post-tensioning force at different drift angle levels. Fig. 3.12 shows the drift angle level versus the percentage of error, defined by Eq. 3.4, in post-tensioning force. As shown in the figure, the FE model over predicted the post-tensioning forces in most cases. The percentage of error increased with increasing the drifts. Except for specimens JH41 and JH42, the error in predicting the post-tension stresses ranged from -6% to +5% for virgin specimens and from -3% to +4% for retested specimens. The error in predicting the post-tensioning force reached approximately 12% for specimens JH41 and JH42. This errors maybe due to a small deviation in defining the materials

characteristics and properties such as Young’s modulus of the tendon and the concrete, and spalling of the concrete at the toe in the experimental tests.

$$\text{Error in post-tensioning (\%)} = \frac{\text{Numerically determined PT} - \text{Experimentally measured PT}}{\text{Experimentally measured PT}} \% \quad (\text{Eq. 3.4})$$

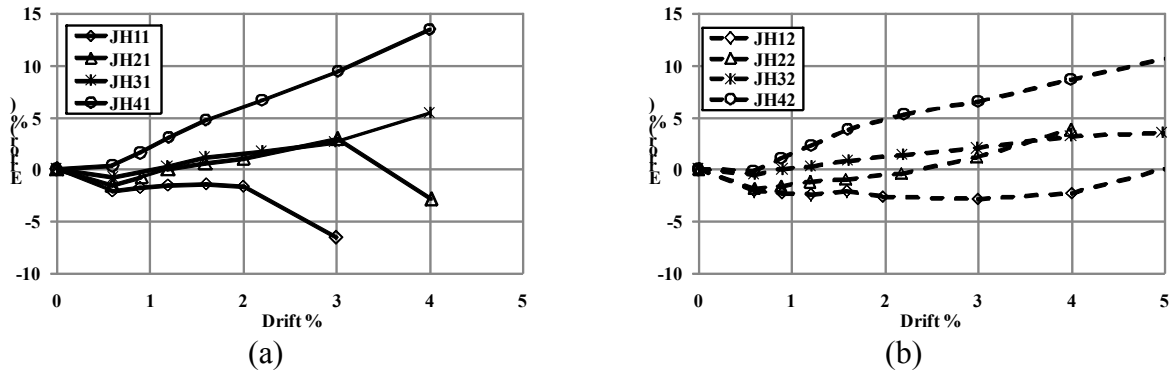


Figure 3.12: Error in post tensioning stress versus drift angle (a) virgin piers, and (b) retested piers

3.8 Sensitivity Analyses

As explained earlier, the mesh size was selected based on several analyses until the solution results converged at a given mesh size which was used in this study. In addition, the effects of confined concrete softening behavior, coefficient of friction between the concrete segments (μ_{c-c}) and coefficient of friction between the concrete and steel tubes (μ_{c-s}) on the predicted backbone curves were examined and presented in this section.

The softening behavior of concrete has an important role in the nonlinear response of RC structures. To investigate the effects of the softening behavior, three different slopes (Fig. 3.13) were implemented in the concrete behavior for the softening curve in the FE models of piers JH11 and JH21. The steepest softening curve is the one by Mander et al. (1988), while the other two softening behaviors were hypothetically assumed with milder stiffness degradations. The two hypothetical slopes were only used in this part of the research to explore the importance of the softening behavior of the concrete material on the ultimate strengths and displacements.

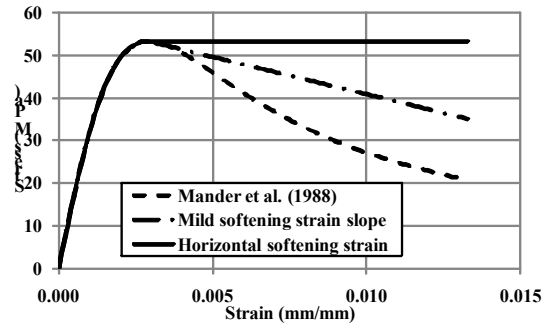


Figure 3.13: Different softening behavior of concrete

Fig. 3.14 shows the backbone curve for specimens JH11 and JH21 using the three different concrete material softening behaviors. As shown in Fig. 3.14, the softening behavior has a significant effect on the ultimate displacement of the investigated piers, as well as the slope of the descending branch of the piers after they reach their peak strengths. Decreasing the rate of the stiffness degradation, i.e. using milder slopes for the softening behavior of the confined concrete, increased the ultimate displacement and strength. Using horizontal softening behavior increased the ultimate displacement to be 175% and 183% of the ultimate displacement when using the steep softening behavior (Mander et al. 1988) for specimens JH11 and JH21, respectively, while in the case of mild softening behavior the ultimate displacement increased to approximately 150% of the ultimate displacement when using the steep softening behavior (Mander et al. 1988) for both specimens.

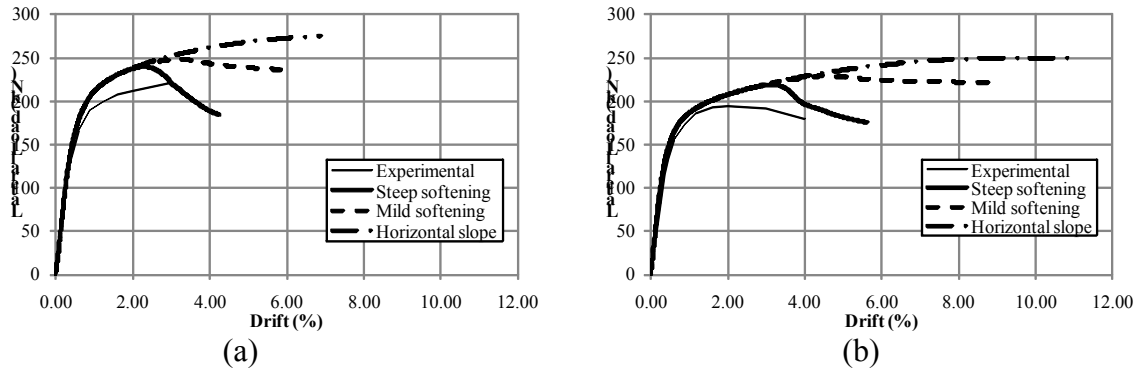


Figure 3.14: The effects of concrete material softening behavior on the response of piers (a) JH11, and (b) JH21

In this chapter a value of 0.5 was used for μ_{c-c} (coefficient of friction between concrete surfaces) and μ_{c-s} (coefficient of friction between concrete and steel surfaces). In this section values of 0.30, 0.50, 0.75 and 1.00 were used for μ_{c-c} , and values of 0.10, 0.30 and 0.50 were used for μ_{c-s} . The effect of the variation of μ_{c-c} and μ_{c-s} on the backbone curves is presented in Figs. 3.15(a) and 3.15(b), respectively. As shown in the figures, there is no effect of μ_{c-c} and μ_{c-s} on either displacement or the ultimate displacement of the piers. This matches the experimental observations where there was no sliding of the steel jacket or segments.

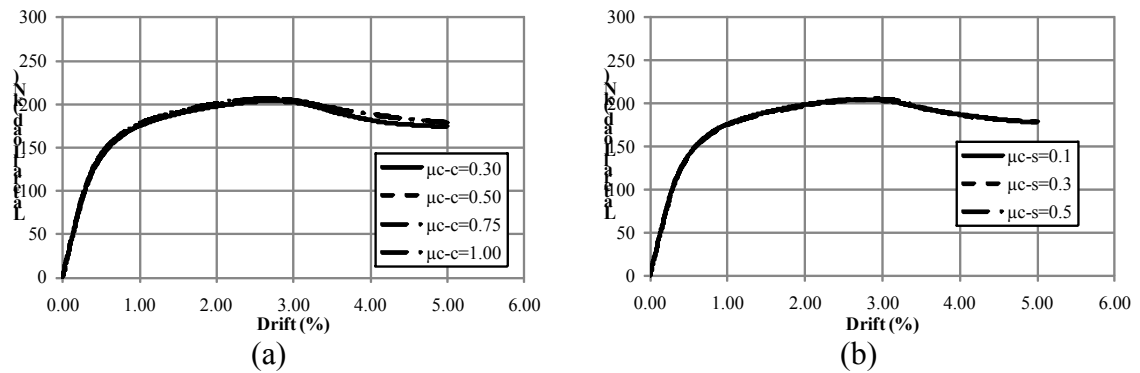


Figure 3.15: Effects of coefficients of friction on the backbone curves of pier JH11 (a) changing μ_{c-c} , and (b) changing μ_{c-s}

3.9 Findings and conclusions

This paper discusses the seismic behavior of the SPPT bridge piers. The piers consist of precast segments superimposed over each other and sandwiched between a reinforced concrete foundation and the bridge superstructure. The system is connected by unbonded post-tensioning tendons passing through ducts made in the segments during casting. The bottommost segments of the piers were encased in steel tubes to enhance its ductility. A FE model was developed, implemented and validated against experimental data. The analyses and experimental work presented in this study revealed that:

- The SPPT pier system is able to withstand large lateral drift angles with minimal damage and minimal residual displacements. The tested piers reached a lateral drift angle of approximately 4% with minimal damage in the form of spalling. After repairing this spalling and increasing the applied post-tensioning, the piers were able to reach a lateral drift greater than 5% before or at failure.
- Selection of the appropriate jacket height is a critical design parameter. For specimens JH1 and JH2, the height of jacket confinement was inadequate, leading to premature strength degradation of the test columns. A taller jacket would have postponed cover concrete spalling in the non-jacketed segments, thus reducing the amount of column damage requiring repair.
- As expected, decreasing the piers aspect ratios from 6 to 3, increased their initial stiffness and ultimate strength. In addition, increasing the applied post-tensioning force increased the ultimate strength of the test specimens.
- The FE model developed and presented in this paper was able to capture the backbone curves of the experimentally tested SPPT piers, and therefore could be used for

understanding the effects of the different parameters on the backbone curves of SPPT piers.

3.11 References

- ABAQUS Software and Documentation, Version 6.8-2. © Dassault Systèmes, SIMULIA, 2008.
- American Concrete Institute Committee 318, Building Code Requirements for Structural Concrete (ACI318-08) and Commentary (ACI318R-08). American Concrete Institute, Farmington Hills, MI.
- ASTM C469 (Standard test method for static modulus of elasticity and Poisson's ratio of concrete in compression).
- Beque, J., Patnaik, A. K., and Rizkalla, S., (2003), "Analytical models for concrete confined with FRP tubes" *J. Composites for Construction*, ASCE, 7(1), 31-38.
- Chang, K. C., Loh, C. H., Chiu, H. S., Hwang, J. S., Cheng, C. B., and Wang, J. C. (2002). "Seismic behavior of precast segmental bridge columns and design methodology for applications in Taiwan", Taiwan Area National Expressway Engineering Bureau, Taipei, Taiwan in Chinese.
- Chou, C.-C., and Chen, Y.-C., (2006). "Cyclic tests of post-tensioned precast CFT segmental bridge columns with unbonded strands" *J. Earthquake Engng. Struct. Dyn.*, 35, 159-175.
- Dawood, H. M., "Seismic Behavior of Segmental Precast Post-tensioned Concrete Piers", M.Sc. thesis, Washington State University, Washington, 2010
- ElGawady, M., Booker, A., Dawood, H. M. (2010- In press). "Seismic behavior of post-tensioned concrete filled fiber tubes", ASCE, *Journal of Composites for Construction*.
- ElGawady, M. A., Sha'lan A., and Dawood, H. M. (2010). "Seismic behavior of precast post-tensioned segmented frames", 9th U.S. National and 10th Canadian Conference on Earthquake Engineering (July 25-29, 2010).
- ElGawady, M., and Sha'lan, A., (2010- In review). "Seismic behavior of self-centering bridge bents", ASCE, *Journal of Bridge Engineering*.
- Fam, A. Z., and Rizkalla, S. H., (2001), "Confinement model for axially loaded concrete confined by circular fiber-reinforced polymer tubes" *ACI Str. J.*, 98 (4), 451-461.

- Hewes, J.T. “Seismic Design and Performance of Precast Concrete Segmental Bridge Columns.” Ph.D. Dissertation, University of California, San Diego, La Jolla, California. 2002.
- Lee, J., and G. L. Fenves, (1998) “Plastic-Damage Model for Cyclic Loading of Concrete Structures,” *Journal of Engineering Mechanics*, vol. 124, no.8, pp. 892–900.
- Lee, W. K., and Billington, S. L., (2009) “Modeling Residual Displacements of Concrete Bridge Columns under Earthquake Loads using Fiber Elements.”, *Journal of Bridge Engineering*, (in press).
- Lubliner, J., J. Oliver, S. Oller, and E. Oñate, (1989) “A Plastic-Damage Model for Concrete,” *International Journal of Solids and Structures*, vol. 25, pp. 299–329.
- Marriott, D., Pampanin, S., and Palermo, A., (2009). “Quasi-static and pseudo-dynamic testing of unbonded post-tensioned rocking bridge piers with external replaceable dissipaters” *J. Earthquake Engng. Struct. Dyn.*, 38, 331-345.
- Ou, Y.-C., Chiewanichakorn, M., Aref, A. J., and Lee, G. C. (2007). “Seismic performance of segmental precast unbonded posttensioned concrete bridge columns.” *J. Str. Eng.*, 133(11), 1636-1647.
- Mander, J. B., Priestley, M. J. N., and Park, R. (1988). “Theoretical stress-strain model for confined concrete.” *J. Struct. Eng.*, 114(8), 1804–1826.
- Priestley N., Sritharan S., Conley J., and Pampanin S., (1999) “Preliminary results and conclusions from the PRESSS five-story precast concrete test building.” *PCI Journal*, 44 (6):p. 42-76.
- Samaan, M., Mirmiran, A., and Shahawy, M. (1998). “Model of concrete confined by fiber composite.” *J. Struct. Eng.*, 124(9), 1025–1031.
- Teng, J. G., Jiang, T., Lam, L., and Luo, Y.Z., (2009), “Refinement of a design-oriented stress strain model for FRP-Confined concrete” *J. Composites for Construction*, ASCE, 13(4), 269-278.
- Wight, G. D. (2006) “Seismic Performance of a Post-tensioned Concrete Masonry Wall System.”, Ph.D. dissertation, University of Auckland, New Zealand.

CHAPTER 4

BEHAVIOR OF SEGMENTAL PRECAST POST-TENSIONED BRIDGE PIERS UNDER LATERAL LOAD: PARAMETRIC STUDY

Haitham Dawood¹ Mohamed ElGawady^{2§} Joshua Hewes³

This chapter discusses the design parameters that potentially affect the lateral seismic response of the segmental precast post-tensioned bridge piers. The piers consist of precast circular cross section segments stacked one on top of the other with concentric tendons passing through ducts made in the segments during casting. The bottommost segments of the piers were encased in steel tubes to enhance ductility and minimize damage. An FE model was used to investigate different design parameters and how they influence the lateral force – displacement response of the piers. Design parameters investigated include the initial post-tensioning stress as a percentage of the tendon yield stress, the applied axial stresses on concrete due to post-tensioning, pier aspect ratios, construction details, steel tube thicknesses, and internal mild steel rebar added as energy dissipaters. Based on the data presented, an initial tendon stress in the range of 40-60% of its yield stress and initial axial stress on concrete of approximately 20% of the concrete characteristic strength will be appropriate for most typical designs. These design values will prevent tendon yielding until a lateral drift angle of approximately 4.5%. Changing the steel tube thickness, height, or a combination of both proved to be an effective parameter that may be used to reach a target performance level at a specific seismic zone.

¹Graduate Research Assistant, Dept. of Civil and Environmental Engineering, Washington State University, Pullman, WA, hmousad@msn.com

² Assistant Professor, Dept. of Civil and Environmental Engineering, Washington State University, Pullman, WA, melgawady@wsu.edu;

[§]Corresponding author

³ Assistant Professor, Dept. of Civil and Environmental Engineering, Northern Arizona University, Joshua.Hewes@NAU.edu

4.3 Introduction

This chapter evaluates the effects of different design parameters on the backbone lateral force – displacement response of a segmental precast post-tensioned (SPPT) bridge pier. The standard pier investigated in this paper (see Fig. 4.1(a)) was similar in dimensions to pier JH11 tested by Hewes (2002) and described in detail in Dawood et al. (2010). The pier consisted of four concrete segments placed on top of each other and structurally connected using concentric unbonded tendon comprised of 27 – 12.7 mm [0.5 in] diameter ASTM A779 Grade 270 (1860 MPa [270 ksi]) low-relaxation steel strands with a total cross-sectional area of 2665 mm²[4.13 in²]. The pier was circular in cross-section with diameter of 610mm [24 in]. The pier has an aspect ratio (AR) of 6, where aspect ratio is defined as the distance between point of application of lateral loading and pier base divided by pier diameter. The unbonded tendon length was $L_t = 4953$ mm [195 in]. The pier was investigated under an initial post tensioning stress corresponding to approximately 45% of the yield strength of the tendons.

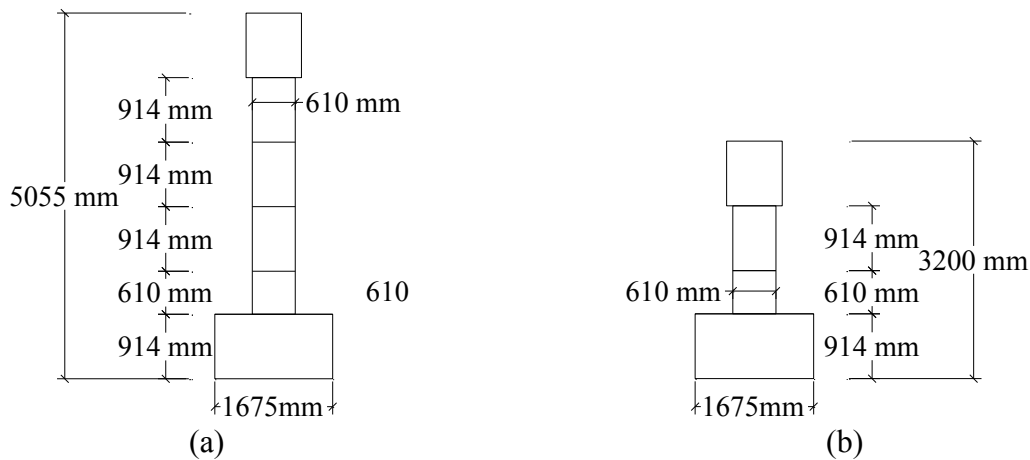


Figure 4.1: Detailed dimensions for (a) standard pier and (b) pier B

The bottommost segment of the pier utilized a 6.0 mm [0.24 in] thick, ASTM A569, A36 steel jacket to provide the relatively high level of lateral confinement which is required due to the high compressive strains associated with a pier rocking about its base. The steel jacket started

from the top of the bottommost segment and terminated approximately 25.4 mm [1.0 in] above its bottom to prevent the jacket from bearing on the footing during testing. This resulted in a jacket height of approximately 585 mm [23 in]. The steel used in jacketing the segment had yield and ultimate strengths of 317 [46 ksi] and 460 MPa [67 ksi], respectively. The jacketed segment did not contain any longitudinal reinforcement other than the post-tensioning tendons. The characteristic concrete compressive strength (f'_c) used was 41.4 MPa [6000 psi]. All other segments above the bottommost segment was modeled as a conventional reinforced concrete segment having transverse spiral of #3 of Grade 60 spaced at 75 mm [3.0 in] for lateral confinement. The upper non-jacketed segments had a concrete cover of 25.4 mm [1.0 in].

Throughout this chapter the standard pier was used for the analysis. However, to evaluate the effect of pier aspect ratio on pier response, a squat pier – namely “Pier B” – was also used in the investigation. The pier characteristics are identical to the standard pier in this chapter but with an aspect ratio of 3. It consisted of only two segments resulting in a clear height of 1524 mm [60 in] instead of 3354 mm [132 in] for the standard pier.

A detailed finite element model for the pier was prepared, validated, and presented by Dawood et al. (2010). Fig. 4.2 shows a summary of the detailed finite element pier model. This model was used to study the effects of six parameters on the force-displacement response of SPPT piers. The effects of tendon initial post-tensioning stress level (PT), initial concrete compressive stress due to post-tensioning (IS), pier aspect ratio (AR), different construction details of the system (CON), confinement thickness at pier’s base (CTh), and internal energy dissipating bars (IED) on the overall behavior of the system were investigated. Table 4.1 summarizes the different values assigned for each parameter. The range of these parameters was

selected to investigate a wide spectrum of values and doesn't necessarily reflect typical values to be used in practice.

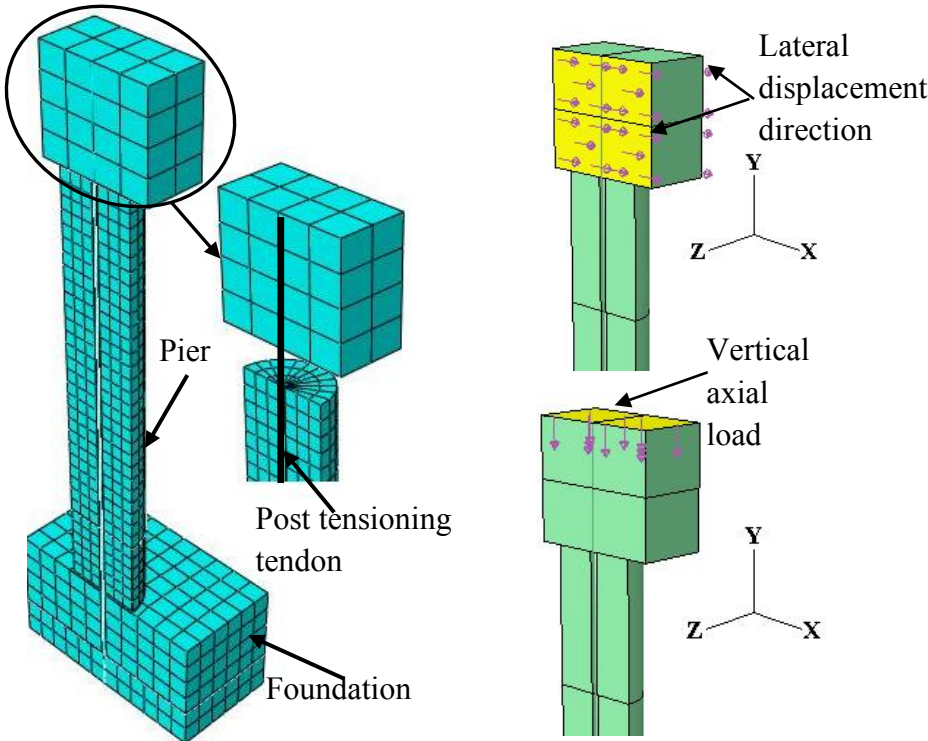


Figure 4.2: A typical mesh and applied loads and displacements for the SPPT pier.

Table 4.1: Different values assigned to each design parameter in the study

Series	Parameter	1	2	3	4	5	6	7	8
PT	Initial stress level as a percentage of tendon's yield stress (%).	30%	40%	45%	50%	60%	70%	80%	90%
IS	Stress on concrete induced by post-tensioning as a percentage of f'_c (%)	13%	16%	19%	22%	25%	28%	31%	-
AR	Aspect ratio of the piers.	3.0	4.5	6.0	7.5	9.0	-	-	-
CON	Different configurations of the system	See Fig. 4.14					-	-	-
CTh	Confinement thickness (mm)	6.0	4.5	3.0	1.5	-	-	-	-
IED	Reinforcement ratio of the mild steel used as internal energy dissipaters (%).	0.00	0.25	0.44	1.34	1.75	-	-	-

4.4 Results and Discussions

4.4.1 Effects of initial post-tensioning level in the tendon

The first parameter investigated in this study – the PT series – was the level of initial tendon stress. The initial post-tensioning stress ranged from 30% to 90% of the yield strength of the tendons while changing the cross sectional area from 4000 mm² [6.2 in²] to 1300 mm² [2.0 in²], respectively, to maintain the axial stresses on the concrete invariant at 7.17 MPa [1040 psi] which corresponds to 17% of f'_c . Fig. 4.3 shows the lateral drift at the loading point (middle of the loading stub) versus the measured the lateral resistance of the different piers. The lateral drift was defined as the ratio of the measured lateral displacement divided by the height of the loading point above the pier base. As shown in the figure, all the piers reached their ultimate strengths at a lateral drift angle of approximately 3%. Beyond that a gradual degradation in the strength occurred and the analysis ended at a lateral drift angle of 5%. At this drift level a reduction of approximately 14% occurred in the strengths of the piers. The analysis truncated due to spalling and compression failure at the bottom of the second segment.

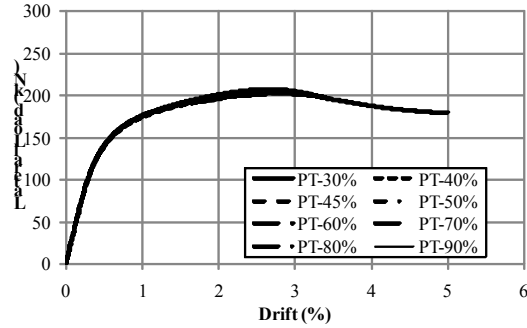


Figure 4.3: The effects of changing the initial post-tensioning stress in the tendons while keeping the same stress on concrete

Fig. 4.3 shows that changing the initial post tensioning stress in the tendon while maintaining constant initial axial stress on the concrete segments doesn't have a major effect on the backbone curve of the system. Surprisingly, in no case yielding of the tendon was observed. Since the post-tensioning tendon was placed in the geometric centroid of the pier, the increase in the tendon stress due to interface joints opening initiated after significant drift of the pier took place. Fig. 4.4 shows the lateral drift vs. the peak stress in the tendon for each pier. As shown in the figure, the increase in the tendon stress started at a lateral drift angle of approximately 1% and beyond that the increases in the post-tensioning stresses were quite small. The post-tensioning stresses reached their peak at a lateral drift of 3% when the piers reached their peak strength. Beyond that both the strengths of the piers and the stresses in the tendons started to decrease due to damage at the bottom of the second segments.

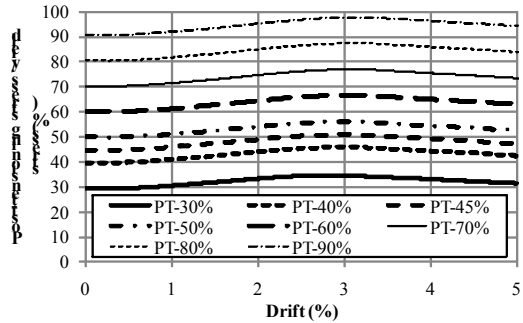


Figure 4.4: Drifts of different pier vs. the stresses in the post-tensioning tendons normalized by its yield stress

A second reason for the elastic response of the tendon was the relatively long unbonded length of the tendon. In the case of a squat pier, the unbonded tendon length will be relatively small and thus larger incremental tendon strains will occur with increasing the applied lateral displacement, resulting in potential yielding of the tendon if it was initially stressed to high initial stress levels. Fig. 4.5 shows the effects of the level of the initial post-tensioning stresses on the response of Pier B. Only three levels of initial post-tensioning stresses were investigated namely, 40%, 60%, and 80% of the yield stress of the tendon. Fig. 4.6 shows the peak stresses in the tendon versus the lateral drift angles of Pier B.

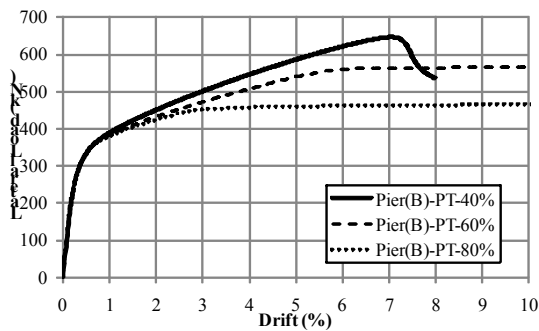


Figure 4.5: The effects of changing the initial post-tensioning stress in the tendons for squat piers

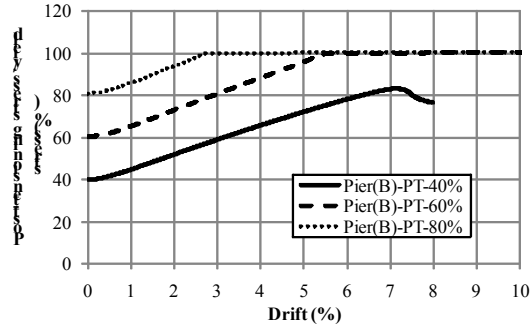


Figure 4.6: Drift of squat piers vs. the stresses in the post-tensioning tendons normalized by their yield stress

As shown in Figs. 4.5 and 4.6, increasing the initial post-tensioning stresses to 60% and 80% of the tendon yield stresses resulted in yielding of the tendon at lateral drift angles of 5.5%, and 2.5%, respectively. In addition, Fig. 4.6 shows that the increase in the tendon stresses started at small lateral drifts of approximately 0.2% which is significantly smaller than in the case of the more slender standard pier. Moreover, the rate of the strain increase in the post-tensioning is higher in the case of the squat piers compared to the slender piers. For small initial stresses of 40% of the yield stress, no yielding of the tendon was observed and the tendon reached a peak stress of approximately 82% of its yield stress followed by concrete crushing and the analysis stopped. Such crushing at high drift angle of 7% led to brittle failure as indicated in Fig. 4.5.

For initial tendon stresses of 40% of the yield stress (Fig. 4.5), the pier was able to develop a peak strength of 650 kN [146 kips] at a lateral drift angle of 7% where the concrete started to crush rupture and the analysis stopped at a lateral drift angle of 8%. For high initial stress in the tendons, the piers reached lateral strengths of 580 kN [130 kips] and 480 kN [108 kips] at lateral drift angles of 2.5% and 5.5% for initial post-tensioning stresses of 60 and 80% of the yield stress. Once the tendon yielded, the pier reached its peak strength and substantial decrease in the tangent stiffness of the system occurred. Based on these analyses and within the

scope of this study it appears that an initial post-tensioning stress in the tendon that range from 40 to 60% of the tendon yield stress is suitable for design. A squat pier ($AR=3$) with an initial post-tensioning stress of 60% of the tendon yield stress would reach yielding of the tendon at a lateral drift of 5.5%; however, such drift angle is beyond the anticipated level of drift angle for a typical bridge. Priestley et al. (2007) recommended a drift angle of 4.5% for a bridge at the collapse prevention limit state.

4.4.2 Effects of initial stresses on the concrete

The second parameter investigated in this study – the IS series – was the level of the initial axial compressive stress imposed on the concrete due to post-tensioning forces. This was achieved by maintaining the tendon's post-tensioning stress constant at 45% of its yield stress while changing the tendon cross-sectional area from 1980 mm² to 4990 mm² [3.07 in² to 7.73 in²]. This resulted in axial stresses in the concrete ranging from 5.38 MPa [780 psi] to 12.83MPa [1860 psi] which corresponds to 13% to 31% of f'_c .

Fig. 4.7 shows the lateral drift angle versus the lateral resistance of the piers with different initial stresses on the concrete. Increasing the applied axial stresses on the piers increased the nominal strengths, the ultimate strengths, and the post-elastic stiffness of the piers. However, the increase in the applied initial post-tensioning stress on the concrete resulted in a reduction in the ultimate drift angles and the drift angle at the maximum lateral load. For small axial stresses on the concrete segments, the geometric nonlinearity, i.e. the rocking mechanism was predominant, while for the case of high axial stresses the material nonlinearity was dominant leading to concrete crushing at smaller drift angles. This resulted in two features in the backbone curves (Fig. 4.7): 1) the transition between the initial and post-elastic stiffness is abrupt for small axial stresses compared to high initial stresses; and 2) the slope of the lateral resistance –drift

curves beyond the peak strength is relatively sharper for higher concrete initial axial stress resulting in small ultimate drift angles. This is attributed to the high stresses accumulated by the rigid body rocking that result in more brittle failure.

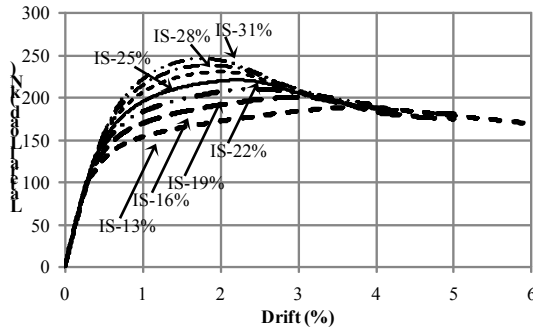


Figure 4.7: The effects of increasing the axial stresses due to post-tensioning forces on concrete segments

Fig. 4.8 shows the peak stress in the post-tensioning tendon normalized by its yield stress vs. the lateral drift of the standard piers. As shown in the figure, in no case did tendon yielding occur. In addition, the rate of increase in the post-tensioning stress was slightly higher for piers having smaller axial stress on the concrete since piers that were subjected to small axial stress due to post-tensioning were able to reach deformation higher than other piers subjected to higher post-tensioning forces (Fig. 4.7). Decreasing the applied axial stress due to post-tensioning made the rocking response and geometric nonlinearity more dominant compared to the deformation in the case of high-applied axial stress due to post-tensioning.

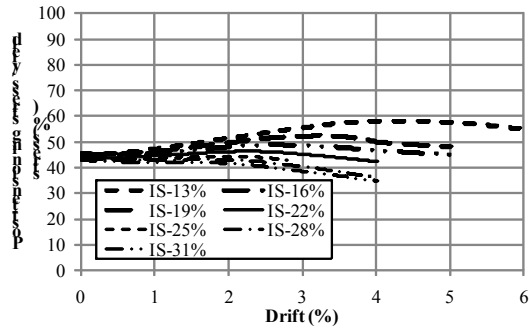


Figure 4.8: The increase in the post-tensioning stresses vs. the standard piers lateral drifts

Based on these analyses, it seems an initial concrete axial stresses of approximately $20\%f'_c$ is reasonable for design of piers similar to those examined in this chapter. The slender piers that were subjected to axial concrete stresses of approximately 20% of f'_c or less were able to reach an ultimate drift angle of 4.5% or larger.

To investigate this recommendation for a squat pier, Pier B was analyzed under different axial concrete stresses ranged from 19 to 31% f'_c . Fig. 4.9 shows the effects of the applied axial stresses on the concrete on the backbone curves of Piers B. As shown in the figure and similar to the case of the standard pier, increasing the applied axial stress due to post-tensioning slightly increased the strength of the piers; however, it significantly increased the post-elastic stiffness and decreased the ultimate drift angle. Piers that were subjected to an axial stress of approximately 22% of f'_c or less were able to reach an ultimate drift angle of 5% or greater.

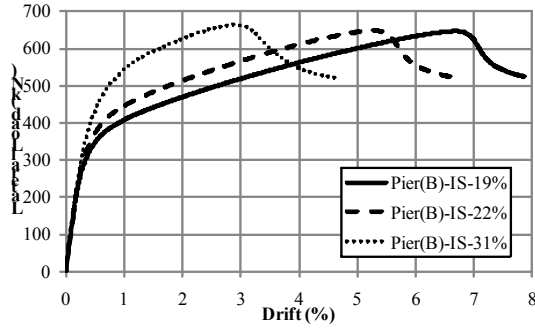


Figure 4.9: The effects of increasing the axial stresses on concrete segments for Pier B

Fig. 4.10 shows the variation of peak stresses in the tendons versus the lateral drift for Pier B for the different applied axial stresses on the concrete segments. As shown in the figure, in no case did yielding of the tendon occur.

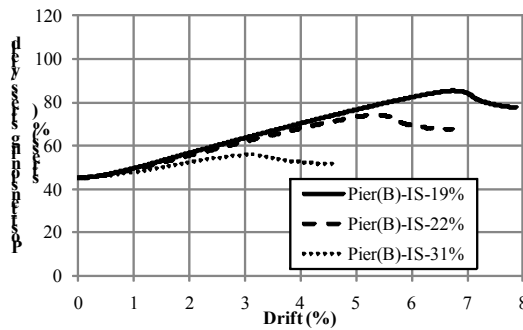


Figure 4.10: The increase in the post-tensioning stresses vs. piers type B lateral drifts

4.4.3 Effects of pier aspect ratio

The third parameter investigated in this chapter was the effects of increasing the aspect ratio – AR series – of the piers from 3 to 9 by adding one more segment from one pier to the other as shown in Fig. 4.11.

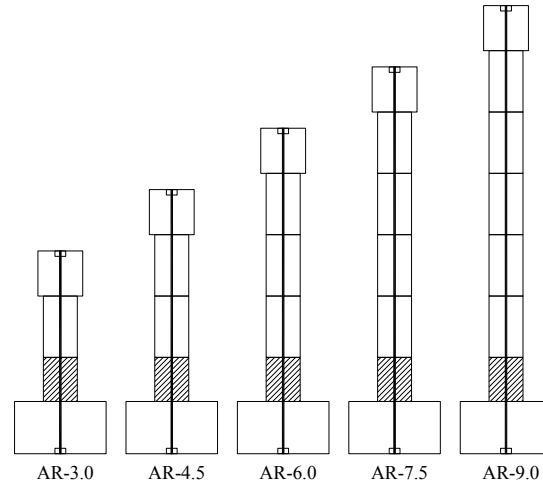


Figure 4.11: Layout of the piers having different aspect ratios

Fig. 4.12 shows the lateral resistance of the different piers versus the lateral drift angle measured at the loading point. Increasing the aspect ratio of the piers from 3 to 9 decreased the initial stiffness as well as the ultimate drift angle (Fig. 4.12(a)) and increased to lesser extent the ultimate displacement (Fig. 4.12(b)). Failure of squat piers was more abrupt compared to slender piers since in the squat piers more stress concentration and damage occurred at the bottom of the second segment compared to slender piers. The slope of the post-elastic stiffness increased with decreasing the pier aspect ratio.

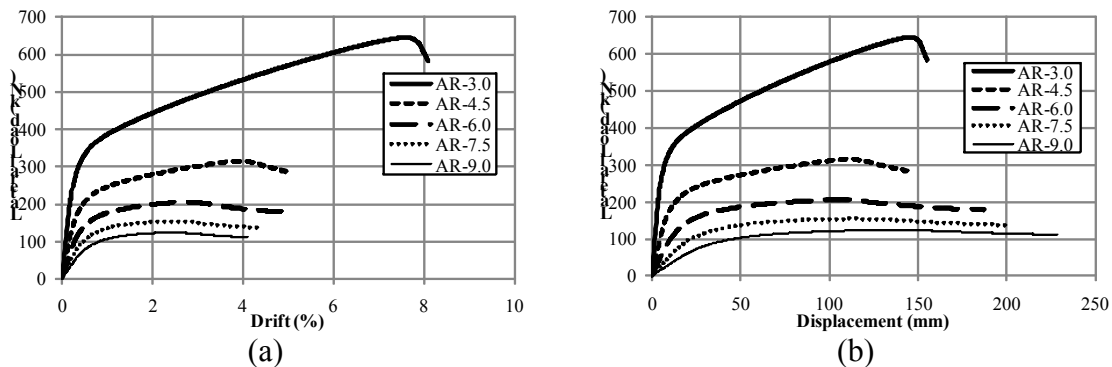


Figure 4.12: The effect of changing the piers' aspect ratio on the backbone curves

Fig. 4.13 shows an approximate mechanism for the rotation of two piers having two different aspect ratios, assuming rigid rotations of the segments over each other and also assuming that only the interface joint between the bottommost segment and foundation will open. For both piers to reach the same displacement, the rotation of the squat piers (θ_{squat}) to the rotation of the slender piers (θ_{slender}) i.e. ($\theta_{\text{squat}} / \theta_{\text{slender}}$) should be approximately equal to H/h where h , H , θ_{squat} and θ_{slender} are shown on Fig. 4.13. Because the rotation in the squat pier is higher, the elongation of the tendon in the squat pier is higher. Additionally, for the squat pier the unbonded tendon length is shorter than in the case of the slender pier, resulting in higher incremental strains and higher incremental post-tensioning stresses. Such increases led to an increase in the slope of the post-elastic stiffness. It is worth noting that in no case did the tendon reach its yield strain and in all cases the analysis stopped due to concrete crushing at the bottom of the second segment.

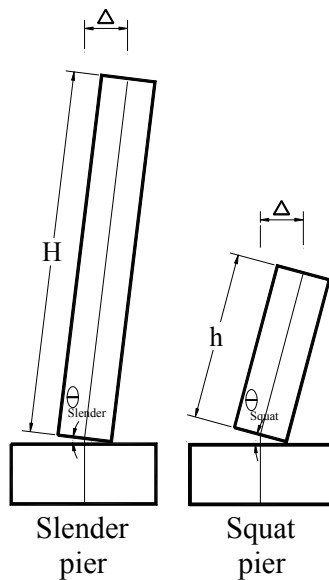


Figure 4.13: The mechanism of deformation for slender and squat piers

4.4.4 Effects of construction details

The fourth parameter investigated –CON series –was the effect of different construction details on the behavior of the pier system. As shown in Fig. 4.14, case CON-1 was a pier constructed similar to the standard pier. Pier CON-2 represents a different construction scenario where the bottommost two segments in the pier CON-1 were replaced by a single segment casted monolithically while maintaining the steel confinement height and thickness unchanged from those used for pier CON-1. In the case of pier CON-3, the three lowest segments were cast monolithically while maintaining the same steel confinement configuration. Pier CON-4 had construction details similar to pier CON-1 except that the two lower segments of pier CON-4 were both confined by steel tubes having a thickness of 6 mm [0.24 in]. In Fig. 4.14, the hatched areas represent segments confined by external steel tubes.

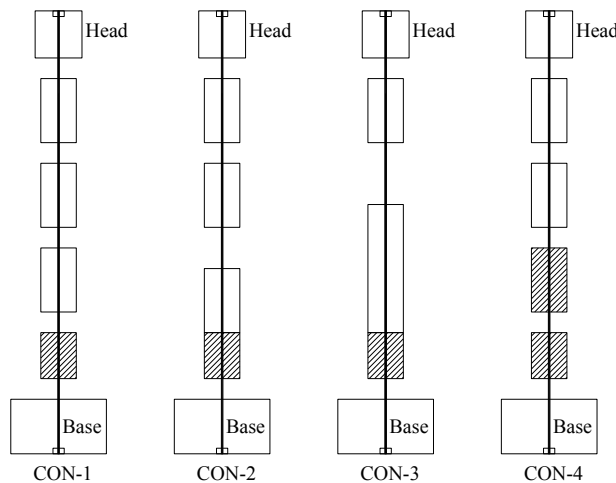


Figure 4.14: Configuration of each pier of CON series

Fig. 4.15 represents the backbone curves for the different piers of series CON. As shown in the figure, the ultimate displacement of the pier CON-2 is approximately 140% of that of the pier CON-1. In the case of pier CON-1, the pier failed due to stress concentration at the interface between the lowest two segments resulting in spalling and crushing of the concrete at the second

segment. The concrete of the second segment was less ductile than the bottommost segment due to the confining steel tube. Pier CON-2 has the advantage of the continuation of stresses between the first two segments (no interface joint opening), and consequently concentrated the stresses at the interface joint between the foundation and the bottommost segment. The high confinement of the lower segment prevented the premature failure of the pier due to high stress concentrations that happened in the case of pier CON-1.

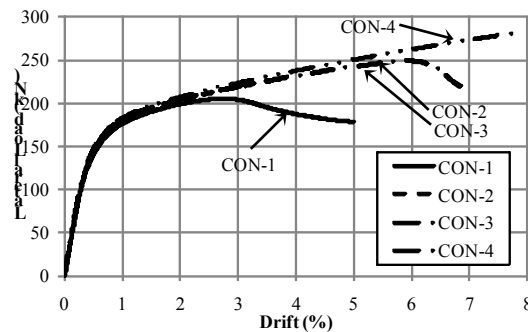


Figure 4.15: The effects of the different configurations on the backbone curves

Removing the interface joint between the second and the third segments in the case of pier CON-3 had minor effects on the ultimate drift angle. Since the joint opening at this interface in pier CON-2 was minimal, removal of the joint for CON-3 had little influence on response.

Another option to prevent premature failure due to stress concentration at the interface joint between the first and second segment was to encase the second segment in a steel tube as shown for pier CON-4 in Fig. 4.14. As expected, in the case of pier CON-4, the ultimate drift angle increased to approximately 160% and 115% of the ultimate drift angles of the piers CON-1 and CON-2, respectively. This indicated the importance of designing the confinement of each segment to obtain the optimum performance of the pier from structural and economical point of views. This analysis showed an important conclusion that a design engineer can achieve a target

displacement performance point using an appropriate segment height, appropriate confinement configuration, or a combination of the two.

4.4.5 Effects of confinement thickness

The fifth parameter investigated in this study – series CTh – was the effect of changing the confinement ratio of the bottommost segment on the backbone behavior of the system. The volumetric reinforcement ratios chosen ranged from 3.9% to 1% which corresponds to a steel tube thickness of 6.0 mm [0.24 in] to 1.5mm [0.06 in]. These thicknesses were used for confinement in two different scenarios: the first scenario (Fig. 4.16(a)) where only the bottommost segment was confined; the second scenario where the two bottommost segments (Fig. 4.16(b)) were confined. As shown in the figure, the confinement volumetric reinforcement ratio had minimal effect in the case of confining only the lower segment since failure occurred mainly at the second segment due to concrete cover spalling. On the other hand, increasing the confinement thickness of the two bottommost segments enhanced the ductility and increased the ultimate displacement by approximately 100% when the confinement thickness increased from 1.5mm [0.06 in] to 6.0mm [0.24 in]. Increasing the confinement thickness had no effect on the nominal lateral strength but increased the post yield stiffness. This shows that the confinement volumetric reinforcement ratio and height are very important parameters to fulfill the required performance level in a given seismic zone.

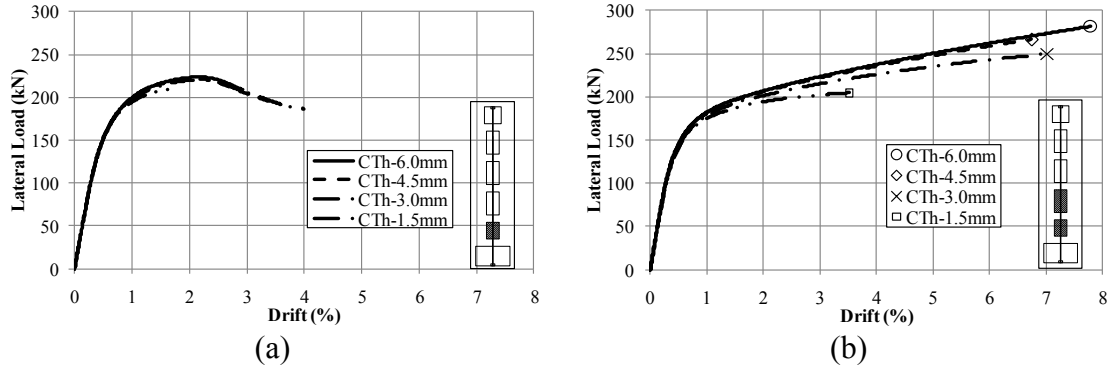


Figure 4.16: The effects on the backbone curves of the different confinement thicknesses for; a) the lower segment only, and b) the lower two segments

4.4.6 Effects of adding internal energy dissipaters

The last parameter investigated in this study was the effect of adding ten mild steel rebar as internal energy dissipaters (IED) to the interface joint between the base and the bottommost segment as well as at the interface between the bottommost segment and the second segment. During earthquake ground motion such mild steel bars would yield increasing the energy dissipation of the system.. The rebar had nominal diameter ranging from 0 (i.e. no IED) to 25 mm [#8] with all the rebar extended 305mm [12 in] on each side of the interface joints. The rebar length was selected to represent one-half the height of the bottommost segment. Fig. 4.17 shows the backbone curves for the different piers having the internal rebar.

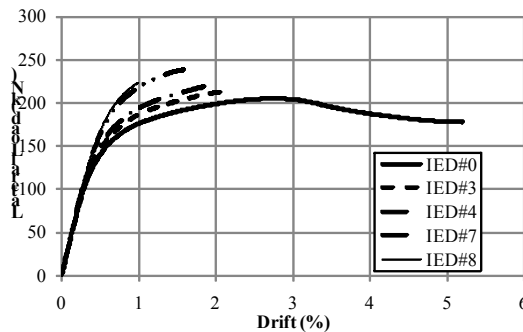


Figure 4.17: The effects of the IED on the backbone curves

As shown in the figure, adding internal mild steel rebar, as energy dissipaters, increased the ultimate strength. However, failure of the piers having such rebar was quite brittle with limited drift angle capacity. Adding the rebar changed the mode of failure from compression controlled, for pier IED#0- without internal rebar, to anchorage failure in the rebar due to the limited development length (Fig. 4.18).

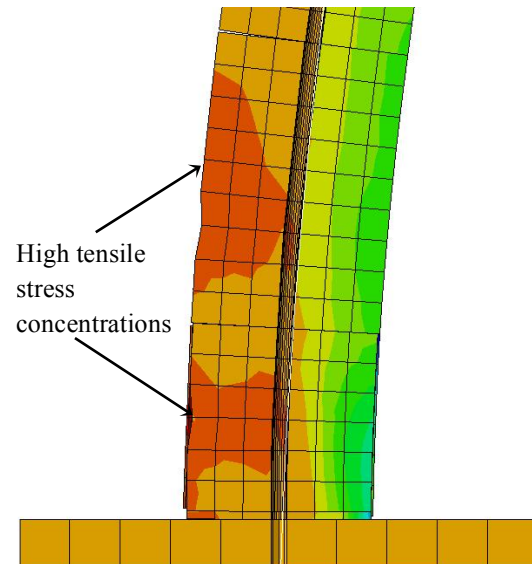


Figure 4.18: High stress concentrations in the segments due to the insufficient development length of the IED bar

In general, increasing the rebar size decreased the ultimate drift angle but increased the ultimate strength of the piers. Fig. 4.19 shows the relationship between pier lateral drift angle versus the normalized tensile stress in the rebar located at the extreme tension side of the pier. The normalized tensile stress is defined as the stress in the rebar normalized by its yield stress. The figure shows that in the case of small rebar diameters, i.e. #3 and #4, the mild bars reached their yield strength before the failure of the pier occurs. However, the rebar were not able to develop their over-strength stresses. For large rebar diameters i.e. #7 and #8 the mild rebar didn't reach their yield stress. However, there was softening in the behavior of the rebar. This softening

is attributed to anchorage failure of the rebar. Yielding of the rebar potentially will lead to higher energy dissipation, high residual displacement, and more concrete damage. However, the rebar should be well designed to avoid brittle anchorage failure.

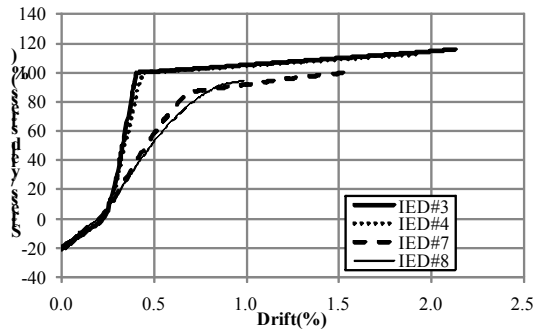


Figure 4.19: The effects of different IED rebar diameters on normalized stresses on the rebar

4.5 Findings and Conclusions

This paper discusses the seismic behavior of the SPPT bridge pier system. The piers consist of precast segments stacked on each other and sandwiched between a reinforced concrete foundation and the bridge superstructure. The system is connected by unbonded post-tensioning tendons passing through ducts made in the segments during casting. The bottommost segments of the piers were encased in steel tubes to enhance its ductility. A FE model was used to investigate different design parameters and how they affect the backbone curves of a given pier. Different parameters including: initial post-tensioning stresses as a percentage of the tendon yield stress, the applied axial stresses on concrete due to post-tensioning, the piers aspect ratios, construction details, confinement thicknesses, and adding internal mild steel rebar as energy dissipaters are discussed in this chapter. The analyses revealed that:

- Increasing the post-tensioning stresses in the tendon by decreasing its cross sectional area while keeping the same axial stress on the concrete won't have significant effects on relatively slender piers. In this case tendons will not likely yield. On the other hand,

increasing the initial post-tensioning stresses in the tendons of squat piers will potentially lead to yielding of the tendon during a major earthquake excitation which will decrease both the pier's tangent stiffness and the ultimate strength. Based on the data analyzed in this chapter, it seems that an initial tendon stress of 45% of its yield stress will be appropriate for design purposes. Using this initial post-tensioning stress will not lead to yielding of the tendon until a lateral drift angle of approximately 4.5%.

- Increasing the initial axial stresses on concrete segments by increasing the post-tensioning forces significantly increased the nominal and ultimate strengths, but reduced the ultimate drift angles. Based on the data analyzed in this chapter, an initial axial stress on the concrete of approximately 20% of f'_c seems appropriate for design purposes.
- Increasing the aspect ratio of the piers led to decrease of the initial stiffness and post-elastic stiffness as well as the nominal lateral load. On the other hand, increasing the aspect ratio led to less brittle descending branch of the backbone curves.
- Encasing the concrete segments in steel tubes significantly increased the ductility of the SPPT piers. However, the confinement volumetric ratio and height are critical parameters that can be tailored to fit different seismic demands.
- Adding internal energy dissipaters to the piers led to increase in the ultimate strength and post elastic stiffness. Using small reinforcement ratios resulted in yielding of the rebar potentially leading to high-energy dissipation and residual displacement. On the other hand, using high reinforcement ratios resulted in elastic response of the rebar potentially leading to small energy dissipation and residual displacements. However, adequate development length should be provided to avoid concrete brittle failure.

4.7 References

- ABAQUS Software and Documentation, Version 6.8-2. © Dassault Systèmes, SIMULIA, 2008.
- ASTM A569/A569M-98, (Standard Specification for Steel, Carbon (0.15 Maximum, Percent), Hot-Rolled Sheet and Strip Commercial)
- ASTM A779 / A779M – 05, (Standard Specification for Steel Strand, Seven-Wire, Uncoated, Compacted, Stress-Relieved for Prestressed Concrete)
- Chou, C.-C., and Chen, Y.-C., (2006). “Cyclic tests of post-tensioned precast CFT segmental bridge columns with unbonded strands” *J. Earthquake Engng. Struct. Dyn.*, 35, 159-175.
- Dawood, H. M., “Seismic Behavior and Design of Segmental Precast Post-tensioned Concrete Piers”, M.Sc. thesis, Washington State University, Washington, 2010
- Dawood, H., ElGawady, M., and Hewes, J., “Behavior of Segmental Precast Post-Tensioned Bridge Piers Under Lateral Loads: Experimental and Modeling”, *Journal of Bridge Engineering*, 2010 (in review).
- ElGawady, M., Booker, A., Dawood, H. M. (2010- In press). “Seismic behavior of post-tensioned concrete filled fiber tubes”, *ASCE, Journal of Composites for Construction*.
- Hewes, J.T. “Seismic Design and Performance of Precast Concrete Segmental Bridge Columns.” Ph.D. Dissertation, University of California, San Diego, La Jolla, California. 2002.
- Priestley, M.J.N., Calvi, G. M., and Kowalsky, M. J., “Displacement Based Seismic Design of Structures,” IUSS Press, Pavia, Italy, 2007, 720pp.

CHAPTER 5

FINITE ELEMENT MODEL CALIBRATION AGAINST SPPT SYSTEM DEVELOPED IN WASHINGTON STATE UNIVERSITY AND PARAMETRIC STUDY

5.1 Introduction

The aim of this chapter is to calibrate the finite element model described in chapter (3) against the experimental study conducted on a segmental precast post-tensioned (SPPT) pier system developed in WSU. The chapter contains a brief description of the experimental studies conducted by Booker A. (2008) and Sha'lan A. (2009) at WSU. The implementation of the FE model to fit the different parameters used in these studies is described and followed by a comparison between the output of the FE model and the two experimental studies. Finally, a parametric study is presented.

5.2 Piers Tested by Booker A. (2008)

Two SPPT concrete piers tested by Booker A. (2008) were used in the FE model's calibration. These piers were tested under cyclic loading induced by an actuator attached to a loading steel frame (Fig. 5.1). The two piers have the characteristics presented in Table 5.1 and shown in Fig. 5.2.

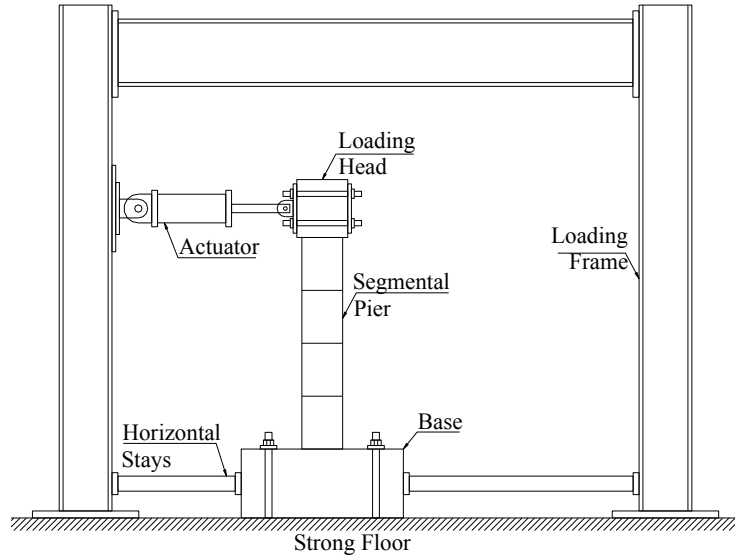


Figure 5.1 Schematic drawing showing the setup for the cyclic loading test for the piers

Table 5.1 Description of the columns used in the laboratory testing

Name	Height to Load	Horizontal Reinforcement	No. of segments	Segment Height
FRP1	1651 mm [65 in]	FRP Tube	1	1524 mm [60 in]
FRP4	1651 mm [65 in]	FRP Tube	4	381 mm [15 in]

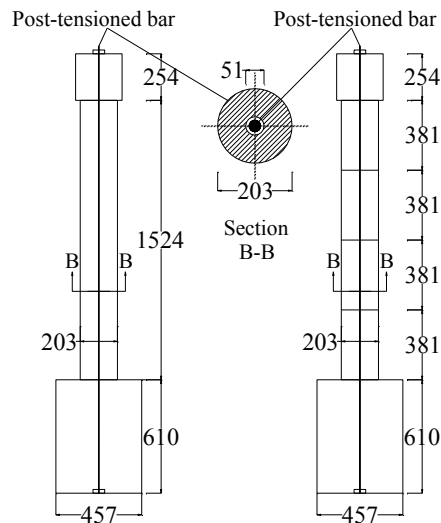


Figure 5.2 Schematic drawing for the two piers used for the calibration of the FE model (Dimensions in mm)

5.3 Bents Tested by Sha'lan (2009)

Two SPPT concrete piers tested by Sha'lan A. (2009) were used in the FE model's calibration. The schematic drawings showing the setup for the cyclic loading test and the bents configuration are shown in Figs. 5.3 and 5.4, respectively. Table 5.3 shows the description of the tested frames.

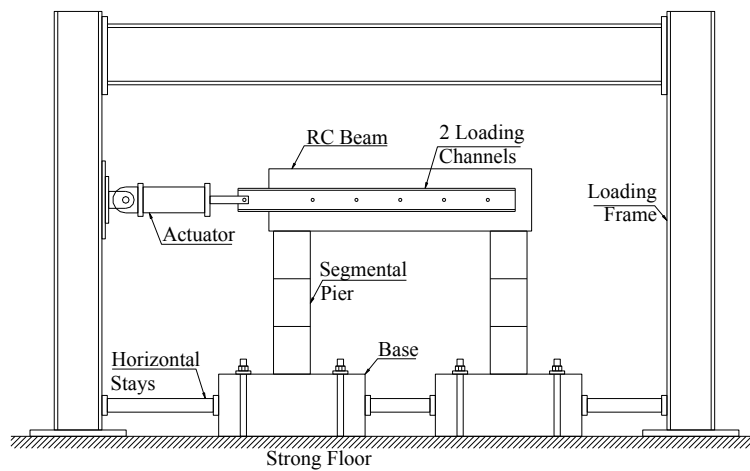


Figure 5.3 Schematic drawing showing the setup for the cyclic loading test for the bents

Table 5.2 Description of the bents used in the laboratory testing

Name	Height to Load	Horizontal Reinforcement	No. of segments	Segment Height
F-FRP1	1334 mm [52.5 in]	FRP Tube	1	1143 mm [45 in]
F-FRP3	1334 mm [52.5 in]	FRP Tube	3	381 mm [15 in]

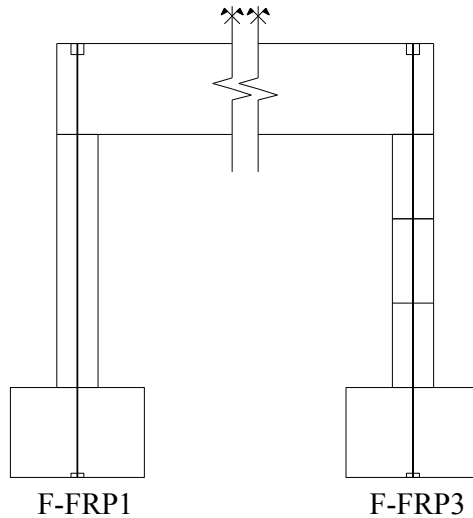


Figure 5.4 Schematic drawing for the tested frames

5.4 Finite Element Model Implementation

The specimens studied by Booker A. (2008) and Sha'lan (2009), were constructed by sandwiching segments between the foundation and superstructure of the pier (represented by a loading stub for the piers and by a reinforced concrete beam for the bents) by an unbonded post-tensioned bar. The segments were plain concrete directly poured in glass fiber reinforced polymer (GFRP) tubes to confine the concrete's core and work as permanent formwork for the segments. In the case of the bents, a reinforced concrete beam was post-tensioned to the top of both piers to make the two piers behave as one bent.

The passive confining stresses imposed by the GFRP tubes on the concrete core during loading alter its stress strain behavior by increasing both its peak strength and ductility. Through this study, Samaan et al.'s (1998) model was used for developing the stress-strain behavior of the pier's core. On the other hand, the model developed by Mander et al. (1988) was used to develop the stress strain curve of the reinforced concrete beam.

The characteristic compressive strength (f'_c) of the concrete used for casting the segments and the reinforced concrete beam was 13.8 MPa [2000 psi] and 22.08 MPa [3200 psi], respectively. Concrete was defined using a density of 2214 kg/m³ [138 lb/ft³] and a Poisson's ratio of 0.2. The stress strain curves in compression for the concrete segments and thereinforced concrete beam is shown in Figs. 5.5 and 5.6, respectively.

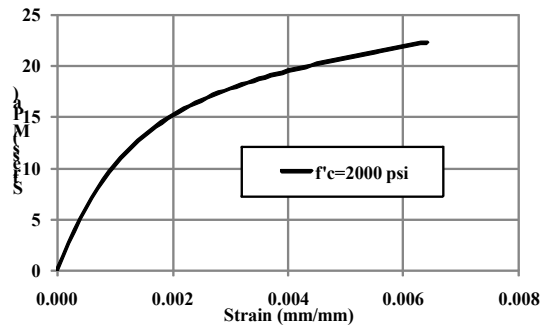


Figure 5.5: Stress strain curves for the concrete of segments

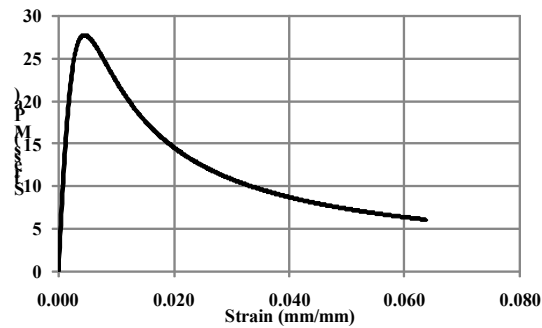


Figure 5.6: Stress strain curves for the concrete of the beam

The tendons used in these two studies were DYWIDAG hot-rolled post-tensioning bars 31.75 mm [1.25 in] in diameter. The tendon's material was modeled using a density of 7840 kg/m³ [0.28 lb/in³], Poisson's ratio of 0.3, modulus of elasticity of 204,774 MPa [29,700 ksi], yield stress of 874 MPa [126,800 psi] and ultimate stress of 1,110 MPa [160,900 psi].

The GFRP tube was supplied by Amalga Composites. Amalga Composites clear fiberglass tubing was selected with a diameter of 203 mm [8 in] and wall thickness of 3.18 mm [0.125 in]. The tubes were delivered in ten-foot lengths, which were cut to size. The GFRP material was used with an elastic modulus of 13,848 MPa [2E6 psi] and a Poisson's ratio of 0.35 (Appendix A).

5.5 Results and Discussions

5.5.1 Piers

The FE model was able to capture the overall behavior of the piers. Figs. 5.7 and 5.8 show the backbone curves from the experimental work superimposed with the model's output. It is worth mentioning that the abrupt reduction in the tangent stiffness of the system was measured in the FE model when the neutral axis at the lowermost section of the pier reaches the tendon's level, this behavior was also reported by Hewes and Priestley (2002).

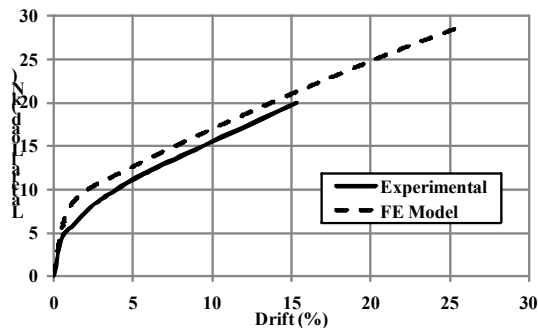


Figure 5.7: Experimental versus predicted backbone curves for the singly segmented pier

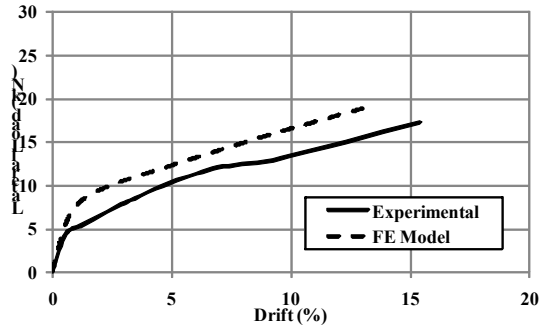


Figure 5.8: Experimental versus predicted backbone curves for the multi segmented pier

Figs. 5.7 and 5.8 shows that the FE model was able to capture the initial stiffness of the piers. On the other hand, the FE model over estimated the lateral load at which the stiffness is reduced. An indepth study was performed to understand which factor affects this load, the major factor was the post-tensioning load. The foundation surface wasn't well leveled during the casting, to overcome this problem a grout layer was used to assure a well leveled surface. This grout layer showed severe damage while testing the piers in the lab. The grout behavior can be explained as follows, at the beginning of the lateral loading the grout behaved well so it didn't affect the system's behavior. At high lateral drift angles, the softened grout layer affected the behavior by reducing the post-tensioning stress in the tendon and by behaving as a soft billow under the pier. This behavior was found to give an explanation if such a deviation between the FE model and the experimental results.

5.5.2 Bents

In the case of the bents, a cement paste layer approximately 6mm [0.25 in] thick was used to level the foundation surface. This layer was simulated in the model by an elastic material that has an elastic modulus of 4.83 MPa [700 psi] (Darwish and Al-Samhan).

Figs. 5.9 and 5.10 show the backbone curves from the experimental work conducted on the SPPT concrete bents superimposed with the model’s output. The curves shows that the FE model was able to capture quite well the backbone behavior of the system.

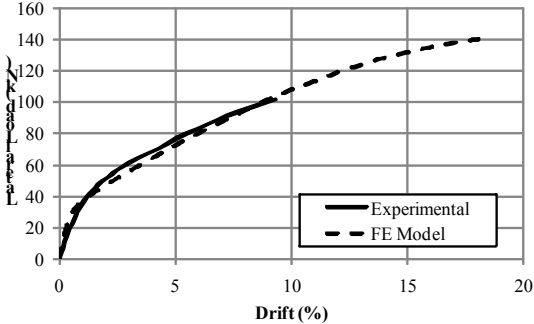


Figure 5.9: Experimental versus predicted backbone curves for the singly segmented bents

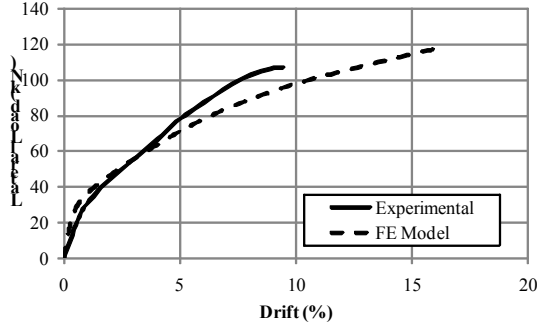


Figure 5.10: Experimental versus predicted backbone curves for the multi segmented bents

5.6 Parametric Study

The model described above was used to study the effects of different design parameters on the backbone curves of PPT-CFFT piers. The piers in this parametric study have $f'_c = 41.4$ MPa [6000 psi], a FRP confining tube thickness = 19 mm [0.75 in], the FRP characteristics were similar to those used in FRP1 and FRP4. Two series of piers were investigated in this parametric study: series “L” are piers having large diameter of 1220 mm [48 in] while series “S” are piers

having a diameter of 610 mm [24 in]. The post-tensioning tendons had nominal diameters of 176 mm [6.92 in] and 93 mm [3.68 in] for ‘‘S’’ and ‘‘L’’ series, respectively. The piers have heights ranging from 1830 mm [72 in] to 9145 mm [360 in]. All the piers were subjected to external gravity load corresponding to an axial stresses normalized by f'_c (DL) of 5%, unless otherwise mentioned. The piers were subjected to variable post-tensioning forces corresponding to axial stresses, normalized by f'_c , (PT) ranging from 10% to 30%. The increases in the applied post-tensioning forces were achieved by increasing the stresses in the tendons from 20% to 60% of the yield stresses of the tendons, respectively.

5.6.1 Effects of applied post-tensioning force

Fig. 5.11 shows the effects of changing the applied post-tensioning force on the backbone curves of three different piers of the S-series. The piers have three different aspect ratios (AR) of 3, 6, and 9. As shown in the figure, increasing PT from 10% to 30% increased the piers nominal strengths. The rate of increase in the nominal strength is higher for slender piers compared to squat piers. For a given aspect ratio, increasing the post-tensioning stresses in the tendon led to early yielding of the tendon. Yielding of the tendon is characterized by softening in the backbone curve due to degradation in the lateral strength and stiffness. Under earthquake excitation, yielding of the tendon leads to losses in the post-tensioning forces. However, for all cases presented in the figure, the earliest yielding in a tendon occurred at a drift angle of approximately 7% for pier having an AR = 3 and PT = 30%. A typical bridge pier would reach a drift angle of approximately 6% under the maximum credible earthquake.

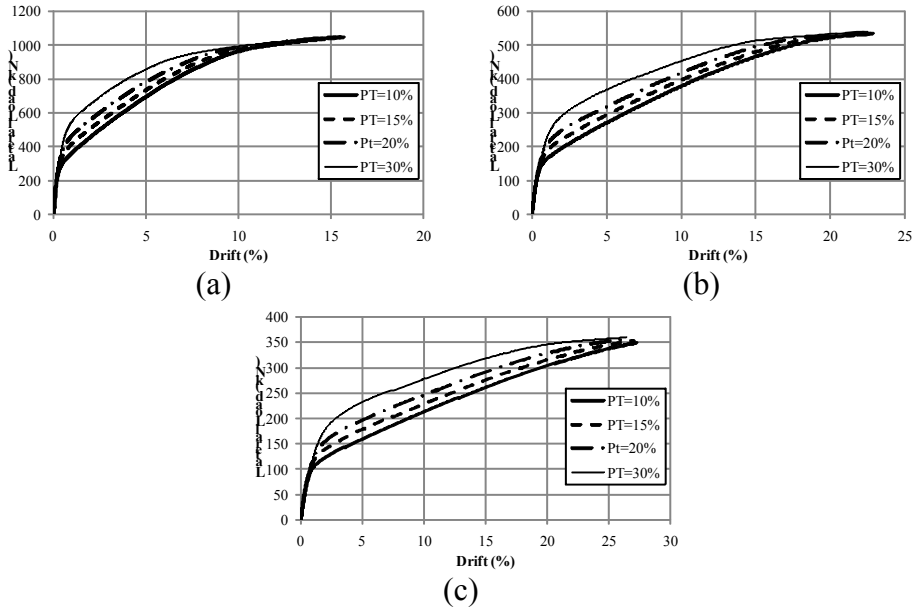


Figure 5.11: Effects of changing the applied post-tensioning forces on the backbone curves of piers having aspect ratios of (a) 3, (b) 6, and (c) 9 (Note the different scales in the graphs)

5.6.2 Load combination effects

Fig. 5.12 shows the backbone curves for three piers of S series having AR of 3, 6, and 9. The three piers have axial stresses due to the applied gravity load and post-tensioning force, normalized by f'_c , of 25%. However, two different load combinations were investigated. Case I has PT = 15% and DL=10% while case II has PT=20% and DL=5%. As shown in the figure, for drift angles smaller than approximately one-half the ultimate drift angle of each pier, the backbone curves are sensitive to the total axial stresses. However, beyond such drift angle, piers having higher PT yielded at smaller drift angles compared to those having smaller PT. Relatively early yielding of the tendon in the case of piers having higher PT led to smaller ultimate resistance. Hence, for practical application and within drift angles of 6% or smaller, it seems appropriate for a design model to consider the effect of the total axial stresses.

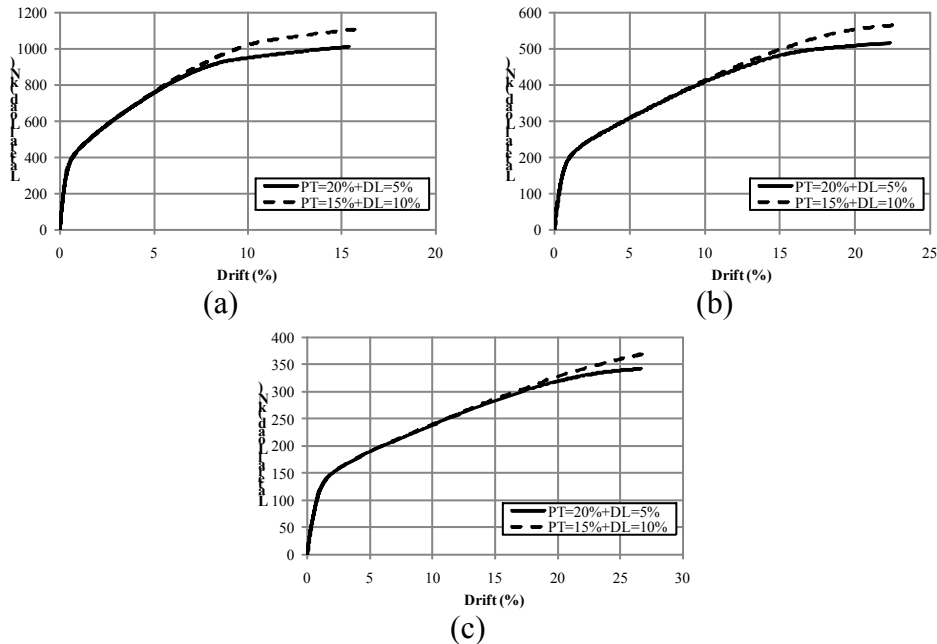


Figure 5.12: Effects of different combinations of axial stresses for piers having AR = (a) 3, (b) 6, and (c) 9 (Note the different scales in the graphs).

5.6.3 Effects of pier aspect ratio

Fig. 5.13 shows the backbone curves for four different piers of the S series having AR = 3, 6, 9, and 15. All the piers had PT = 20% and DL = 7%. As shown in the figure, decreasing the aspect ratio of a pier increased the pier initial stiffness, nominal strength, and ultimate strength. However, such increase in the ultimate strength was accompanied by a significant decrease in the pier deformation capacity. In addition, yielding of the tendons occurred at small drift angles for squat piers. Yielding of the tendon occurred at drift angles ranged from 10% for AR = 3 to 30% for AR = 15.

5.6.4 Pier size effects

Fig. 5.14 shows the backbone curves for two piers: one pier from the S series and the other one from the L series. Both piers have the same aspect ratio of 3. The piers were investigated under PT = 10% and 30%. The applied lateral load of the piers were normalized by

the cross sectional area of the pier. As shown in the figure, for the same axial stress both piers have the same shear stresses for a given AR drift angle until opening of the interface joints at the bases of the piers. However, once the interface joints opened, the shear stresses for the smaller pier are higher than those of the larger pier at a given drift angle. Finally, the smaller pier reached yielding of the tendon at smaller drift compared to the larger pier. The tendon yielded at drift angles ranged from approximately 7% for $PT = 30\%$ to 10% at $PT = 10\%$. The corresponding values for large piers are 10% and 15%, respectively.

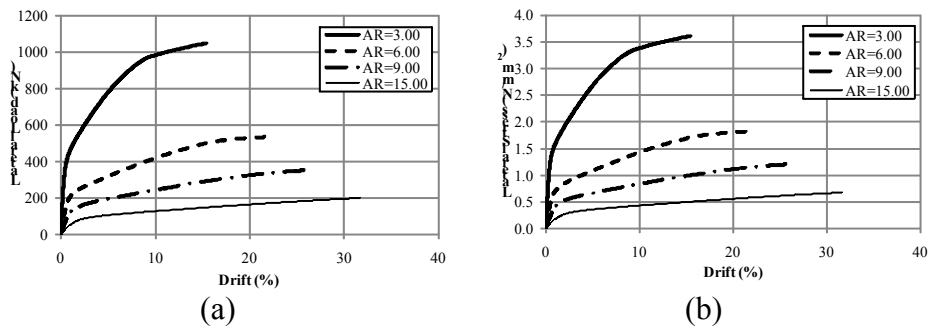


Figure 5.13: Effects of piers aspect ratios on the backbone curves of lateral drift angle vs. a) lateral load; and b) lateral load normalized by the cross sectional area

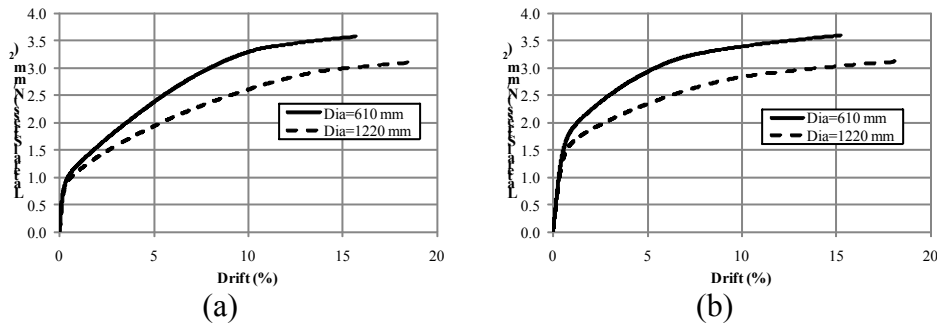
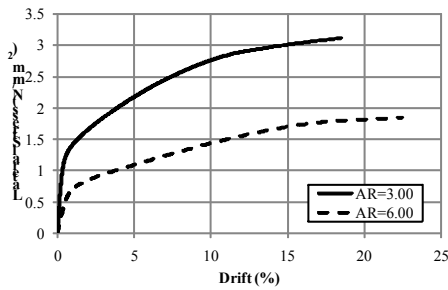


Figure 5.14: Backbone curves for two piers having $AR = 3$ and different sizes for (a) $PT = 10\%$, and (b) $PT = 30\%$

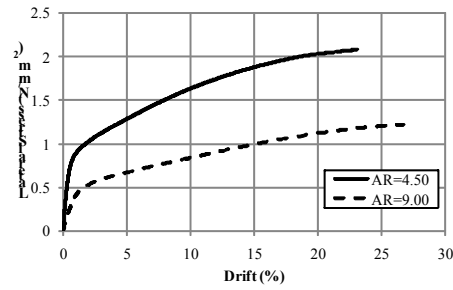
5.6.5 Diameter size effects

Fig. 5.15 shows the backbone curves for six different piers representing three different groups. Each group includes one pier of the S series and one from the L series having the same

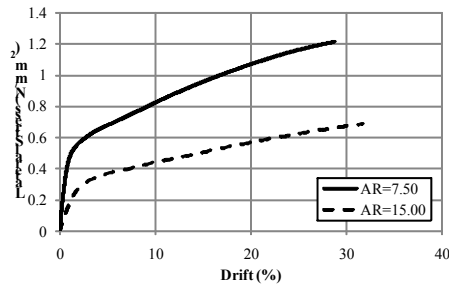
height of 3660 mm [144 in], 5490 mm [216 in], or 9150 mm [360 in]. The lateral forces were normalized by the piers cross sectional areas and presented as shear stresses. As shown in the figure, the pier diameter size has a significant effect on the shear stresses and limited effects on the lateral drift angle capacity. Piers of the L series consistently were able to resist higher stresses compared to those of the S series at the same drift angle. For the same pier height, increasing the piers diameter by 100% increased the lateral shear stresses by approximately 100%. Fig. 5.16 shows an approximate mechanism for rocking of two piers having the same height but with different cross sectional diameter. As shown in the figure, for the same drift angle, increasing the pier cross sectional diameter increases the lever arm between the compression forces in the concrete stress block and the tension forces in the tendon. In addition, moving the tendon far from the rocking pivot increases the stretch in the tendon leading to higher post-tensioning stresses and higher lateral resistance. Finally, increasing the diameter size reduced the displacement capacity of the piers. However, all the piers reached a lateral drift angles significantly higher than 6%.



(a)



(b)



(c)

Figure 5.15: Backbone curves for piers from the S series (dashed line) and L series(solid line) having heights of (a) 3660, (b) 5490, and (c) 9150 mm

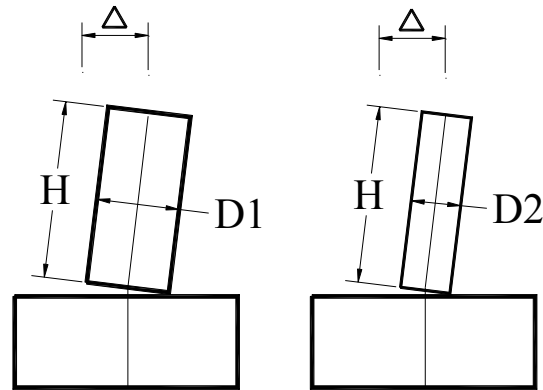


Figure 5.16: An approximate mechanism for rocking of two piers having the same height but with different cross sectional diameter

5.6.6 Confinement effects

Figs. 5.17 and 5.18 show the backbone curves for four piers: two from the S series and two from the L series. All piers have a height of 5487 mm [216 in]. The piers were subjected to PT ranged from 10% to 30%. The piers were constructed with two different FRP tubes. Both tubes have the same thickness of FRP but the second tube having a tensile stress of 275.79 MPa [40 ksi] and E modulus of 24,821 MPa [3600 ksi] representing a stronger and stiffer FRP tubes available in the market. Fig. 5.19 shows the stress-strain behavior for the S series and L series confined using the different FRP materials. As shown in Figs. 5.17 and 5.18, increasing the modulus of elasticity and tensile strength of the tubes significantly increased the strengths and the post-elastic stiffness of the piers. The increase in the strength and post-elastic stiffness is more significant in the case of the piers from the S series.

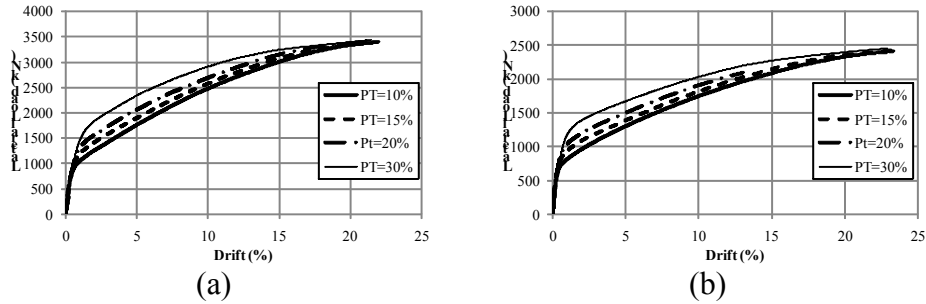


Figure 5.17: Backbone curves for piers of the L series constructed using (a) weak FRP and (b) strong FRP

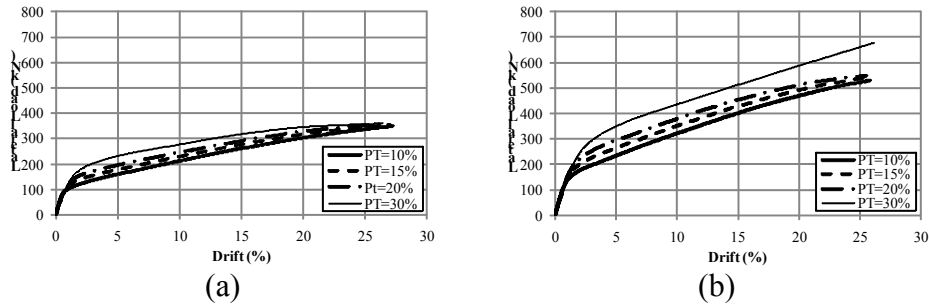


Figure 5.18: Backbone curves for piers of the S series constructed using (a) weak FRP and (b) strong FRP

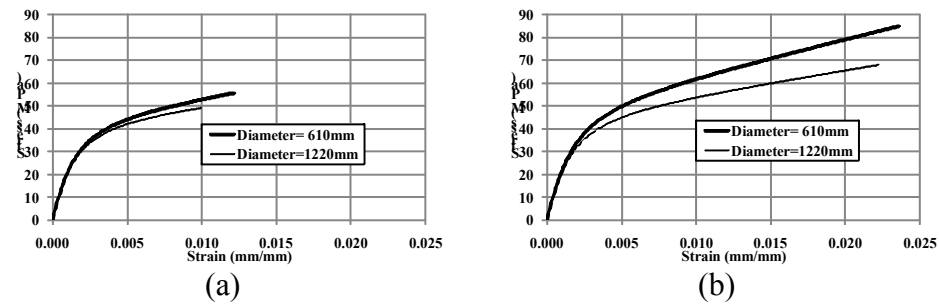


Figure 5.19: The stress-strain relationships for piers from the S and L series confined using (a) weak FRP and (b) strong FRP tubes

5.7 Conclusions

This chapter introduces the implementation of different material behaviors in the previously developed FE model to be able to capture the backbone behavior of SPPT concrete piers and bents tested in Washington State University. This investigation revealed that:

- The FE model was able to capture the backbone behavior of both SPPT concrete piers and bents quite well.
- The grout layer behaved quite well at the beginning of testing, after that the damage induced by high stress concentrations on it made it softer. This led to reduction in the post-tensioning stresses in the tendon.
- The grout layer used to level the foundation surface in the case of piers, affected the lateral load at which the tangent stiffness of the system reduces.
- The cement paste as well affected the initial and post-elastic tangent stiffness of the SPPT concrete bents.
- Taking the cement paste layer in the FE model proved its efficacy as the FE model was able to capture the bents behavior very well.

Based on the results of the presented parametric study:

- The level of the applied post-tensioning forces has significant effects on the backbone of PPT-CFFT piers. Increasing the applied post-tensioning increased the nominal of the piers. However, increasing the post-tensioning stresses in the tendons combined with decreasing the pier's height led to yielding of the tendon at relatively small drifts.
- For the parameters chosen for this study and within the feasible drift angle for a pier, the analysis was sensitive to the total applied axial loads rather than the ratio of the applied post-tensioning to gravity loads.
- Increasing the piers aspect ratios, decreased the initial stiffness, ultimate strength, nominal strength but increased the deformation capacity. In addition tendons in squat piers tend to yield at small drift angles compared to relatively slender piers.

- The analysis showed that the pier size played an important role in the behavior of the piers once the interface joint opened. However, before the interface joint opening, the performance of the piers depended on the piers aspect ratios.
- For the same pier height, increasing the pier diameter size significantly increased the pier shear stress capacity and has minimal effect on the pier deformation capacity.
- Increasing the tensile strength and E-modulus of the confining tube significantly improved the strength and post-elastic stiffness of the piers. However, it did not have significant effect on the deformation capacity of the piers.

5.8 References

- Booker, A. J. (2008). “Performance of continuous and segmented post-tensioned concrete filled fiber tubes.” M.Sc. thesis, Washington State Univ., WA, USA
- Darwish, S.M., and Al-Samhan, A., (2008). "The effect of cement stiffness and tibia tray material on the stresses developed in artificial knee." *Journal of Adhesion*, 28, 120-125.
- Hewes, J. T., and Priestley N. (2002). “Seismic design and performance of precast concrete segmental bridge columns.” Report No. SSRP-2001/25, Univ. of California at San Diego.
- Mander, J. B., Priestley, M. J. N., and Park, R. (1988). “Theoretical stress-strain model for confined concrete.” *J. Struct. Eng.*, 114(8), 1804–1826.
- Samaan, M., Mirmiran, A., and Shahawy, M. (1998). “Model of concrete confined by fiber composite.” *J. Struct. Eng.*, 124(9), 1025–1031.
- Sha’lan, A. (2009). “Performance of re-centering moment resisting frames composed of continuous and segmented precast post-tensioned concrete columns confined by FRP tubes” M.Sc. thesis, Washington State Univ., WA, USA

CHAPTER 6

**PERFORMANCE-BASES SEISMIC DESIGN OF UNBONDED SEGMENTAL
PRECAST POST-TENSIONED CONCRETE PIERS**

Segmental precast post-tensioned (SPPT) pier system has a re-centering behavior that made it an attractive system to be used in high seismic zones. The piers presented in this chapter, are singly segmented piers confined with glass fiber reinforced polymer and sandwiched between the foundation and superstructure. No reinforcement connects the pier to the super and sub structure except for unbonded post-tensioning tendons that connects the whole system together providing it with integrity and self-centering behavior.

A large set of piers with different design parameters were analyzed using a previously validated finite element model. The backbone curve of each pier had been captured, bilinearized using a standard procedure and a set of empirical equations derived to reproduce the bilinearized backbone curve. Different performance objectives had been introduced for the system according to the intensity and frequency of occurrence of a seismic event. A design procedure is introduced to design the SPPT piers using that set of empirical equations to achieve a certain performance level at a specific seismic zone.

6.3 Segmental Precast Post-tensioned (SPPT) Piers

The Kobe earthquake (Japan 1995), was the reason for demolishing over 100 reinforced concrete bridge piers due to a residual drift angles in excess of 1.5% (Lee and Billington 2010). This shows the importance of having a bridge pier's system that not only can withstand high seismic events without collapse, but also that is able to be resilient so as to maintain its

serviceability right after such events. The fact that segmental precast-post-tensioned (SPPT) piers showed high recentring capabilities, if compared against the conventional reinforced concrete (RC) piers, attracted many researchers to study its seismic behavior. In general, the SPPT system consists of precast segments stacked over each other and connected by unbonded post-tensioning tendon. Researchers have chosen different configurations for the segments (e.g. Chang et al. 2002, Hewes 2002 and Ou et al. 2007, Marriott et al. 2009, ElGawady et al. 2010(a), ElGawady et al. 2010(b), and ElGawady and Sha'lan 2010). Segments used were hollow or solid sections; reinforced with longitudinal bars and horizontal stirrups or confined with fiber-reinforced polymers or confined by steel tubes.

6.4 Summary of the Finite Element Model

ABAQUS/Standard version 6.8-2, a general-purpose finite element code, was selected as a basic platform for developing a 3D finite element (FE) model for this study. The model is presented in details by Dawood et al. (2010) and verified against two experimental studies by Hewes and Priestley (2002) and ElGawady et al. (2010).

The segmental pier system consists of precast a segment sandwiched between the foundation and the superstructure. All piers in this study are confined using glass fiber reinforced polymer (GFRP) tubes. The system is connected by unbonded post-tensioning tendons passing through ducts made in the segments during casting. The model was built up using 3D continuum elements for concrete and fiber components and 3D beam element for the tendons (Fig. 6.1).

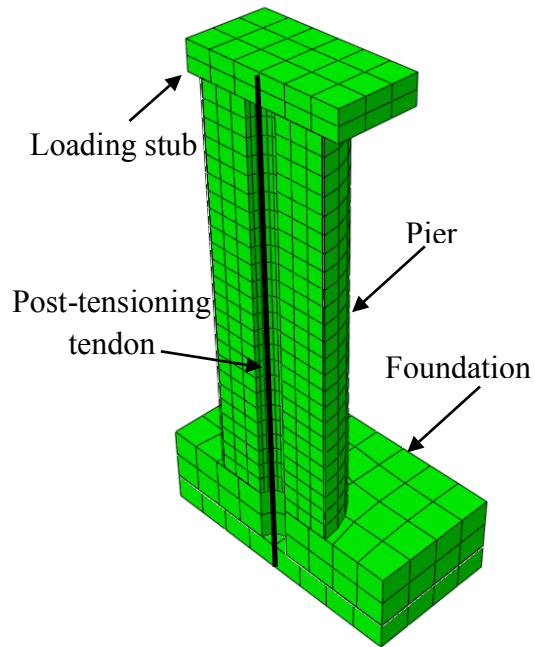


Figure 6.1: Schematic drawing of the SPPT pier showing the used mesh in the FE model and the system's different components

The concrete damaged plasticity model (Lubliner et al. 1989 and Lee and Fenves 1998) is used to model the concrete material behavior while the classic metal plasticity model is used for the tendon's material. The fiber is modeled as an elastic orthotropic material. The tendon's extremes are embedded in the loading stub (that represent the superstructure) and the foundation to simulate the tendon's anchorage, in practice, while keeping it unbonded through its remaining length. The tendon was subjected to a stress type initial condition to simulate its post-tensioning. The bottom surface of the foundation was constrained in the three motional directions assuming a strong and rough soil. The pier's loading stages were; a) tendon's post-tensioning; b) application of vertical load that represents the vertical external service load for the pier; and c) application of a monolithically increasing lateral load.

Fig. 6.2 shows the deformed shape of the pier due to the application of the lateral load, the interface opening between the foundation and the pier is obvious. Fig. 6.3 shows the stress concentration at the pier's toe. The FE model was successful in capturing the overall behavior of the system (i.e., the backbone behavior, stress concentrations at the pier's toe and failure modes). More details about the model, its implementation and validation procedures along with an in-depth parametric study refer to Dawood et al. (2010).

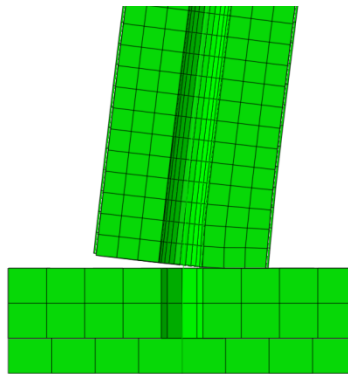


Figure 6.2: Opening of the interface between the foundation and the pier during lateral loading

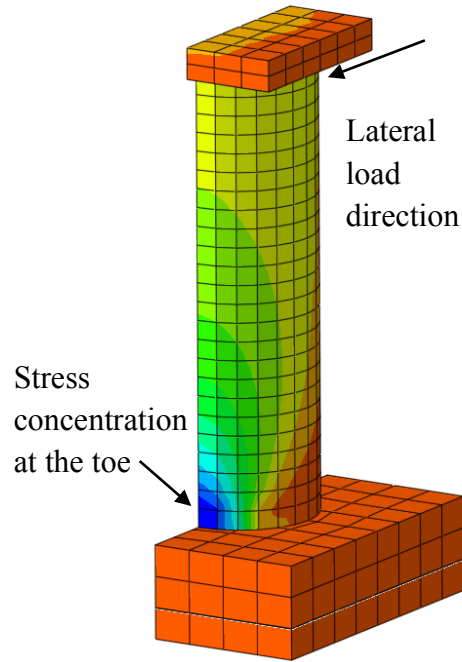


Figure 6.3: Stress concentration at the pier's toe

6.5 Study Description

The previously described FE model was used to study a large matrix of 84 piers with different design parameters (height, diameter, effective post-tensioning load, and external service load) to be able to understand the effect of each parameter on the pier's behavior. The values studied for each parameter are listed in table 6.1. The piers were built up using plain concrete with a characteristic compressive strength (f'_c) of 41.4 MPa [6000 psi] cast directly in glass fiber reinforced polymer (GFRP) confining tubes 19 mm [0.75in] thick (Table 6.2) which also worked as a permanent formwork.

Piers with aspect ratios ranging from 3 to 15 with different heights that range from 1830mm [72 in] to 9144mm [360 in] with two different diameters 1220 mm [48 in] and 610 mm

[24 in] were modeled and analyzed. The external service load (DL) ranged from 5% to 10% of the axial capacity of the pier (the external service load is mentioned to represent the own weight of the bridge as well as the traffic load). The effective post-tensioning (PT) stresses used in the study ranged from 10% to 30% of the axial pier capacity (effective post-tensioning is the post-tensioning stress after the elastic shortening of the pier occur due to the application of the external service load)

Table 6.1: Different studied parameters for the SPPT piers

Height	Diameter	PT	DL
1830 mm [72 in]	1220 mm [48 in]	10%	5%
3660 mm [144 in]	610 mm [24 in]	15%	7%
5490 mm [216 in]	-	20%	10%
9144 mm [360 in]	-	30%	-

Table 6.2: Material Properties of GFRP tubes

Flexural Modulus Longitudinal	13,790 MPa [2,000 ksi]
Flexural Modulus Circumferential	24,822 MPa [3,600 ksi]
Tensile Strength Longitudinal	634 MPa [9.2 ksi]
Tensile Strength Circumferential	2,757 MPa [40 ksi]
Compressive Strength Longitudinal	186 MPa [27 ksi]
Compressive Strength Circumferential	255 MPa [37 ksi]
Shear Modulus	5516 MPa [800 ksi]
Shear Strength	55 MPa [8 ksi]
Poisson's Ratio	0.35

Through this study, Samaan et al.'s (1998) model was used for developing the stress-strain behavior of concrete confined using GFRP. Fig. 6.4 shows the stress strain curves used for the confined concrete material in the analyses for the two chosen diameters. It is worth noting that even if the GFRP and concrete are the same in both cases, the confining effect increases as the diameter of the plain concrete core that decreases. The concrete was defined using a density of 2214 kg/m³ [0.08 lb/in³], Young's modulus of 25,414Mpa [3686 ksi] and a Poisson's ratio of 0.2.

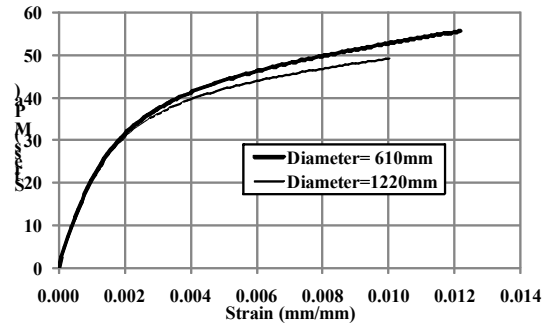


Figure 6.4: Stress strain obtained from Samaan et al. (1998) to model the GFRP confined concrete of the piers

The post-tensioning tendon used for the simulation had an equivalent nominal diameter of 176 mm [6.92 in] and 93 mm [3.68 in] which results in a reinforcement ratio of 1.5% and 1.2% for piers with diameters 1220 mm [48 in] and 610 mm [24 in], respectively. These diameters were chosen so as to subject the post-tensioning tendons to an effective stress corresponding to 20% (25%), 30% (38%), 40% (51%) and 60% (76%) of its ultimate (yield) strength, in the cases in which the effective post-tensioning stress (PT) on the piers' segments corresponded to 10%, 15%, 20% and 30% of its axial capacity, respectively. The post-tensioning tendon is defined with a Young's modulus of 204,774 MPa [29,700ksi], Poisson's ratio of 0.3, yield stress of 874 MPa [126.8 ksi] and ultimate stress of 1110 MPa [160.9 ksi].

6.6 Performance levels

The performance-based seismic design of structures necessitates specifying performance objectives for each seismic hazard level. Vision 2000 document introduced four performance levels for structures. These four levels are; 1) fully operational; 2) operational; 3) life safe; and 4) near collapse. The aforementioned four performance levels are expected for structures subjected

to frequent to very rare seismic events. The seismic levels associated with each performance level in California were presented by Structural Engineers Association of California (1999) and Priestley et al. (2007) (Table 6.3).

Table 6.3: Annual probability of exceedence of the design earthquake for each seismic performance level in California

Performance level	Design earthquake	Annual probability of exceedence for the design earthquake
Fully operational	EQ-I	87% probability in 50 years (33% of EQ-III)
Operational	EQ-II	50% probability in 50 years (50% of EQ-III)
Life safe	EQ-III	Approximately 10% probability in 50 years
Near collapse	EQ-IV	Approximately 2% probability in 50 years (150% of EQ-III)

The Federal Emergency Management Agency (FEMA) in its document (FEMA 356) specified four performance levels for buildings. The performance levels are; 1) collapse Prevention; 2) life Safety; 3) immediate occupancy; and 4) operational. The first (collapse prevention) is associated with the most severe damage, small residual stiffness and strength, and large permanent deformations. On the other hand, the fourth one (operational) is associated with very light damage, no stiffness and strength loss, and no residual deformations.

Priestley et al. (2007) introduced three performance levels for structures. These three levels are; 1) serviceability limit state; 2) damage-control limit state; and 3) survival limit state. The importance of the seismic performance levels introduced by Priestley et al. (2007) is that it included a damage-control performance level, this is economically important as through it a certain damage level is permitted under certain seismic events. The structural and economic performances are both important and influencing the objectives of the structure's behavior during severe seismic events.

Using only two performance levels to assess the unbonded post-tensioned structural elements had been adopted by Kwan and Billington (2003) and Wight et al. (2007). Kwan and Billington (2003) conducted their study on segmental precast post-tensioned bridge pier system, but in their case post-tensioning wasn't the only vertical reinforcement for the system. In that study the researchers used functional and survival performance levels to assess the piers' seismic behavior. Wight et al. (2007) also assessed the performance of unbonded masonry walls by defining performance objectives for the ultimate limit state and serviceability limit state performance levels.

The choice of performance levels and the objective behavior of the structure at each level depend mainly on the engineering judgment of the researchers in accordance to the studied system.

In this chapter serviceability and a collapse-prevention performance levels for the SPPT piers are introduced. The serviceability limit state is associated with earthquakes of higher probability of occurrence and smaller magnitudes and the objective of this performance level is to make the structure suffer minor damage. Hence, the bridge functionality and serviceability isn't compromised just after the end of the ground motion excitations. On the other hand, the collapse-prevention limit state is associated with earthquakes of lower probability of occurrence and higher magnitudes. At this limit state the bridge functionality and serviceability is compromised during the severe seismic event. After the event the bridge will require major repairs.

6.6.1 Performance objectives for the serviceability level

The serviceability limit state performance point is associated with the smallest drift angle among: a) drift angle when concrete toe reaches the theoretical ultimate strain (ϵ_n); b) drift angle at which the stress in the tendon reached 90% of the yield stress; c) drift angle corresponding to 70% of the pier's ultimate drift angle; and d) drift angle of 2%. Where, the drift angle is defined as the ratio between the measured lateral displacement at the point of load application and the height of this point of load application to the pier's foundation.

State 'a' was chosen to insure that no toe crushing would occur. It is worth noting that studies conducted by Hewes and Priestley (2002) and Dawood et al. (2010) showed that the concrete crushing strain, in the case of rocking piers, is much higher than the theoretical crushing strain that result from the currently available models for stress-strain behavior of confined concrete in compression (e.g., Mander et al. 1988, Samaan et al. 1998, Fam and Rizkalla 2001, Beque et al. 2003, and Teng et al. 2009). This shift in the ultimate strain is attributed to the high friction stresses at the toe of the piers as well as the confining material's effect on the concrete core. This shows that even if the ultimate material's strain is reached at the toe the pier can still withstand more lateral load with minor or no damage then require no or minor repairs after the seismic event is over.

State 'b' is chosen as to prevent the yield of tendons with a margin of safety. The yield of tendons will lead to losses in post-tensioning stresses, which will compromise the integrity and stability of the system as it mainly depends on the post-tensioning forces. This will also decrease the self-centering capability of the system then the residual displacement will increase at the end of seismic events.

States 'c' and 'd' were implemented to provide the piers with a sufficient margin of safety to prevent brittle or sudden failure of the system, ensure minimal or no residual drift angle, minimize the P- Δ effect on the system, and prevent excessive damage that can compromise the serviceability of the system.

6.6.2 Performance objectives for the collapse-prevention level

The collapse-prevention limit state performance point is associated with the smallest drift angle among: a) drift angle at which the post-tensioning tendons yield; b) drift angle level of 4.5%; and c) drift angle that cause a residual drift angle of 0.5%.

State 'a' was chosen because yielding of tendons will lead to losses in post-tensioning stresses, which will compromise the integrity and stability of the system, which mainly depends on the post-tensioning forces.

State 'c' was chosen to prevent failure due to P- Δ effect or excessive stress concentration and localized damage at the piers' toes.

In state 'c', a maximum allowable residual drift angle of 0.5% was chosen because of the high recentering behavior of the SPPT pier system (Hewes and Priestley 2002; Ou et al. 2007; ElGawady et al. 2010, and ElGawady and Sha'lan 2010). Such residual drift angle is potentially associated with excessive damage for the studies system.

6.7 Bilinear approximation

For backbone curves (curve relating the lateral displacement vs. the pier's strength) for all piers had been prepared and transformed into a bilinear curve. Through this study a bilinear approximations for the backbone curves introduced in FEMA 356 was considered to interpret the behavior of the system. According to FEMA 356, the first branch of this approximation has a

slope named effective stiffness (K_e) while the post-yield stiffness is taken as a percentage (α) of the effective stiffness. The ultimate lateral force (F_u) and displacement (Δ_u) is the same for the backbone curve and the idealized bilinearization. The location of the yield point (Δ_y, F_y) is computed using iterative procedure. The objective of the iterative procedure is to keep the area under the backbone and the bilinearized curves the same. The effective stiffness (k_e) is chosen so as to make the bilinearized curve intersect the backbone curve at 60% of the yield lateral load in the bilinearized curve (Fig. 6.5).

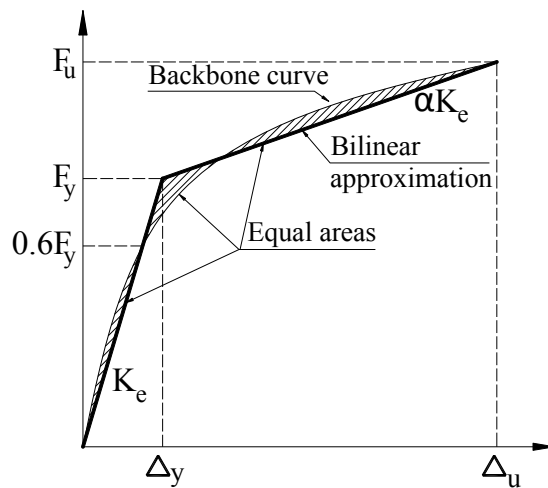


Figure 6.5: Backbone curve along with its bilinearized form

6.8 Residual Drift Angles

The study conducted by ElGawady and Sha'lan (2010) revealed that the residual displacements for the SPPT bents are equivalent to 10% of the lateral displacement reached by the specimens. On the other hand, the study conducted by Hewes and Priestley (2002) on SPPT piers showed a residual displacement of approximately 4% and 5% of the maximum lateral load

for virgin and retested piers, respectively. To maintain the conservative side, the residual displacement of the SPPT piers is assumed to be 10% of the maximum lateral displacement.

6.9 Equivalent viscous damping

The equivalent viscous damping is an essential factor that affects the behavior of the structural system under dynamic/seismic excitation. Hewes and Priestley (2002) reported an average equivalent viscous damping of 5% and minimum of 4% up to a drift angle of 3% then it increased due to spalling of concrete cover of the reinforced concrete segments. Chou and Chen (2006) reported that the equivalent viscous damping was 6.5% for SPPT piers with a minimum value that was approximately 6%. ElGawady et al. (2010) reported a minimum equivalent viscous damping of 4% for single segmented pier. For this study, a constant 5% equivalent viscous damping is assumed for all drifts as the concrete core is externally confined with the GFRP so no cover spalling will be observed before the rupture of the GFRP and collapse of the system.

6.10 Study Procedure

The target of this study is to provide a simplified procedure using empirical equations to be used for the design of the SPPT piers without running cumbersome FE analyses. To accomplish this target the following procedure was carried out; a) the backbone curves outputted from the FE model for the 84 piers using the FE model were capped by the displacements for the serviceability and collapse-prevention limit states performance points; b) the backbone curve for each pier at the two performance levels was bilinearized using the FEMA 356 bilinearization procedure, in this case the performance displacement for serviceability and collapse-prevention were used as the ultimate displacements in the FEMA procedure; c) each parameter in the bilinear backbone curve (i.e. K_e , Δ_y , F_y , Δ_u , F_u and α) is studied individually and an empirical

equation able to predict its value is derived using regression analyses; d) an empirical equation for predicting the rate of increase of post-tensioning stresses in the tendon is derived; e) a simplified systematic procedure is then derived to be able to design the SPPT pier system using these empirical equation without going through cumbersome FE analyses; and finally, f) numerical examples using this procedure are introduced along with a FE analysis for each case to verify the effectiveness and limitations of the proposed design procedure.

6.11 Collapse-prevention Limit State

6.11.1 Effective stiffness (K_{CP-e})

Eq. 5.1 should be used for simple cantilevers, where E : is the modulus of elasticity of the pier's concrete (kN/mm^2); I : is the moment of inertia of the pier's cross section (mm^4); and H is the height of the pier (mm). This equation is valid only to get the tangent stiffness for piers with ideal fixation at the bottom and ideal free joint at its top. In the case of SPPT piers, the lack of a monolithic connection between the bottom of the pier and the foundation, the presence of the post-tensioning bar that gives the system its integrity, and the fact that the effective stiffness is a secant stiffness and not the first tangent stiffness, makes it obvious that a new factor should be added to Eq. 5.1 to compensate for these three factors. This new factor was computed using nonlinear regression analysis for the values of the effective stiffness (k_{CP-e}) computed using the FEMA 356 procedure for the 84 piers studied in this chapter and added to Eq. 5.1 to get Eq. 5.2, where PT is the stress induced by the post-tensioning on the pier's concrete normalized by its characteristics compressive strength (f'_c) as a percentage and all other input must be in (kN) and (mm).

$$K_e = \frac{3EI}{H^3} \quad (\text{Equation 5.1})$$

$$K_{CP-e} \text{ (kN/mm)} = \frac{1.87}{PT^{0.3}} \frac{3EI}{H^3} \quad \text{(Equation 5.2)}$$

The error in computing the effective stiffness of the system for the 84 piers using Eq. 5.2 has a mean (μ) of approximately +4% and a standard deviation (σ) of 10.8%. The error in predicting the effective stiffness is defined by Eq. 5.3.

$$\text{Error in calculating parameter A (\%)} = \frac{A_{\text{from the imperial equation}} - A_{\text{from the bilinear approximation}}}{A_{\text{from the bilinear approximation}}} \%$$

(Equation 5.3)

6.11.2 Yield load (F_{CP-y})

In this chapter the yield load (F_{CP-y}) is taken as the lateral load at which the stiffness of the pier reduces abruptly by a factor α (Fig. 6.5). Fig. 6.6 shows the relationship between the load combination acting on the pier vs. the yield load of the pier (kN). The load combination is defined as two percentages separated by a dash; the first (left) is the stress on the concrete induced by the post-tensioning; and the second (right) is the stress on the concrete induced by the vertical axial load representing the service load, both are normalized by the concrete's f'_c as a percentage. In the figure, piers with the same dimensions are assigned a specific marker type and a code for each dimension is shown under the figure (e.g., H5490-D0610 is a pier with a height of 5490 mm and a diameter of 610 mm).

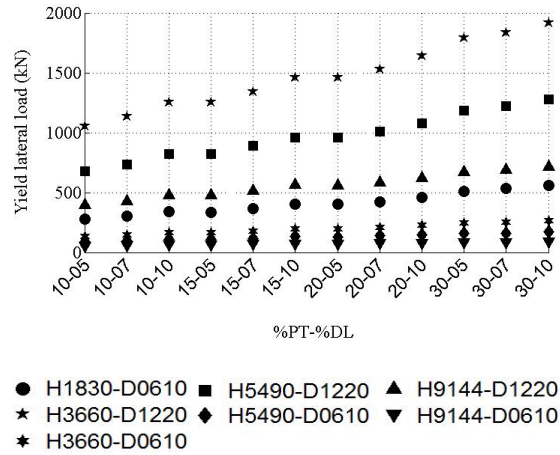


Figure 6.6: The collapse-prevention yield load associated with each specific pier

Fig. 6.6 shows that F_{CP-y} is directly proportional to the value of the combination of loads acting on the pier. For piers with the same diameter, it looks obvious that increasing the height decreases F_{CP-y} . On the other hand, for piers with the same height, increasing the diameter increases F_{CP-y} . On the light of these observations from Fig. 6.6, a nonlinear regression analysis is used to get an equation that represent the F_{CP-y} in terms of the pier's dimensions and load combinations (Eq. 5.4), where DL is the stress induced by the external service load as a percentage of the concrete's f'_c (%).

$$F_{CP-y} \text{ (kN)} = \frac{D^{2.8} PT^{0.4} DL^{0.2}}{400 H} \quad \text{(Equation 5.4)}$$

The error associated with using Eq. 5.4 to get F_y for each pier is computed by Eq. 5.3. The μ of the error computed for all piers is +1.6% with σ of 6.0%.

6.11.3 Yield displacement (Δ_{CP-y})

In this chapter the yield displacement (Δ_{CP-y}) is taken as the lateral displacement measured at the point of load application at which the stiffness of the pier reduces abruptly by a factor α (Fig. 6.5). This displacement was found to be the one at which the neutral axis at the interface surface between the foundation and the pier reached the center of gravity of the pier's cross-section (Hewes and Priestley 2002 and ElGawady et al. 2010). Δ_y in this chapter is calculated using Eq. 5.5. The μ of the error computed for each pier is -0.85% with σ of 15%.

$$\Delta_{CP-y} \text{ (mm)} = \frac{F_y}{K_e} \quad \text{(Equation 5.5)}$$

6.11.4 Performance displacement (Δ_{CP-P})

The collapse-prevention performance displacement (Δ_{cp-p}) is lateral displacement that fulfills all the target collapse-prevention performance objectives. The prevailing performance level in all the 84 piers introduced in this chapter was the 4.5% of lateral drift angle. As a result, the collapse-prevention performance point can be computed using Eq. 5.6.

$$\Delta_{cp-p} \text{ (mm)} = 0.045 \times H \quad \text{(Equation 5.6)}$$

6.11.5 Performance load (F_{CP-P})

The collapse-prevention performance load (F_{cp-p}) is the load corresponding to the performance displacement for a certain pier. Fig. 6.7 shows the performance lateral load for each pier. The figure shows that the performance load, like the yield load, increased by increasing the load combination imposed to the pier as well as increasing the pier's diameter. Also, it is inversely proportional to the pier's height. From the nonlinear regression analysis, Eq. 5.7 was derived.

$$F_{cp-p} \text{ (kN)} = \frac{D^{3.0} P_T^{0.2} D_L^{0.1}}{40 H^{1.3}}$$

(Equation 5.7)

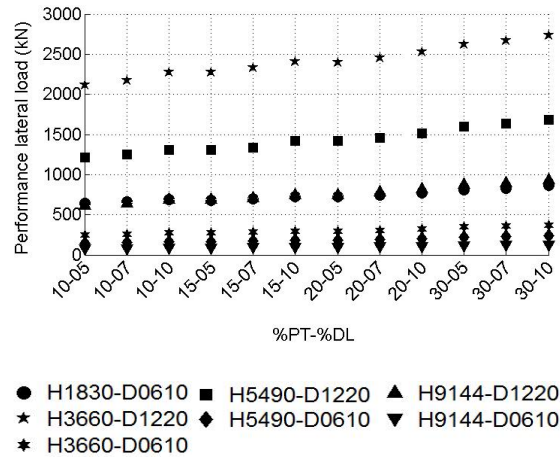


Figure 6.7: The collapse-prevention performance load associated with each specific pier

The error in using Eq. 5.7 to calculate the performance lateral load is computed using Eq. 5.3 and it has a μ value of -7.5% and σ of 5% for the 84 piers.

6.11.6 Error in predicting the lateral strength (collapse-prevention)

Until this point a single empirical equation had been developed for each parameter in the bilinear backbone curve. The previously derived equations (Eqs. 5.2, 5.4, 5.5, 5.6, and 5.7) are enough to build up an empirical backbone curve. To assess the overall accuracy of this empirical approach, the error in computing the lateral capacity of the piers (Eq. 5.3) at each lateral drift angle is calculated and plotted in Fig. 6.8. The figure shows the error calculated for the 84 piers (thin gray lines) superimposed with the line representing the mean error (continuous black line) and the lines representing the mean error plus or minus the standard deviation ($\mu \pm \sigma$) (dotted black lines).

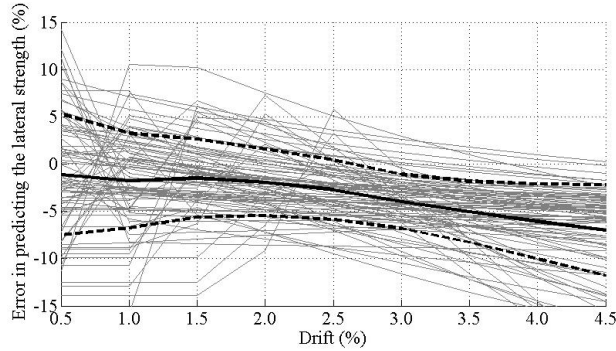


Figure 6.8: The lateral drift angle vs. the error in predicting the pier's strength (collapse-prevention limit state)

The maximum and minimum errors calculated are +15% and -20%, respectively. The figure shows that, the mean (μ) error in predicting the lateral strength for all the studied piers ranged from -1.1% to -7.0% for all drift angles up to 4.5%. The standard deviation (σ) ranged from 2.8% to 6.4%. This resulted a ($\mu \pm \sigma$) that ranges from -11.8% to +5.3% and a ($\mu \pm 2\sigma$) that ranges from -16.6% to +11.7%. Assuming that the piers represents a normally distributed community, then 68% of the piers will have an error range in predicting its strength of -11.8% to +5.3% , and 95% of the piers will have an error range of -16.6% to +11.7%.

6.12 Serviceability Limit State

The same procedure introduce for getting empirical equations to capture the bilinearized curve for the collapse-prevention limit state is also used for the serviceability limit state. As stated before, the backbone curve of the pier was capped at a drift angle that fulfills all the design objectives of the serviceability limit state. Hence, it can be deduced that the empirical equations used to predict the performance lateral load and lateral displacement will be different from the ones derived for the collapse-prevention limit state. The bilinearized backbone curve, is derived

assuming equal areas beneath it and the backbone curve from the FE analysis. This caused a slight alternation in the empirical equations derived for the effective stiffness, yield displacement and yield load in the case of collapse-prevention limit state. Even if this slight change seems unrealistic, it should be taken into consideration to make sure that the bilinearized curve best represents the behavior of the pier up to a certain lateral drift angle which is computed from the serviceability or collapse-prevention limit states.

6.12.1 Effective stiffness (K_{Ser-e})

Eq. 5.8 was found to be able to predict the effective stiffness (K_{Ser-e}) of the piers when bilinearizing its backbone curve for the serviceability limit state. The error associated with using Eq.5.8 to predict the effective stiffness of the system in the serviceability limit state has μ of -2.3% and σ of 10.2%.

$$K_{Ser-e} \text{ (kN/mm)} = \frac{1.82}{PT^{0.3}} \frac{3EI}{H^3} \quad \text{(Equation 5.8)}$$

6.12.2 Yield load (F_{Ser-y})

Eq. 5.9 best represents the yield lateral load at serviceability limit state (F_{Ser-y}) (Fig. 6.9). The error in predicting F_{Ser-y} using Eq. 5.9 for all piers has μ of +9.6% and σ of 14.9%.

$$F_{Ser-y} \text{ (kN)} = \frac{D^{2.8} PT^{0.4} DL^{0.2}}{435 H} \quad \text{(Equation 5.9)}$$

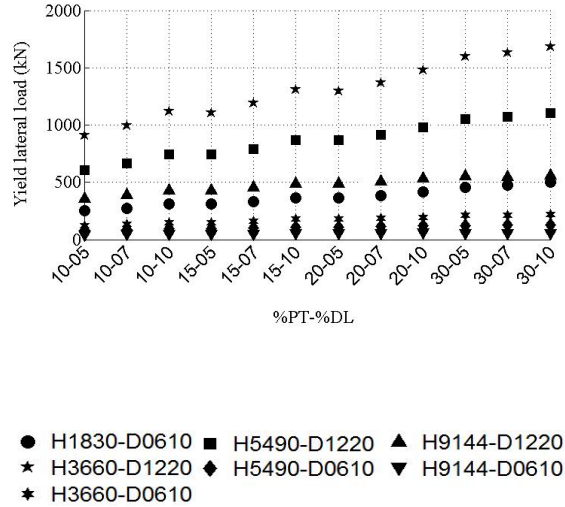


Figure 6.9: The serviceability yield load associated with each specific pier

6.12.3 Yield displacement (Δ_{Ser-y})

Eq. 5.5 was used for the calculation of the yield displacement in the case of serviceability limit state (Δ_{Ser-y}). The error in calculating Δ_{Ser-y} using this procedure has μ of +14.5% and σ of 26.5%.

6.12.4 Performance displacement (Δ_{Ser-P})

The performance displacement in the case of serviceability limit state (Δ_{Ser-P}) is calculated using Eq. 5.10. The error in calculating Δ_{Ser-P} using Eq. 5.10 has μ of +1.4% and σ of 6.7%.

$$\Delta_{Ser-p} \text{ (mm)} = 0.02 \times H \quad \text{(Equation 5.10)}$$

6.12.5 Performance load (F_{Ser-P})

Fig. 6.10 shows the value of the performance load in the serviceability limit state (F_{Ser-P}) for all piers and how it is affected by the pier's dimensions and load combinations. To be able to

predict F_{Ser-P} , Eq. 5.11 is proposed. The error associated with using Eq. 5.11 in calculating F_{Ser-P} had μ of +3% and σ of 6.4%.

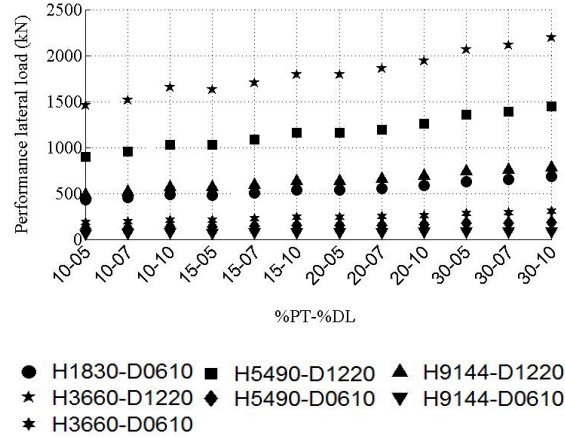


Figure 6.10: The serviceability performance load associated with each specific pier

$$F_{Ser-p} \text{ (kN)} = \frac{3 D^{3.0} P T^{0.3} D L^{0.1}}{1000 H^{1.1}} \quad \text{(Equation 5.11)}$$

6.12.6 Error in predicting the lateral strength (serviceability)

Eqs. 5.8 to 5.11 were used to get the predicted bilinearized backbone curve and Eq. 5.3 was used to calculate the error in predicting the lateral strength for all piers at different drift angles. Fig. 6.11 shows the error in predicting the lateral strength of all piers (gray lines), along with three curves representing the μ (continuous black line) and $\mu \pm \sigma$ (dotted black lines) of all curves at different drift angles. The error in predicting the lateral strength for all piers at all drifts ranged from -23% to +19% with μ ranging from -4.1% to 1.8% and σ ranging from 9.9% to 6%. This resulted in 68% of the piers have an error range ($\mu \pm \sigma$) from -12.5% to 7.8% and 95% of the piers have an error range ($\mu \pm 2\sigma$) from -22.3% to 17.1% when using the imperial procedure to calculate its lateral strength.

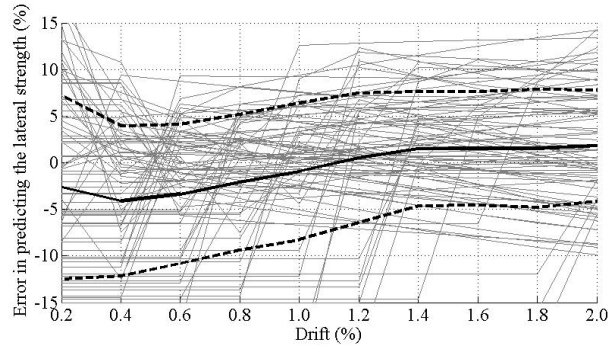


Figure 6.11: The lateral drift angle vs. the error in predicting the pier's strength (serviceability limit state)

6.13 Increase of Post-tensioning with lateral drift angle

Finding an empirical equation that correlates the lateral displacement vs. the increase in post-tensioning stress in the tendons for the SPPT piers is essential for designing the tendon's cross sectional area for each pier during the design procedure.

To accomplish this target, the curves representing the lateral drift angle versus the stress in the post-tensioning tendons normalized by its initial stress is presented in Figs. 6.12 and 6.13. The topmost curve represents a loading combination of (10% from PT and 5% from DL) and the curves below it represent (10%PT-7%DL, 10%PT-10%DL, 15%PT-5%DL, etc.tc). The figures show that the relationship between the drift angle (%) and the post-tensioning force follows two different behaviors.

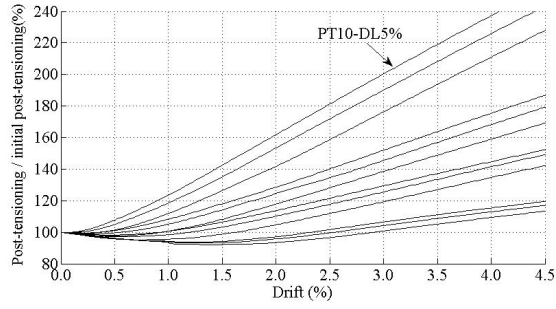
The first behavior is associated with piers subjected to high vertical load combinations. At small lateral load values, there are obvious losses in the post-tensioning stresses. At a certain stage, this behavior turns into an increase in the post-tensioning stresses again. The losses in post-tensioning stresses are attributed to high stress concentration at the pier's toe that results in high compressive strains and shortening in the pier's height. Once the neutral axis of the

bottommost surface of the pier reached the tendon's location, the tendon's starts to stretch again and the post-tensioning stresses increase approximately linearly with the lateral drift angle.

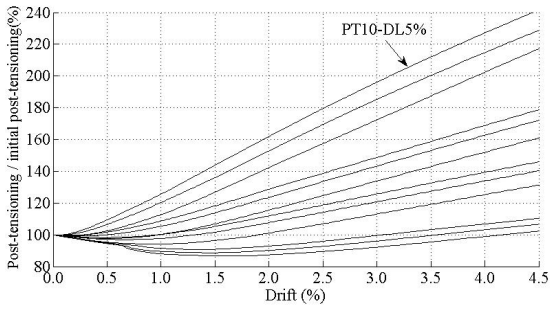
In the study conducted by Wight et al. (2007) on unbonded post-tensioned masonry walls, the authors used Eq. 5.12 to calculate the strain increase in the post-tensioning tendons, where Δ_T is lateral displacement of the wall of the point of load application; h_e is the height of the wall above the foundation surface; Δ_i is the change in the tendon's length; d_i is distance from the extreme compression fiber of the wall to the tendon's position; and c is the compression zone height at the lowermost cross section of the wall.

$$\frac{\Delta_T}{h_e} = \frac{\Delta_i}{d_i - c} \quad (\text{From Wight et al. 2007}) \quad (\text{Equation 5.12})$$

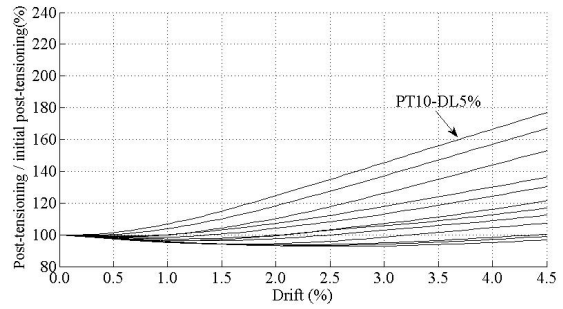
Fig. 6.14-(a) shows a schematic drawing of the deformed shape of a SPPT pier when the neutral axis didn't reach the level of post-tensioning tendon. In that case the compression zone height (c) is larger than the tendon's depth (d_i), then from Eq. 5.12 it can be deduced that at low values of lateral loading the change in the tendon's length is negative which means losses in the post-tensioning stresses. On the other hand, Fig. 6.14-(b) shows the pier after the neutral axis passed the level of the post-tensioning tendon. In that case the compression zone height (c) is smaller than the tendon's depth (d_i) and then the tendon starts to be stretched again so the stress in the tendon's increases again.



(a)

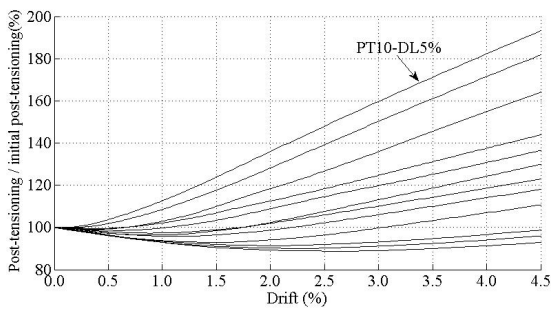


(b)

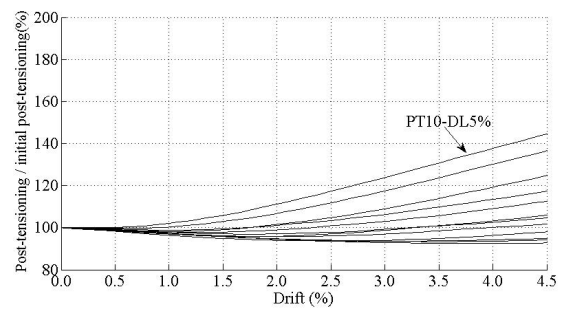


(c)

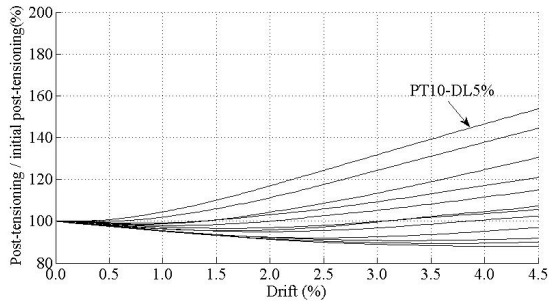
Figure 6.12: The relationship between the lateral drift angle (%) vs. the stress in the post-tensioning tendon's normalized by its initial stress for piers; a) H1830-D0610; b) H3660-D1220; c) H3660-D0610



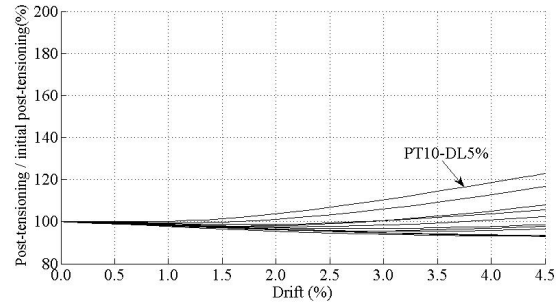
(a)



(b)

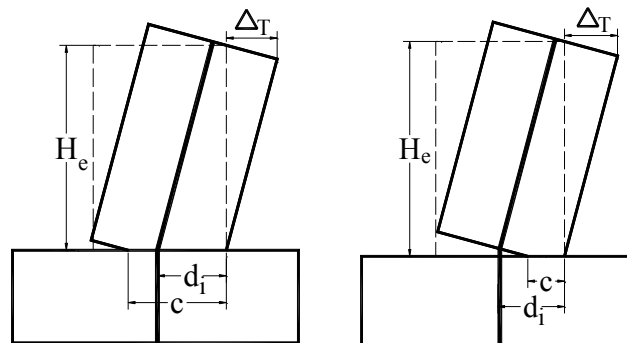


(c)



(d)

Figure 6.13: The relationship between the lateral drift angle (%) vs. the stress in the post-tensioning tendon's normalized by its initial stress for piers; a)H5490-D1220; b)H5490-D0610; c)H9144-D1220; and d)H9144-D0610



(a)

(b)

Figure 5.14: Schematic drawing of the pier; a) neutral axis didn't reach the tendon's level; and b) the neutral axis passed the tendon's level

The second behavior is associated with piers with relatively small vertical load combinations. In this case, the pier's segment behaves more as a rigid block and in that case material nonlinearity isn't prevailing from the beginning of the loading process, so the losses in the post-tensioning stresses had a negligible value and the stress starts to increase almost soon. In that case, the increase is almost linear except the first part before the interface joint between the

pier and the foundation opens. It is worth noting that the same behavior was observed in the study carried out by Yamashita and Sanders (2009).

Comparing the different graphs presented in Figs. 6.12 and 6.13, it is obvious that the rate of stress increase is directly proportional to the stress induced by the post-tensioning on the concrete. On the other hand, the stress induced on the concrete by the bridge service load doesn't seem to affect that slope. For piers with the same height, the smaller diameters have much milder slope and for the piers with the same diameter, increasing the height decreases the slope. Upon these observations, a nonlinear regression analysis is carried out and resulted in Eq. 5.13 that represents the slope of the post-tensioning increase curve as a function of the pier's dimension and stress induced by post-tensioning.

$$(S)_{\text{Slope of post-tensioning increase (kN/mm)}} = \frac{10^4 D^{0.78}}{PT^{1.4} H^2} \times P_i \quad (\text{Equation 5.13})$$

Because the increase in the post-tensioning stress doesn't start once the lateral loading starts, a horizontal plateau was assumed at the beginning of the lateral loading. As discussed before and as shown in Figs. 6.12 and 6.13 the lateral displacement at which this plateau occurs is directly proportional to the value of the loading combination imposed on the pier. The horizontal plateau is also directly proportional to the pier's height and inversely proportional to its diameter. Eq. 5.14 was found to be the best representative of the displacement at which this horizontal plateau ends according a nonlinear regression analysis of the available data.

$$(DS)_{\text{Displacement at which the post-tensioning starts to increase (mm)}} = \frac{H^{1.9} PT^{1.7} DL^{0.6}}{10^5 D^{0.9}} \quad (\text{Equation 5.14})$$

Equations 13 and 14 are sufficient to be able to draw a curve that tracks the stress change in the post-tensioning tendons. This curve starts with a horizontal plateau at a post-tensioning

percentage of 100% of its initial value, which ends at a displacement computed from Eq. 14. From that point the relationship turns into another line with a slope value calculated using Eq. 5.13 up to the performance lateral displacement.

To be able to assess the accuracy of the previously introduced procedure, the error (Eq. 5.3) in predicting the post-tensioning value in the tendon is calculated and plotted vs. the lateral drift angle for the 84 piers (Fig. 6.15). In Fig. 6.15 the error of all piers is represented by the gray lined while the mean error is represented by the black continuous line and the dotted black lines represent the $\mu \pm \sigma$.

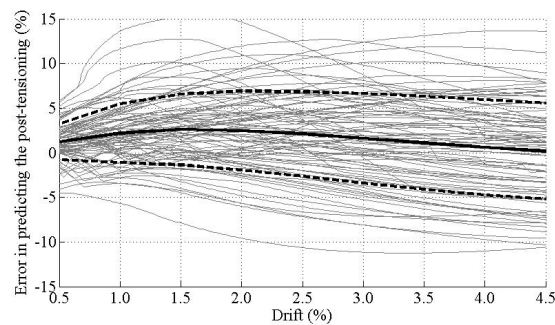


Figure 6.15: Error in predicting the change of post-tensioning stress with lateral drift angle

The error in predicting the post-tensioning value ranged from -12% to +16%. The figure shows that, the mean (μ) error in predicting the post-tensioning stress in the tendons for all the studied piers ranged from +0.18% to +2.59% for all drift angles up to 4.5%. The standard deviation (σ) ranged from 2.00% to 5.37%. This resulted a ($\mu \pm \sigma$) that ranges from -5.19% to +6.89% and a ($\mu \pm 2\sigma$) that ranges from -10.55% to 11.64%. Assuming that the piers represents a normally distributed community, then 68% of the piers will have an error range in predicting its

strength of -5.19% to +6.89% , and 95% of the piers will have an error range of -10.55% to 11.64%.

6.14 Design Procedure

Fig. 6.16 shows a flow chart diagram of the proposed design procedure for the SPPT piers. The procedure can be summarized in the following steps;

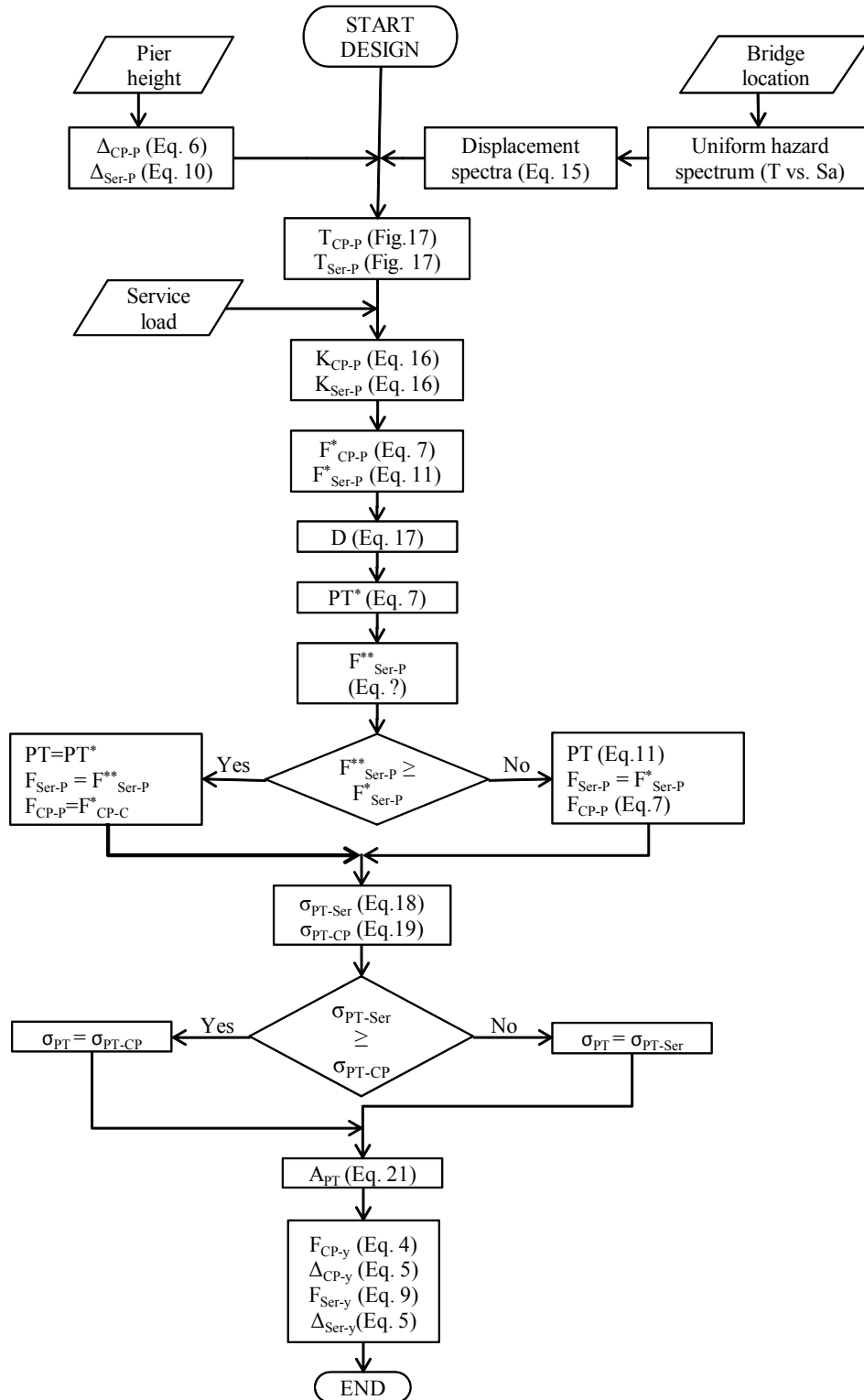


Figure 6.16: Flow chart diagram of the proposed design procedure for SPPT piers

* means that this is a temporary value that will be checked later on

1) two uniform hazard spectra (period vs. spectral acceleration) are obtained for the region in which the bridge will be constructed in, the uniform hazard spectrum of a 2% probability of exceedance in 50 years (relatively higher seismic events) is associated with the collapse-prevention limit state while the one of a 10% probability of exceedance in 50 years (relatively lower seismic events) is associated with the serviceability limit state;

2) the two uniform hazard spectra (5% damping) are then converted into uniform hazard displacement spectra (period vs. spectral displacement) using Eq. 5.15 (Priestley et al. 2007), where, T is the period of the structure in seconds; $S_d(T)$ is the spectral displacement at a period of T seconds; and $S_a(T)$ is the spectral acceleration at a period T .

$$S_d(T) = \frac{T^2}{4 * \pi^2} * S_a(T) \quad \text{(Equation 5.15)}$$

3) the height of the pier, known from the topography of the construction site of the bridge, should be used to calculate the performance lateral displacements for the two performance levels (Δ_{CP-P}) and (Δ_{Ser-P}) using Eqs. 5.6 and 5.10, respectively;

4) the uniform hazard displacement spectra (step 2), along with the performance displacements for the two performance levels (step 3), are both used to obtain the target periods for the pier in the cases of collapse-prevention (T_{CP-P}) and serviceability (T_{Ser-P}) limit states (Fig. 6.17).

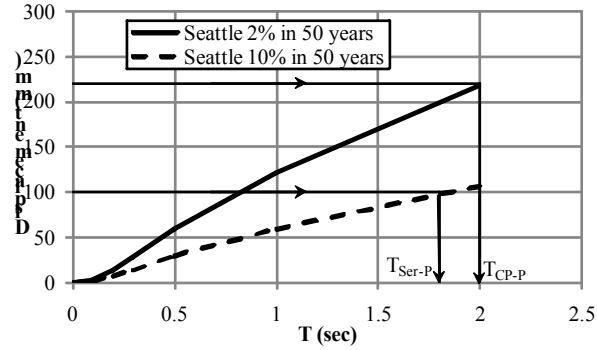


Figure 6.17: A diagram showing how to obtain the periods of the pier from the uniform hazard displacement spectra of the Seattle, WA area

5) the periods of the pier and the mass acting on the pier along with T_{CP-P} and T_{Ser-P} are used to calculate the target secant stiffness (Eq. 5.16) of the pier in the collapse-prevention and serviceability using the respective periods (step 4).

$$K = \frac{4\pi^2 m}{T^2} \quad \text{(Equation 5.16)}$$

6) the target performance lateral loads (F_{CP-P}^*) and (F_{Ser-P}^*) are computed by multiplying the secant stiffness by its corresponding performance lateral .

7) a diameter for the pier should be assumed or alternatively computed using Eq. 5.17 which is an approximate equation that gives an idea of the diameter that is most likely to fulfill the target performance levels. The post-tensioning stress on concrete as a percentage of f_c is then calculated using Eq. 5.7.

$$D \text{ (mm)} = 3.0 \times F_{CP-P}^{0.33} \times H^{0.42} \quad \text{(Equation 5.17)}$$

8) the performance lateral load for the serviceability limit state (F_{Ser-P}^{**}) corresponding to previously calculated pier's diameter and post-tensioning stress is calculated using Eq. 5.11.

9) if F_{ser-P}^{**} calculated from step 8 is greater than or equal to the target F_{ser-P}^* calculated in step 6, then F_{ser-P} equals F_{ser-P}^{**} and the next step can be processed. If not, F_{ser-P} equals F_{ser-P}^* , PT and F_{CP-P} are recalculated by substituting in Eqs. 5.11 and 5.7, respectively.

10) the target initial stress in the post-tensioning tendons (Eq. 5.20) is taken as the minimum of the stress values computed using Eq. 5.18 and 5.19, where; σ_{PT-Ser} is the initial post-tensioning stress in the tendons that will make the tendons reach 90% of its yield stress when the lateral displacement of the pier reaches Δ_{Ser-P} ; σ_{PT-CP} is the initial post-tensioning stress in the tendons that will make the tendons reach 100% of its yield stress when the lateral displacement of the pier reaches Δ_{CP-P} ; σ_y is the yield stress of the tendons' material; DS are calculated from Eq. 5.14.

$$\sigma_{PT-Ser} = 0.9\sigma_y / \left[1 + \frac{1.2 \times 10^4 D^{0.78}}{PT^{1.4} H^2} \times (\Delta_{Ser-P} - DS) \right] \quad (\text{Equation 5.18})$$

$$\sigma_{PT-CP} = \sigma_y / \left[1 + \frac{1.2 \times 10^4 D^{0.78}}{PT^{1.4} H^2} \times (\Delta_{CP-P} - DS) \right] \quad (\text{Equation 5.19})$$

$$\sigma_{PT} = \text{minimum of } \begin{cases} \sigma_{PT-Ser} \\ \sigma_{PT-CP} \end{cases} \quad (\text{Equation 5.20})$$

11) the cross sectional area of the tendon (A_{PT}) is calculated through Eq. 5.21, where;

$$A_{PT} = \frac{A_{pier} \times PT \times f_c'}{\sigma_{PT}} \quad (\text{Equation 5.21})$$

12) F_{CP-y} , F_{Ser-y} , Δ_{CP-y} , and Δ_{Ser-y} are computed using Eqs. 5.4, 5.9, 5.5, and 5.5, respectively.

6.15 Findings and Conclusions

This chapter presents the analysis obtained from a group of 84 piers with different design parameters analyzed using a previously prepared FE model. The behavior's objectives of two performance levels had been set for the SPPT pier system. A set of empirical equations capable of predicting the backbone curve of the piers had been derived using the data derived from that large set of piers. Those empirical equations had been arranged in a design procedure so as to choose the design parameters that make the pier fulfill the two performance levels. The analysis conducted in this chapter revealed that:

- The developed empirical equations were able to predict the bilinearized backbone curve of the SPPT piers within a certain error margin.
- The error associated with using the set of empirical equations to predict the backbone curves is believed to be treatable by adding a factor of safety that will increase the accuracy and safety margin of the methodology. Moreover, the developed design methodology has the potentiality to be refined upon the availability of more experimental results in the future.
- The performance displacement for the collapse-prevention and serviceability limit states was capped by the maximum lateral drift of 4.5% and 2.0%, respectively.
- The material failure wasn't prevailing in capping the performance lateral displacement in the serviceability limit state; this can be attributed to the high friction stresses at the base of the pier that has a confinement effect on the toe's concrete.
- The high recentering capability of the SPPT piers prevented the residual drift angle to cap the performance lateral displacement.

- The effective stiffness of the SPPT piers was found to be less than the stiffness of the cantilever piers using the beam theory and the reduction factor was found to be a function in the stresses induced on the concrete by the post-tensioning force.
- The yield and performance lateral loads were found to be inversely proportional to the pier's height and directly proportional to the piers diameter, stress induced on the concrete from the post-tensioning load and the external bridge service load.
- In the case of high post-tensioning and external service loads, the tendons lose its post-tensioning stress at the beginning of the lateral loading. Once the neutral axis at the bottommost section of the pier reached the tendon's position, the post-tensioning stress increases approximately linearly with lateral drift angle.
- In the case of low post-tensioning and axial service loads, the rigid body rocking of the pier's segments is prevailing, this results in approximately a horizontal plateau followed by a linear increase in the post-tensioning as the neutral axis reached the tendon's position.
- The developed empirical equations to predict the lateral displacement vs. change in post-tensioning stresses were able to capture the behavior of the tendons.
- The rate of increase in post-tensioning stress was found to be directly proportional to the diameter of the pier and inversely proportional to the pier's height and the post-tensioning stress on the concrete. On the other hand, the displacement at which the increase in post-tensioning stress starts is inversely proportional to the pier's diameter and directly proportional to the pier's height, post-tensioning and serviceability axial load stress acting on the pier.
- The developed design procedure showed its applicability to piers with parameters other than the ones used in this study.

- In the case of piers with design parameter parameters (diameter, height, post-tensioning stress and stress due to the external service loads) outside the range studied in this chapter, additional studies and experiments should be made for these specific cases to be able to predict its real behavior.

6.17 References

- ABAQUS Software and Documentation, Version 6.8-2. © Dassault Systèmes, SIMULIA, 2008.
- Beque, J., Patnaik, A. K., and Rizkalla, S., (2003), “Analytical models for concrete confined with FRP tubes” *J. Composites for Construction*, ASCE, 7(1), 31-38.
- California Office of Emergency Services (OES), vision 2000: Performance Based Seismic Engineering of Buildings, Structural Engineers Association of California, Sacramento, USA, 1995
- Chang, K. C., Loh, C. H., Chiu, H. S., Hwang, J. S., Cheng, C. B., and Wang, J. C. (2002). “Seismic behavior of precast segmental bridge columns and design methodology for applications in Taiwan”, Taiwan Area National Expressway Engineering Bureau, Taipei, Taiwan in Chinese.
- Dawood, H. M., “Seismic Behavior of Segmental Precast Post-tensioned Concrete Piers”, M.Sc. thesis, Washington State University, Washington, 2010
- Dawood, H., ElGawady, M., and Hewes, J.,(2010- In review). “Behavior of segmental precast post-tensioned bridge piers under lateral loads: experimental and modeling”, ASCE, *Journal of Bridge Engineering*.
- ElGawady, M., Booker, A., Dawood, H. M. (2010- In press). “Seismic behavior of post-tensioned concrete filled fiber tubes”, ASCE, *Journal of Composites for Construction*.
- ElGawady, M. A., Sha’lan A., and Dawood, H. M. (2010). “Seismic behavior of precast post-tensioned segmented frames”, 9th U.S. National and 10th Canadian Conference on Earthquake Engineering (July 25-29, 2010).
- ElGawady, M., and Sha’lan, A., (2010- In review). “Seismic behavior of self-centering bridge bents”, ASCE, *Journal of Bridge Engineering*.
- Fam, A. Z., and Rizkalla, S. H., (2001), “Confinement model for axially loaded concrete confined by circular fiber-reinforced polymer tubes” *ACI Str. J.*, 98 (4), 451-461.

- FEMA 356 (2000). "Prestandard and Commentary for the Seismic Rehabilitation of Buildings". Federal Emergency Management Agency. Washington, District of Columbia.
- Hewes, J.T. "Seismic Design and Performance of Precast Concrete Segmental Bridge Columns." Ph.D. Dissertation, University of California, San Diego, La Jolla, California. 2002.
- Kwan, W.-P., and Billington, S. L. (2003). "Unbonded posttensioned concrete bridge piers. I: Monotonic and cyclic analyses." *J. Bridge Eng.*, 8(2), 92–101.
- Lee, W. K., and Billington, S. L., (2009) "Modeling Residual Displacements of Concrete Bridge Columns under Earthquake Loads using Fiber Elements.", *Journal of Bridge Engineering*, (in press).
- Lee, J., and G. L. Fenves, (1998) "Plastic-Damage Model for Cyclic Loading of Concrete Structures," *Journal of Engineering Mechanics*, vol. 124, no.8, pp. 892–900.
- Lubliner, J., J. Oliver, S. Oller, and E. Oñate, (1989) "A Plastic-Damage Model for Concrete," *International Journal of Solids and Structures*, vol. 25, pp. 299–329.
- Mander, J. B., Priestley, M. J. N., and Park, R. (1988). "Theoretical stress-strain model for confined concrete." *J. Struct. Eng.*, 114(8), 1804–1826.
- Marriott, D., Pampanin, S., and Palermo, A., (2009). "Quasi-static and pseudo-dynamic testing of unbonded post-tensioned rocking bridge piers with external replaceable dissipaters" *J. Earthquake Engng. Struct. Dyn.*, 38, 331-345.
- Priestley, M.J.N., Calvi, G. M., and Kowalsky, M. J., "Displacement Based Seismic Design of Structures," IUSS Press, Pavia, Italy, 2007, 720pp.
- Samaan, M., Mirmiran, A., and Shahawy, M. (1998). "Model of concrete confined by fiber composite." *J. Struct. Eng.*, 124(9), 1025–1031.
- Structural Engineers Association of California, Recommended Lateral Force Requirements and Commentary, 7th Edition, SEAOC, Sacramento, CA, USA, 1999
- Teng, J. G., Jiang, T., Lam, L., and Luo, Y.Z., (2009), "Refinement of a design-oriented stress strain model for FRP-Confined concrete" *J. Composites for Construction*, ASCE, 13(4), 269-278.
- Wight, G. D., Kowalsky, M. J., and Ingham, J. M., (2007). "Direct Displacement-Based Seismic Design of Unbonded Post-Tensioned Masonry Walls." *ACI Structural Journal*, V. 104, No. 5, pp. 560-569.
- Yamashita, R., and Sanders, D. H. (2009). "Seismic Performance of Precast Unbonded Prestressed Concrete Columns." *ACI Structural Journal*, V. 106, No. 6, pp. 821-830.

APPENDIX

APPENDIX A

MATERIALS TESTING

During The current research different properties of the used materials had been tested and will be explained through this part of the appendix.

A.1 Concrete

Several concrete cylinders were cast during pouring the specimens by ElGawady et al. (2020) and ElGawady and Sha'lan (2010) (ASTM C172) and cured until the testing day (ASTM C192). Compressive strength (ASTM C39/C39M) was measured for six cylinders, three for concrete which was expected to give $f'_c = 13.8$ Mpa [2000 psi] and three more for $f'_c = 20.7$ Mpa [3000 psi] (Table A.1), (Fig. A.1). To assure the full contact between the cylinder ends and the machine's loading heads, either a steel cap filled with rubber or gypsum caps were used.



Figure A.1 Test setup for computing concrete characteristic strength f'_c

Table A.1 Summary of compression test results

Expected strength	Failure load kN [lbs]	f _c Mpa [psi]	status	f _c average
13.8Mpa [2 ksi]	509 [114,453]	27.9 [4050]	rejected	14.3 Mpa [2068psi]
13.8Mpa [2 Ksi]	246 [55,218]	13.5 [1954]	ok	
13.8Mpa [2 Ksi]	274 [61,672]	15.0 [2182]	ok	20.5 Mpa [2973psi]
20.7Mpa [3 ksi]	387 [86,953]	21.2 [3077]	ok	
20.7Mpa [3 Ksi]	380 [85,395]	20.8 [3022]	ok	
20.7Mpa [3 Ksi]	355 [79,706]	19.4 [2820]	ok	

Five more concrete cylinders were tested to calculate the static modulus of elasticity (ASTM C469) of the concrete (Figs. A.2 & A.3). Because the actual modulus of elasticity was computed, this value replaced the theoretical one suggested by Samaan et al. (1998) in their model as this should be used when no testing results are available.



Figure A.2 Test setup for computing static modulus of elasticity of the concrete cylinders

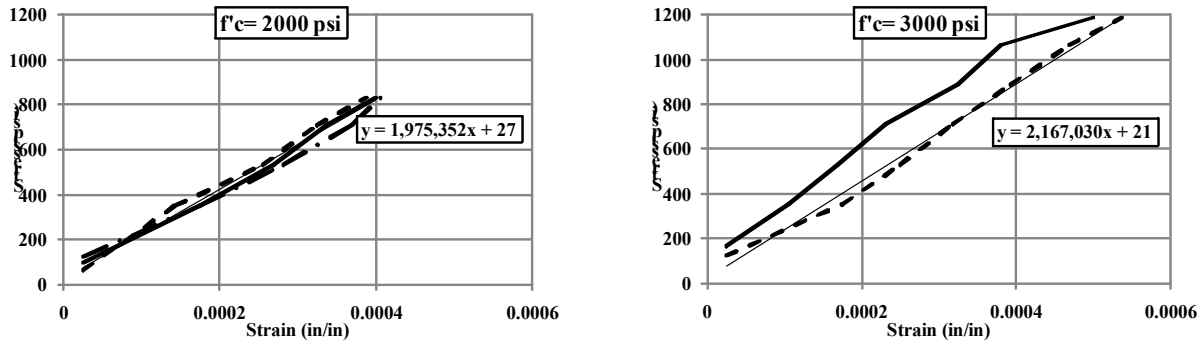


Figure A.3 Stress strain curves from the cylinders tests along with the equations of the trend lines

For information about testing results of the concrete cylinders of the concrete used in the piers studied in chapters (3) and (4) refer to Hewes (2002).

A.2 Post-tensioning bars

The stress-strain curve used in chapter (5) of this chapter is supplied by a certified test report provided by the DYWIYDAG Company which was done by North Star Steel Minnesota on 02/11/2003 (Fig. A.4). The post-tensioning bars in chapters (3 and 4) were used as reported by Hewes (2002).



NORTH STAR STEEL MINNESOTA

P.O. Box 64189
1678 Red Rock Road
Saint Paul, Minnesota 55164

Heat #:	S57731
Size:	32mm Int.
Product:	Dywidag
Grade:	D150
Date Rolled:	2/10/03
P.O.	
M.O.#:	C0019997

CERTIFIED TEST REPORT

CHEMICAL ANALYSIS (WT %)

C	Mn	P	S	Si	Sn	Cu	Ni	Cr	Mo	Cb	V	Co	Al	Ti	Ca	N
0.50	1.58	0.015	0.024	0.62	0.016	0.26	0.44	0.21	0.02	0.003	0.088	0.0100	0.003	0.0042	13	132

MATERIAL 100% MELTED AND ROLLED IN THE USA. MANUFACTURING PROCESSES FOR THIS STEEL, WHICH MAY INCLUDE SCRAP MELTED IN AN ELECTRIC ARC FURNACE AND HOT ROLLING, HAVE BEEN PERFORMED AT NORTH STAR STEEL MINNESOTA, 1678 RED ROCK ROAD, SAINT PAUL, MINNESOTA, USA. ALL PRODUCT PRODUCED FROM STRAND CAST BILLETS. NO WELD REPAIRMENT PERFORMED. STEEL NOT EXPOSED TO MERCURY OR ANY LIQUID ALLOY WHICH IS LIQUID AT AMBIENT TEMPERATURES DURING PROCESSING OR WHILE IN NORTH STAR STEEL MINNESOTA POSSESSION.

JOMINY END QUENCH HARDENABILITY RESULTS (HRC)

J1	J2	J3	J4	J5	J6	J7	J8	J9	J10	J11	J12
J13	J14	J15	J16	J18	J20	J22	J24	J26	J28	J30	J32

MECHANICAL TEST REPORT

SPECIMEN AREA (in ²)	YIELD (Kpsi)	YIELD (ksi)	TENSILE (Kpsi)	TENSILE (ksi)	GAUGE LENGTH (in)	% ELONG	BEND	% R.A.	SPECIFICATION / GRADE
1.201	159.8	126.8	202.9	160.9	12.50	10.40	OK		D150
1.256	168.0	133.8	204.4	162.7	12.50	9.60	OK		D150

Additional Specifications/Comments:

Meets Material requirements of A722-88

A722-88

Conforms to DSI, USA, INC. Spec 2, Revision 5, Issued Aug 14th 1997.

Grain Size: <input type="text"/>	Reduction Ratio: <input type="text"/>	C.E Per: <input type="text"/>	As Rolled surface Hardness	
Coding: CIN	D.I: 5.37 in.	Ms: <input type="text"/> Deg F.	C.E: <input type="text"/>	Bhn
				Test 1: <input type="text"/>
				Test 2: <input type="text"/>
HRC				

CHARPY IMPACT TEST		
*	Test 1	Test 2
Temp (F)		
ft-lb 1		
ft-lb 2		
ft-lb 3		

Micro Clean Average

A1: A2: B1: B2: C1: C2: D1: D2: S-Rating: O-Rating:

Macro Etch:

ASTM Test Method										
Accredited to:	ASTM A370	ASTM E8	ASTM E10	ASTM E18	ASTM E21	ASTM E112	ASTM E255	ASTM E288	ASTM E418	ASTM E1619
ISO Guide 25	X	X	X	X				X	X	X
ISO Guide 25 AND FQA									X	X
Subcontractor (ISO Guide 25)										

The above results relate only to the items tested.

* Denotes tests performed by subcontractors in accordance with ASTM standards.

Chemical tests performed in accordance with ASTM E415 and E1019. Mechanical tests performed in accordance with ASTM E8, E10 and A370. All other tests performed in accordance with the requirements of applicable specifications unless otherwise noted above. We hereby certify that the above test results are representative of those contained in the records of the company.

Any modification to this certificate as provided by North Star Steel Minnesota without the expressed written consent of North Star Steel Minnesota negates the validity of this test report. This report shall not be reproduced except in full, without the expressed written consent of North Star Steel Minnesota. North Star Steel Minnesota is not responsible for the inability of this material to meet specific applications.

SIGNED:

DATE: 02/11/2003

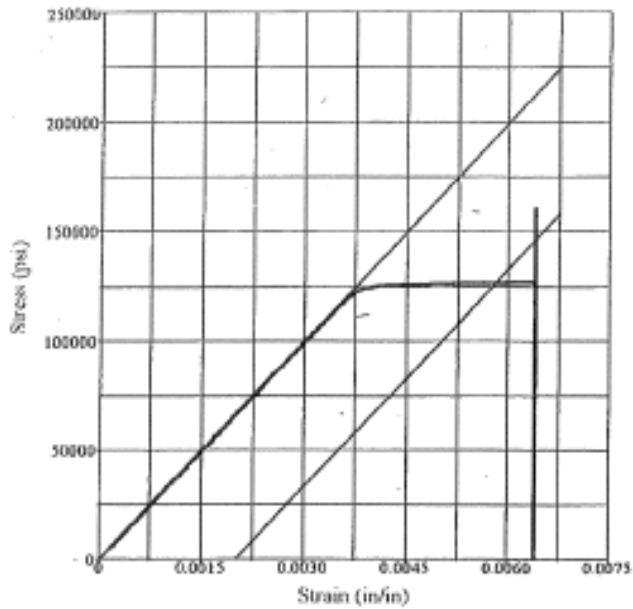
APPROVAL:

SWORN AND SUBSCRIBED TO BEFORE ME

THIS _____ DAY _____

NOTARY PUBLIC

THIS CERTIFICATE IS NOTARIZED ONLY WHEN REQUESTED.



Test Results	
Area:	1.261 in ²
Tangent Modulus:	33288.09 ksi
Offset Yield Stress:	126.8 ksi
Offset Yield Load:	159.8 kip
Peak Load:	202.9 kip
Tensile Strength:	160.9 ksi
Total Elongation:	10.40 %
Pretest Punch Length:	12.5 in
Posttest Punch Length:	13.8 in

Test Summary

Counter: 9453
 Elapsed Time: 00:01:22
 Mill Order #: 226753
 Heat Number: S57731
 Grade: D150
 Size: 32MMI
 Product: Dywidag
 Operator: GS
 Bundle #: A030276
 Comments: 1000
 Procedure Name: Dywidag with Ext
 Start Date: 2/10/03
 Start Time: 7:27:34 AM
 End Date: 2/10/03
 End Time: 7:28:56 AM
 Workstation: NSSSTP0135W
 Tested By: jwilson

Figure A.4: Copy of the report supplied by the DYWIYDAG company

A.3 Glass Fiber Reinforced Polymer (GFRP)

GFRP was tested in tension by (Rai) (Table A.2) and compression by (Westmoreland Mechanical Testing & Research, Inc.) using (ASTM D6641) (Fig. A.5).

Table A.2 Summary of tension tests of GFRP specimens (Rai)

Gauge length: 2 in Strain rate: 0.1 in/in.min Date of test: 09/29/09						
Sample	Thickness mm [in]	Width mm [in]	Peak stress Mpa [psi]	Cracking stress Mpa [psi]	Cracking strain (%)	Young's modulus Mps [psi]
1	3.23 [0.127]	12.98 [0.511]	65.0 [9427]	55.9 [8108]	0.3946	13627 [1,976,442]
2	3.20 [0.126]	13.00 [0.512]	64.0 [9283]	60.0 [8707]	0.4126	14436 [2,093,749]
3	3.23 [0.127]	12.98 [0.511]	63.5 [9203]	56.9 [8248]	0.3979	14543 [2,109,212]
4	[discarded]	[--]	[--]	[--]	--	[--]
5	3.20 [0.126]	12.93 [0.509]	62.4 [9046]	51.0 [7392]	0.3721	12303 [1,784,448]
6	3.23 [0.127]	13.13 [0.517]	63.7 [9248]	57.0 [8272]	0.3970	14332 [2,078,645]
			Mean (Young's modulus) =			13848 [2,008,499]



Westmoreland Mechanical Testing & Research, Inc.

P.O. Box 388

221 Westmoreland Drive

Youngstown, Pa. 15696-0388 U.S.A.

Telephone: 724-537-3131 Fax: 724-537-3151

Website: www.wmtr.com

WMT&R is a technical leader in the material testing industry.

1 December 2009

Washington State University
100 Dairy Road
Pullman, WA 99164-1120

WMT&R Report No.: 9-41303
Purchase Order No.: K621273
WMT&R Quote No.: QN292761

Attention: Dr. Mohammed ElGawady

Subject: Compression Testing of Glass Fiber Reinforced Polymer Tube Sections

Introduction

Five (5) already machined tube sections, identified as glass fiber reinforced polymer material, were provided by Washington State University for compressive strength testing. An additional specimen was provided as a spare in the event of an invalid result. Testing was originally to be performed in accordance with ASTM D3410 but due to the unavailability of an ASTM D3410 fixture, WMT&R was given authorization by Washington State to substitute ASTM D6641 as the test standard of interest. As a result, the overall specimen length was reduced from 6.0" to 5.5" to comply with Section 4.1 of ASTM D6641.

Prior to testing, the cross section area of each specimen was measured using a Keyence VHX 600E Digital Microscope with integrated image analysis software. Each cross section image was calibrated at 10X magnification, a perimeter sketched around the specimen, and the area within determined (Figure 1). The width and thickness of each specimen was also measured at three (3) distinct locations within the middle 0.5" such that an alternate cross section area may be determined using a nominal tube outer diameter and average width/thickness values. All specimens were then equipped with a Vishay Micromasurements uniaxial general purpose strain gage, Item No. CEA-06-125UN-350, on the outer diameter face for strain measurement. A bending evaluation as defined by Section 7.6 of ASTM D6641 was not performed due to monetary concerns.

Testing was conducted utilizing a fixture capable of inducing a compressive force through simultaneous end and shear loading as shown in Figure 2. The test fixture bolts used to control shear loading were torqued to a minimum of 25in.*lbs applied in increments using a diagonally crossing pattern. Following specimen installation, the fixture was placed between two well aligned platens then a compressive load applied at a crosshead controlled rate of 0.05in./min. until rupture.

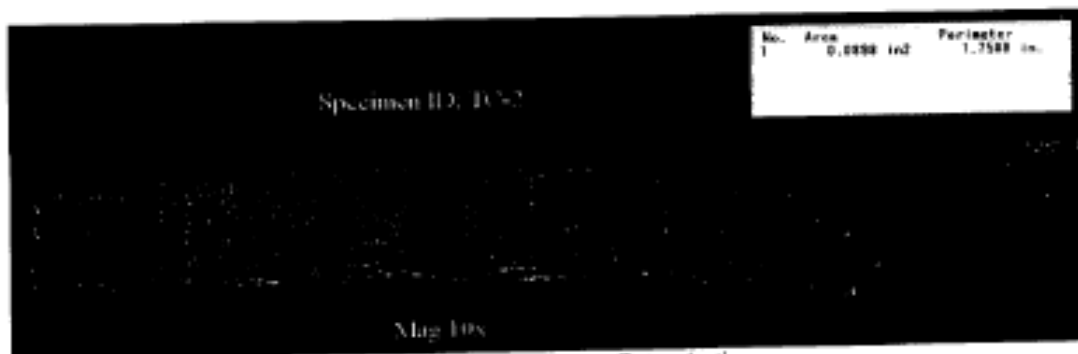


Figure 1: Cross Section Area Determination

NOTE: THE RECORDING OF FALSE, FICTITIOUS, OR FRAUDULENT STATEMENTS OR ENTRIES ON THIS DOCUMENT MAY BE PUNISHABLE AS A FELONY UNDER FEDERAL STATUTE.

THIS CERTIFICATE OR REPORT SHALL NOT BE REPRODUCED EXCEPT IN FULL, WITHOUT THE WRITTEN APPROVAL OF WMT&R, INC.

Testing Specialists for Aerospace, Automotive, and Material Testing Fields

Locations in Youngstown, PA U.S.A. - Tel. (724) 537-3131 and
Banbury, Oron U.K. - Tel. +44 (0) 1295 261211

1 December 2009
Purchase Order No.: K621273

WMT&R Report No.: 9-41303

Continued:



Figure 2: ASTM D6641 Test Fixture

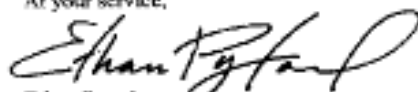
An automated test system utilizing an Instron servo-controlled, hydraulically actuated test frame in conjunction with software designed by Westmoreland Mechanical Testing and Research, Inc., provided the means for load application. Vishay-MicroMeasurements Strain Smart Software Version 3.10 with a model 5100 scanner provided the means for acquisition of load and strain at a sampling rate of 50 points per second.

Testing results, including relevant comments, may be found on the following pages and accompanying compact disc. The graphical data was plotted to the maximum strain value acquired. Strain to rupture was not obtained for Specimen ID Nos. TC-3 and TC-5 as a result of deformation of the test area which detached the gage and consequently terminated the signal. All tested and untested material is also enclosed.

All machining, testing and inspections were performed in accordance with the WMT&R Quality Assurance Manual Rev. 11, dated 12/3/2008.

If you have any questions concerning this report, please feel free to contact me. If I am unavailable, you may also speak with Mr. Matt Wojton, Tensile Laboratory Supervisor.

At your service,


Ethan Pytash
Mechanical Engineer

bt

K:\Epytash\Washington State University\9-41303\9-41303.doc

NOTE: THE RECORDING OF FALSE, FICTITIOUS, OR FRAUDULENT STATEMENTS OR ENTRIES ON THIS DOCUMENT MAY BE PUNISHABLE AS A FELONY UNDER FEDERAL STATUTE.
THIS CERTIFICATE OR REPORT SHALL NOT BE REPRODUCED EXCEPT IN FULL, WITHOUT THE WRITTEN APPROVAL OF WMT&R, INC.



Westmoreland Mechanical Testing and Research, Inc.
 ASTM D6641 Testing Results



Materials Testing Laboratory
 Tuesday, December 01, 2009

Washington State University
 100 Dairy Road
 Pullman, WA 99164-1120
 Attention: Dr. Mohammed ElGawady

WMT&R Report Number: 9-41303
 WMT&R Quote Number: QN292761
 Washington State Purchase Order Number: K621273

Test Type: Compressive Properties per ASTM D6641-09
Test Environment: 72°F / Ambient Air
Speed of Testing: 0.050 in./min.
Material: Glass Fiber Reinforced Polymer Tube Sections

Specimen ID Number	Test Log Number	Ult. Comp. Strength (ksi)	Ult. Comp. Load (lbf)	0.2% Off. Yield Strength (ksi)	0.2% Off. Yield Load (ksi)	Modulus (Msi)	Width (in.)	Thickness (in.)	Machine Number	Disposition
TC-1	L28887	-27.122	-2465.4	-23.032	-2093.6	2.46	0.7599	0.1267	H14	R
TC-2	L28888	-28.162	-2528.9	-24.565	-2205.9	2.46	0.7630	0.1252	H14	R
TC-3	L28889	-29.097	-2572.2	-24.806	-2192.9	2.55	0.7615	0.1348	H14	R
TC-4	L28890	-28.044	-2465.1	-23.323	-2050.1	2.45	0.7604	0.1209	H14	R
TC-5	L28891	-26.950	-2476.7	-21.120	-1940.9	2.11	0.7607	0.1205	H14	R
Average		-27.875	-2501.7	-23.369	-2096.7	2.41	0.7611	0.1236		
Standard Deviation		0.8697	47.4140	1.4722	109.1259	0.1696	0.0012	0.0027		
Coefficient of Variation		-3.1200	-1.8953	-6.2999	-5.2047	7.0412	0.1592	2.2112		

AU/R: A=Acceptable, U=Unacceptable, R=Report

Note(s):
 All specimens were equipped with a Vishay MicroMeasurements uniaxial general purpose strain gage, Item No. CEA-06-125UN-350, on the outer diameter side.
 A 25in*lb torque was applied to all fixture bolts in increments using a diagonally crossing pattern.
 Load-Strain Data was recorded at 50 data points per second using Vishay-MicroMeasurements Strain Smart Software Version 3.10 in conjunction with a model 5100 scanner.
 All modulus calculations were performed using a range of 1000 to 3000 microstrain according to ASTM D6641.

Eshan Piyash
 Eshan Piyash
 Mechanical Engineer

Figure A.5: Copy of the compression testing report of the FRP

A.4 Fiber Sheets Used To Retrofit JH12 & JH22 (CHAPTER 3)

Table A.3 shows the FRP material's properties used to retrofit piers JH12 and JH22 (chapter 3).

Table A.3 Typical dry fiber properties used in chapter (3)

Tensile strength	3.24 GPa [470,000 psi]
Tensile modulus	72.4 GPa [10.5×10^6 psi]
Ultimate elongation	4.5%
Density	2.55 g/cm ³ [0.092 lbs/in ³]
Weight per sq. yd.	915 g/m ² [27 oz.]
Fiber thickness	0.36 mm [0.014 in]

A.5 References:

- ASTM C172 (Standard practice for sampling freshly mixed concrete).
- ASTM C 39/C 39M (Standard test method for compressive strength of cylindrical concrete specimens).
- ASTM C469 (Standard test method for static modulus of elasticity and poisson's ratio of concrete in compression).
- ASTM C192 (Making and curing concrete test specimens in the laboratory).
- ASTM C617 (Capping cylindrical concrete specimens).
- ASTM C469 (Static modulus of elasticity and poisson's ratio of concrete in compression).
- ElGawady, M., Booker, A., Dawood, H. M. (2010- In press). "Seismic behavior of post-tensioned concrete filled fiber tubes", ASCE, Journal of Composites for Construction.
- ElGawady, M., and Sha'lan, A., (2010- In review). "Seismic behavior of self-centering bridge bents", ASCE, Journal of Bridge Engineering.
- Hewes, J.T. "Seismic Design and Performance of Precast Concrete Segmental Bridge Columns." Ph.D. Dissertation, University of California, San Diego, La Jolla, California. 2002.